An Experimental and Analytical Investigation of Thermoacoustic Convection Heat Transfer in Gravity and Zero-Gravity Environments

Masood Parang

The University of Tennessee
Knoxville, Tennessee 37996-2210

April 1986

Prepared for;

National Aeronautics and Space Administration
Lewis Research Center
Under Grant NAG3-239

ACKNOWLEDGMENTS

The author wishes to acknowledge the financial support provided for this work by NASA-Lewis Research Center under grant number NAG 3-239. Special gratitude is due to Dr. An-Ti Chai, the Project Manager of this grant, for his support and many helpful comments and suggestions. Acknowledgment is made to Dr. Thomas L. Labus for his role in the support and funding of this project.

The author is indebted to Mr. Adel Salah-Eddine, graduate student at the Mechanical and Aerospace Engineering Department, the University of Tennessee, for his significant contribution in different phases of this study. A special credit is due to him for his efforts in the completion of this research project.

ABSTRACT

An experimental and analytical study of Thermoacoustic Convection (TAC) heat transfer in gravity and zero-gravity environments is presented. The experimental apparatus consisted of a cylinder containing air as fluid. The side wall of the cylinder was insulated while the bottom wall was allowed to remain at the ambient temperature. The enclosed air was rapidly heated by the top surface which consisted of a thin stainless steel foil connected to a battery pack as the power source. Thermocouples were used to measure the transient temperature of the air on the axis of the cylinder. The output of the thermocouples were displayed on digital thermometers and the temperature displays were recorded on film using a high-speed movie camera. Temperature measurements were obtained in the zero-gravity environment by dropping the apparatus in the 2-seconds Zero-Gravity Drop Tower Facilities of NASA-Lewis Research Center. In addition, experiments were also performed in the gravity environment and the results are compared in detail with those obtained under zero-gravity conditions.

A conduction-only numerical heat transfer model was developed to compute the transient air temperature in the cylindrical geometry. For the purposes of comparison, the

experimental geometry and boundary conditions were employed in this numerical model. The results are compared to the experimental data to determine the significance of the thermoacoustic convection heat transfer mechanism. It is observed that the rate of heat transfer to the air measured during the experiments is consistently higher than that obtained by the conduction-only solution.

A one-dimensional TAC numerical model was developed to determine the unsteady temperature distribution in the enclosed air. This numerical model is similar to those studied in earlier investigations of thermoacoustic convection heat transfer. The governing equations were numerically integrated employing the transient heater-surface temperature measured in the experiments. The numerical results show that the variations in the non-dimensional air temperature with time agree qualitatively with those measured in the experiments. The numerical model used does not take into account all of the experimental conditions and therefore no attempt is made for a quantitative comparison between the experimental results and the computed temperature profiles based on this model.

TABLE OF CONTENTS

LIST OF TABLES

LIST OF FIGURES

NOMENCLATURE

A_s	heater surface area
A_d	cross sectional area of the cylinder
C_p	specific heat at constant pressure
C_v	specific heat at constant volume
D_t	diameter of the thermocouple
F	radiation geometric configuration factor
g	gravitational acceleration
K	thermal conductivity
L	distance between parallel plates defined in Figure II-5 and cylinder height in the experimental apparatus
P	pressure
P_0	initial pressure
P_i	input power
Pe	Peclet Number
Pr	Prandtl Number
q_d	direct incident radiation
q_e	rate of emitted radiation
q_a	rate of heat absorbed due to radiation
q_r	rate of reflected radiation incident on the thermocouple surface
R	specific gas constant
R_s	electric resistance of the steel foil
Re	Reynolds Number

R_d	cylinder radius
R_i	reflectivity of the insulation material
S	camera speed in frames/second
t	time
T	temperature
T_w	heated wall temperature
T_o	initial temperature
T*	average temperature of the heater surface
T	non-dimensional air temperature
U	velocity component in the x-direction
V_t	volume of the thermocouple
V_i	input voltage
w_t	uncertainty in the time measurement
w_T	uncertainty in the temperature measurement
w_l	uncertainty in the thermocouple location
w_R	uncertainty in the foil electric resistance
w_v	uncertainty in the input voltage
γ	ratio of specific heats
ρ	density
ρ_t	density of the thermocouple material
ρ_i	initial density
μ'	dynamic viscosity
ε_s	emissivity of the stainless steel foil
Δx	grid spacing
Δt	time increment
ΔT_t	change in the thermocouple temperature

σ	Stefan-Boltzmann constant
$( )'$	indicates dimensional quantities

CHAPTER I

INTRODUCTION

Material processing in space has received a great deal of attention in the past two decades. There is enough evidence to show that materials produced in space would be superior in quality to those manufactured on earth. When density differences are present in a fluid, gravity induces fluid motion which may cause inhomogeneity problems during material processing and manufacturing on earth. Therefore, conditions of weightlessness in space can provide a unique environment for manufacturing processes where buoyancy-driven fluid circulation is undesirable. Crystal growth is one example that shows the advantages of manufacturing in space. Buoyancy-driven fluid motion has been known to cause inhomogeneities in crystals that are grown in a gravitational field. These, in turn, may cause serious problems in the performance of integrated circuits and other electronic devices that are made of such crystals. Therefore, crystals that are grown in space are expected to produce better electronic components. Another advantage of manufacturing in a low gravitational field (or more accurately, conditions of near weightlessness) is the elimination of container contamination in the solidification of melts. Since solid boundaries are not

needed to hold fluids in space, problems arising due to reactions between fluids and container boundaries can be eliminated.

In most applications of material processing, fluids are either heated or cooled. Therefore, it is essential to establish a clear understanding of the extent and nature of heat transfer in space and the factors on which it depends in order to utilize its effects to the best advantage [1].

In the conditions of weightlessness and with the absence of other driving forces for natural convection (e.g., vibrations, electromagnetic forces, etc.), conduction becomes the dominant heat transfer mechanism. However, in most practical situations in space as, for example, within a space vehicle, fluid motion and convection heat transfer exist due to a variety of forces such as g-Jitter, surface tension, vibrations, electromagnetic forces, and thermal volumetric expansion. This study focuses on a convection heat transfer mechanism which exists solely due to thermal volumetric expansion and where it is assumed that all other driving forces for natural convection are either non-existant or negligible.

Thermoacoustic Convection (TAC) is a heat transfer mechanism driven by thermal volumetric expansion. It is defined as energy transport by pressure waves that

propagate at acoustic speed in a fluid medium. These waves are generated by rapid addition of heat at a fluid boundary or within the body of the fluid by processes such as chemical reactions or by absorption of electromagnetic radiation. The basic mechanism by which these acoustic waves are generated is as follows: when the internal energy of a fluid particle is suddenly increased, the volume occupied by the fluid particle increases. This sudden volume expansion produces pressure waves that induce convective motion and enhanced heat transfer rate.

One of the main motivations in the investigation of TAC is in space applications. Manufacturing processes, cryogenic storage, and fluid handling processes in space may all include large TAC heat transfer rates. The TAC heat transfer mechanism is also of fundamental scientific interest. There is, however, an almost complete lack of experimental evidence on the significance of TAC. Above considerations led the Overstudy Committee on Fluid Physics, Thermodynamics, and Heat Transfer Experiments in Space to recommend a series of TAC experiments to be prformed in space [2].

CHAPTER II

LITERATURE REVIEW

In this chapter a brief review of the historical background of thermoacoustic convection heat transfer is presented. The review begins with a brief discussion of the early observations on thermoacoustic oscillations followed by a more detailed description of recent investigations on TAC.

Sondhauss and Rijke Oscillations:

Thermoacoustic oscillations can be generated in a gas-filled tube with one open end and one closed end when thermal energy is transferred to the gas either internally or externally at the closed end. Sondhauss investigated this physical phenomenon and found that sound is produced when a steady flame is applied to the bulb at the closed end of a glass tube filled with air. A schematic diagram of a Sondhauss Tube is shown in Figure II-1. Sondhauss discovered that the heat addition at the bulb of the tube caused the air to oscillate and produce a sound which is characteristic of the tube dimensions. Furthermore, he also found that the vibration of the tube itself did not play a major role in inducing these oscillations. Sondhauss published his first account on such TAC oscillations in 1850 but did

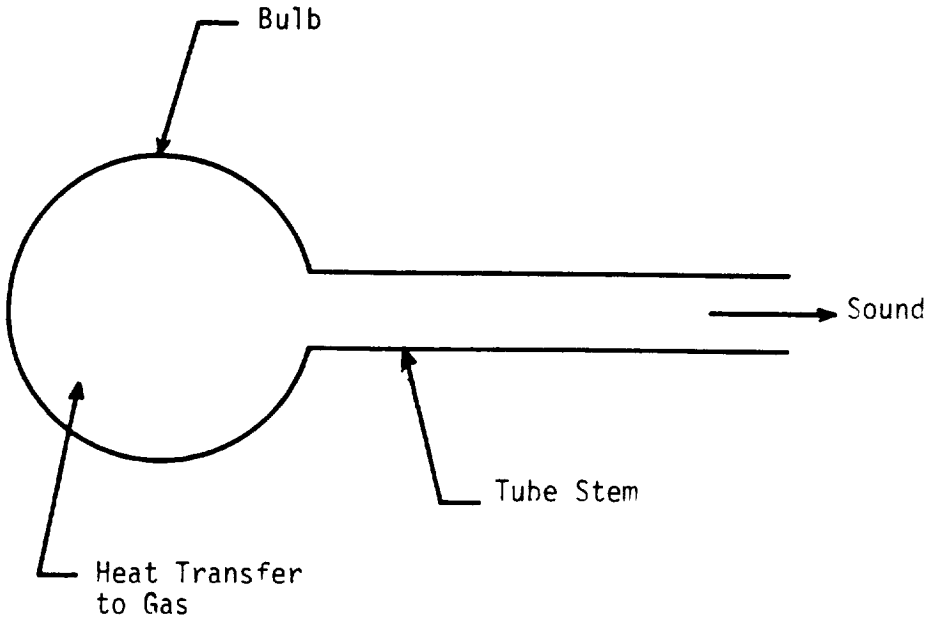

Figure II-1. Sondhauss Tube

not, however, explain the physical mechanism causing the production of sound [3].

The first explanation of the physical aspects involved in the generation of Sondhauss Oscillations was offered by Rayliegh [4]. His criterion was stated as follows:

> If heat be added to the air at the moment of greatest condensation (compression) or taken from it at the moment of greatest rarefaction, the vibration is encouraged.

Rayliegh did not offer any proof for his criterion. But it is clear that Raylieh criterion is fulfilled in a Sondhauss tube since heat is transferred to the air at the bulb where the pressure is highest.

Feldman performed the most successful experimental study on Sondhauss Oscillations [5], and [6]. His work shows that acoustic Oscillations do not occur unless the rate of energy addition to the fluid exceed a certain minimum value. He also pointed out that the shape of the cavity plays an essential role in the production of sound. Furthermore, Feldman also found that the heat addition must occur at the section where the gas pressure and velocity are appreciable .

When a steady heat source is applied near the bottom end of a vertical gas-filled tube with both ends open, gas oscillations occur and sound is produced. These

oscillations are called Rijke Oscillations. Such a tube is called Rijke Tube and is shown in Figure II-2. Rijke discovered these thermoacoustic oscillations in 1859 [7]. He found that the upper end of the tube must remain open in order to generate such oscillations and thus concluded that the natural convection inside the tube encourages the vibrations in the gas. Furthermore, Rijke found that the oscillations are strongest when the heat source is located near the bottom end at a distance about one-fourth the length of the tube.

Just like Sondhauss, Rijke did not offer a substantial explanation of the physical mechanism involved in the generation of these oscillations. However, Rayliegh showed that the oscillations in Rijke Tube are composed of compression and expansion waves superimposed on a steady upward gas flow caused by natural convection. Rayliegh also observed that such thermoacoustic oscillations are encouraged when his criterion is fulfilled, that is, when the heater is located at the point of maximum pressure.

A series of analytical and experimental studies were performed in order to establish an understanding of such oscillations (see References 8-16). These investigations showed that Rayliegh criterion must be fulfilled for such oscillations to occur. However, a complete understanding

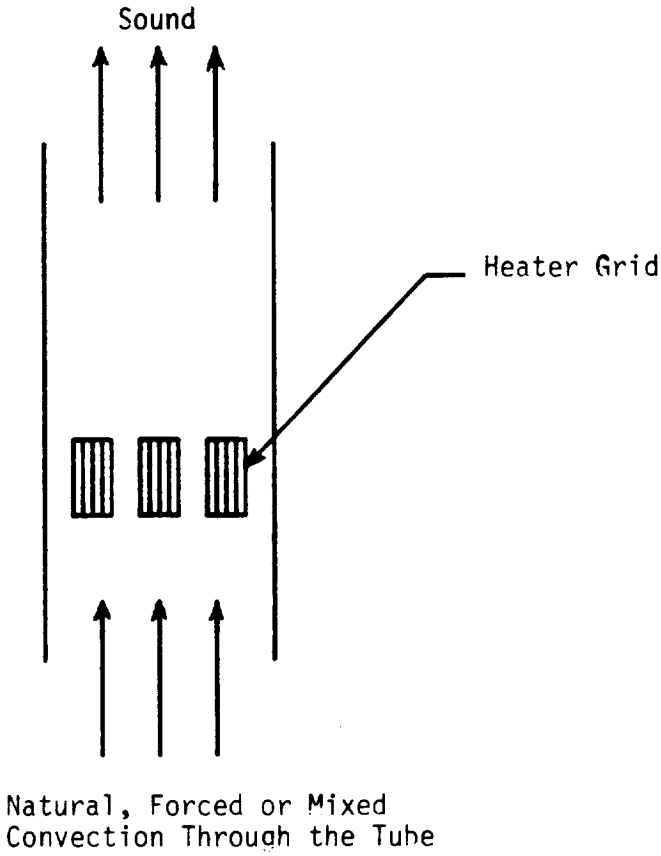

Figure II-2. Rijke Tube

of the physical mechanism involved in Rijke Oscillations does not exist.

Thermoacoustic Convection in Completely Confined Fluids.

In 1967 Larkin performed the first analytical investigation on thermoacoustic convection [17]. He applied numerical computation to solve the governing equations describing a one-dimensional heat transfer model. Transient spatial velocity, density, temperature, and pressure distribution were determined using a medium filled with helium gas and enclosed between two infinite parallel plates to simulate a one-dimensional heat flow. At $t'<0$ the temperature of helium was assumed to be uniform and equal to $T'_o(273^oK)$, at $t'>0$ the temperature of one boundary is suddenly raised to $2T'_o(546^oK)$ while keeping the other plate at its initial temperature. Because of the Zero-Gravity environment, no buoyancy force exists in the momentum equation. However, even in the absence of gravitational forces, Larkin found that thermal gradients could induce fluid motion as a result of fluid compressibility. The calculated fluid velocity showed thermally-induced convective oscillatory motion of an acoustical nature. The calculated spatial temperature distribution showed higher values than those obtained by pure conduction solution. Thus based on the results

obtained from the example problem, Larkin concluded the following:

1. The acoustical nature of the fluid motion suggests that thermoacoustic oscillations were generated.

2. Fluid oscillations introduced a convective mode that greatly enhanced the rate of heat flow.

3. The rate of pressure rise in the fluid is much higher than that predicted by a conduction solution.

In 1971, the so called Heat Flow and Convection (HFC) Experiments were conducted by astronaut Roosa aboard the Apollo 14 spacecraft. The objective of these experiments was to study heat flow patterns and fluid behavior in a reduced gravitational field. The "zone heating" experiments involved heating two glass cylinders,one containing distilled water and the other containing a 20 percent sugar solution. The transient temperature data obtained during the flight were higher than those obtained based on a conduction-only solution. In the "radial heating" experiments a closed disk-shaped layer of carbon dioxide was heated by a center post heater . Figure II-3 presents a comparison of the temperature predictions, based on a conduction and radiation solutions, and the actual flight data.

Analytical studies by Grodzka, Fan, and Hedden [18] suggested that the increase in the heat transfer rate measured during the Apollo 14 flight was caused by

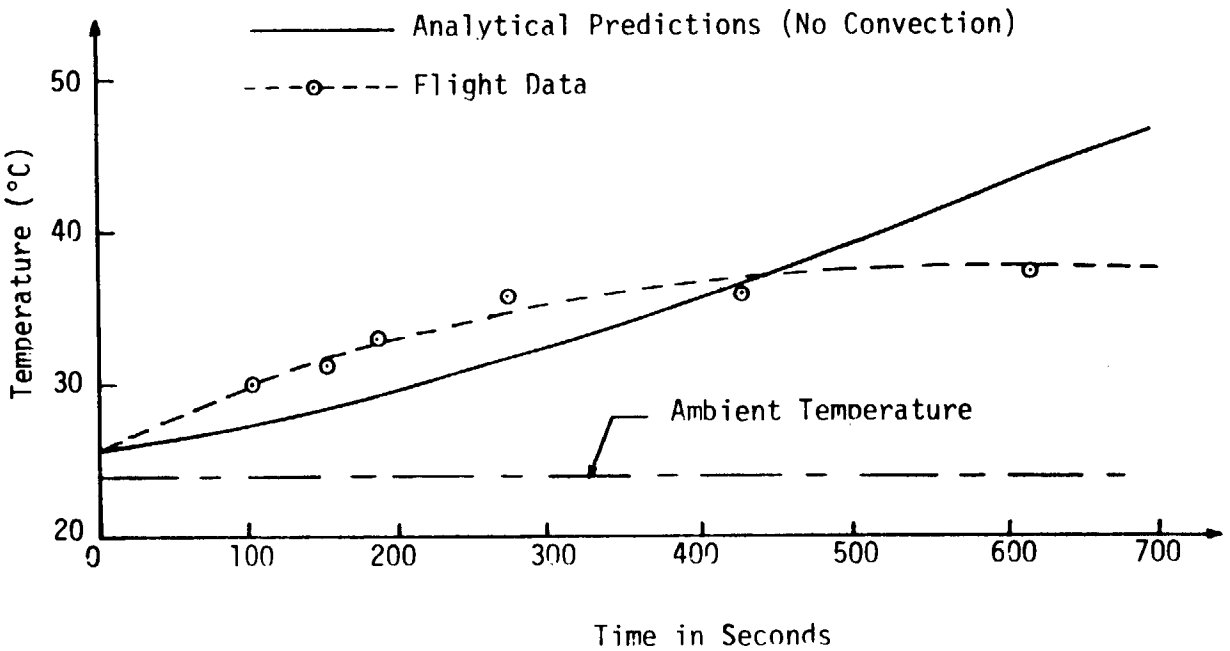

Figure II-3. Radial Heating Unit Temperature Profiles (Ref. 18).

thermoacoustic convection. These studies also pointed out that the rate of energy addition to the fluid dictates the magnitude of the effects of TAC.

The radial heating experiments were repeated during the Apollo 17 flight in 1972. These experiments were improved and extended versions of the Apollo 14 experiments. Instead of Carbon Dioxide, Argon gas was used as the working fluid. Typical results of the Apollo 17 experiments are presented in Figure II-4. An analysis of the results by Bannister, et al. [19] led to the following conclusions:

1. Thermoacoustic Convection effects were negligible during the Apollo 17 heating experiments.

2. The rates of heat addition to the fluids (7.5 Watts) were not sufficient to generate any TAC.

3. The high heat transfer rates observed in the Apollo 14 experiments were probably caused by spacecraft vibrations and g-jitter which were less severe on the Apollo 17 flight.

In 1973 L. W. Spradley, S. V. Bourgeois, C. Fan, and P. G. Grodzka presented an in-depth analytical investigation of one-dimensional TAC heat transfer problem [20]. This study was initiated to explain the behavior of the Apollo 14 data and to develop an understanding of the low gravity convection in space manufacturing. Spradley, et al. considered a

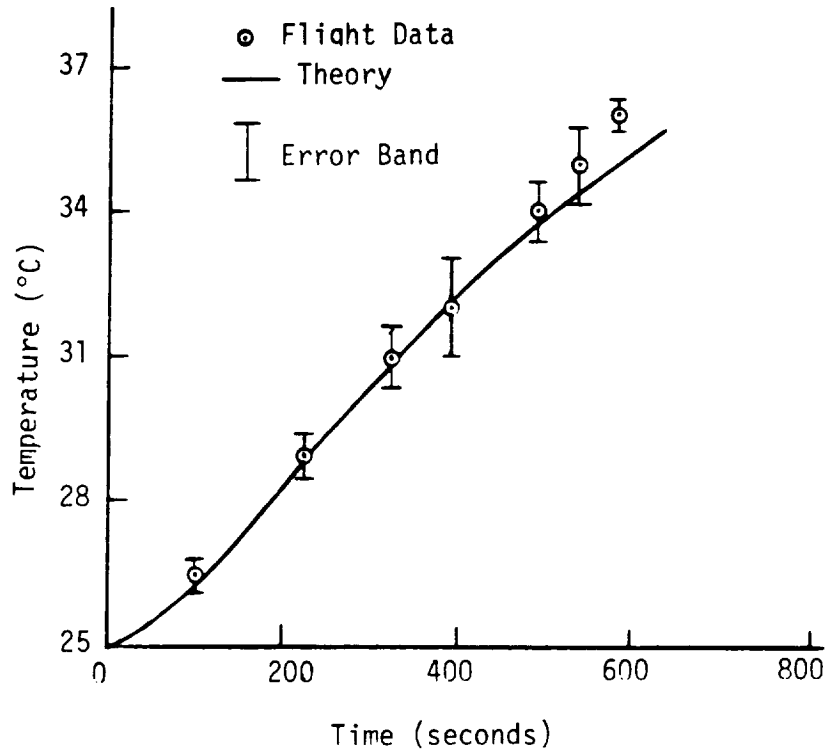

Figure II-4. Variation of Temperature With Time at 0.5 cm From The Radial Heater Post (Ref. 19).

one-dimensional heat transfer in both radial and planar models. The latter consists of two infinite parallel plates bounding a compressible newtonian fluid. The heat flow is one-dimensional and is described in a cartesian reference frame. Radiation heat transfer and viscous dissipation were neglected. Ideal gas equation was used and all thermal properties were assumed constant.

Since in this study an analytical model similar to Spradley, et al. will be employed, it is appropriate to describe in more detail this one-dimensional TAC model and formulate the applicable governing equations.

A sketch of the geometry of the problem considerd by Spradley, et al. is shown in Figure II-5.

The governing equations for this problem are:

Continuity:

$$\frac{\partial}{\partial t}(\rho') + \frac{\partial}{\partial x'}(\rho' u') = 0 \qquad (2.1)$$

Newton's 2nd Law:

$$\frac{\partial}{\partial t'}(\rho' u') + \frac{\partial}{\partial x'}(\rho' u' u') = -\frac{\partial P'}{\partial x} + \frac{4}{3}\mu' \frac{\partial^2 u'}{\partial x'^2} \qquad (2.2)$$

Energy:

$$\rho' c'_v \frac{\partial T'}{\partial t'} + \rho' c'_v u' \frac{\partial T'}{\partial x'} = -P' \frac{\partial u'}{\partial x'} + k' \frac{\partial^2 T'}{\partial x'^2} \qquad (2.3)$$

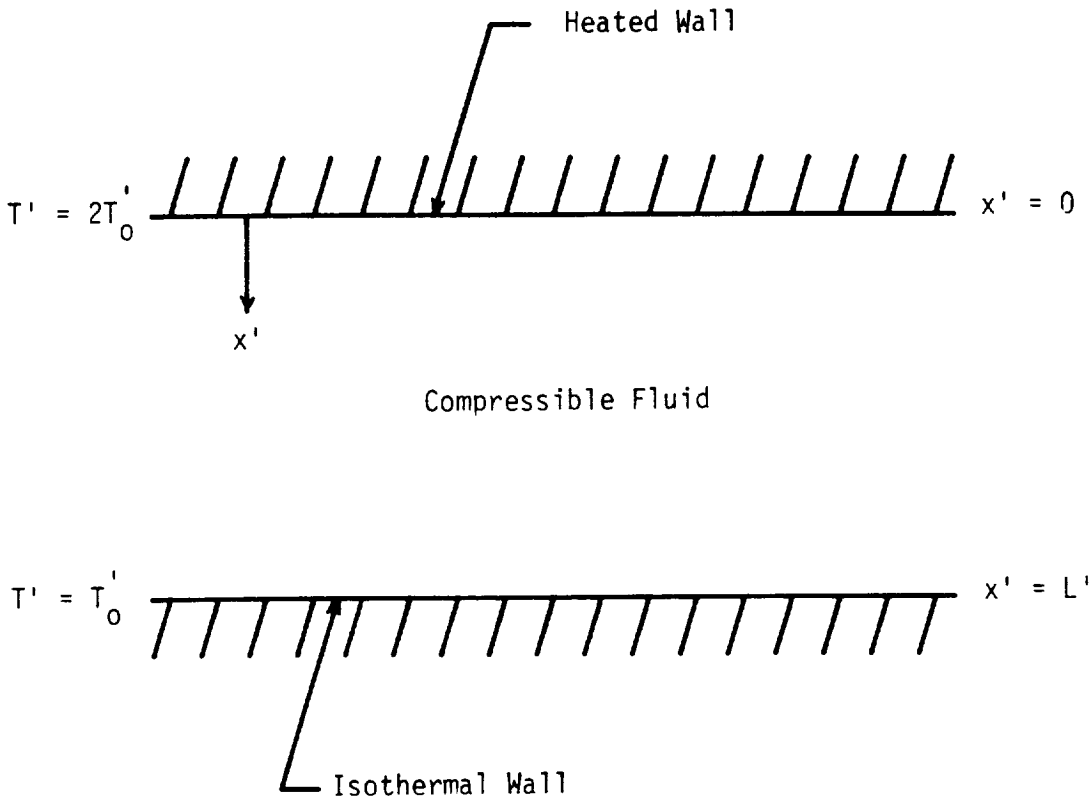

Figure II-5. Geometrical Configuration of the Infinite Parallel Plate Model.

Equation of state:

$$P' = \rho' R' T' \tag{2.4}$$

The boundary and initial conditions are:

Velocity:

$U'(x'=0, t')=U'(x'=L', t')=0$ no slip condition at the wall (2.5)

$U'(x', t'=0)=0$ Fluid initially at rest (2.6)

Temperature:

$T'(x', t'=0)=T_o'$ Initially isothermal (2.7)

$T'(x'=0, t')=T_o'$ Heated wall (2.8)

$T'(x'=L', t')=T_o'$ Isothermal wall at $x'=L'$ (2.9)

Pressure:

$\left.\frac{\partial P'}{\partial x'}\right|_{t'=0} = 0$ No body forces (2.10)

Density:

$\rho'(x', t'=0) = \frac{P_o'}{R'T'}$ Equation of state (2.11)

Equations (2.1) to (2.11) define the mathematical model for analysis of Thermoacoustic Convection in zero-gravity used by Spradley, et al. . This model is also employed in this study with appropriate necessary modifications.

Since the problem involves pressure waves which

propagate at acoustic velocity, the velocity of sound was used by Spradley, et al. as the characteristic velocity. The characteristic time used was the time required for the wave to travel the length of the container. The characteristic pressure, density, temperature, and length used in the non-dimensionalization of the equations were chosen as P_o', ρ_o', T_o', and L', respectively.

The non-dimensional equations become:

Continuity:

$$\frac{\partial \rho}{\partial t} + \frac{\partial}{\partial x}(\rho u) = 0 \qquad (2.12)$$

Newton's 2nd Law:

$$\frac{\partial}{\partial t}(\rho u) + \frac{\partial}{\partial x}(\rho u u) = -\frac{\partial P}{\partial x} + \frac{4}{3}\left(\frac{1}{Re}\right)\frac{\partial^2 u}{\partial x^2} \qquad (2.13)$$

Energy:

$$\rho \frac{\partial T}{\partial t} + \rho u \frac{\partial T}{\partial x} = -(\gamma - 1)P \frac{\partial u}{\partial x} + \left(\frac{\gamma}{RePr}\right)\frac{\partial^2 u}{\partial x^2} \qquad (2.14)$$

State:

$$P = \rho T \qquad (2.15)$$

The dimensionless initial and boundary conditions are:

$$U(x,t=0)=0 \quad , \quad T(x,t=0)=1 \quad , \quad \rho(x,t=0)=1 \qquad (2.16)$$

$$U(x=0,t)=U(x=1,t)=0 \qquad (2.17)$$

$$T(x=0,t)=T'_{\infty}/T'_{o} \qquad (2.18)$$

$$T(x=1,t)=1 \qquad (2.19)$$

The dimensionless groups which appear in the equations are:

Prandtl Number $$Pr = \frac{\mu' C'_p}{K}$$

Reynolds Number $$Re = \frac{L'\sqrt{R'T'_o}}{\mu'}$$

Peclet Number $$Pe = Re \cdot Pr$$

Ratio of specific heats $$\gamma = C'_p / C'_v$$

An explicit finite difference scheme was applied to solve the dimensionless equations. The unsteady form of the equations was used to study the transient behavior of the problem. The explicit approach with the unsteady equations allowed a forward-marching algorithm in time to be employed. Forward time differences were used on the unsteady terms and space centered differences were used on all space derivatives except the convection terms where a "flip-flop" forward-backward scheme was used to eliminate numerical instability.

The results obtained by Spradley, et al. are presented in Figures II-6 and II-7.

Figure II-6 shows the calculated dimensionless velocity profile as a function of time for the first 400 time steps using a time increament of 5×10^{-6} seconds. This figure shows an oscillatory behavior for the fluid velocity. The small period of oscillation of the fluid velocity clearly indicates the acoustic nature of the fluid motion.

The calculated spatial temperature profile at $t=0.2$ seconds is shown in Figure II-7. This figure shows much higher temperature values than those obtained by pure conduction solution. At $t=0.2$ seconds the calculated temperature profile is seen to be much closer to steady state values than a solution corresponding to pure conduction heat transfer mode. These results indicate that TAC is an effective heat transfer mechanism in enhancing the rate of energy transport.

The solution for the temperature field obtained by Larkin [17] is also presented in Figure II-7. It is interesting to note that although the maximum amplitude of velocity for the first few waves calculated by Larkin are one order of magnitude higher than that calculated by Spradley, et al. the temperature profiles obtained by both methods are in perfect agreement.

Krane and Parang have performed a scaling analysis

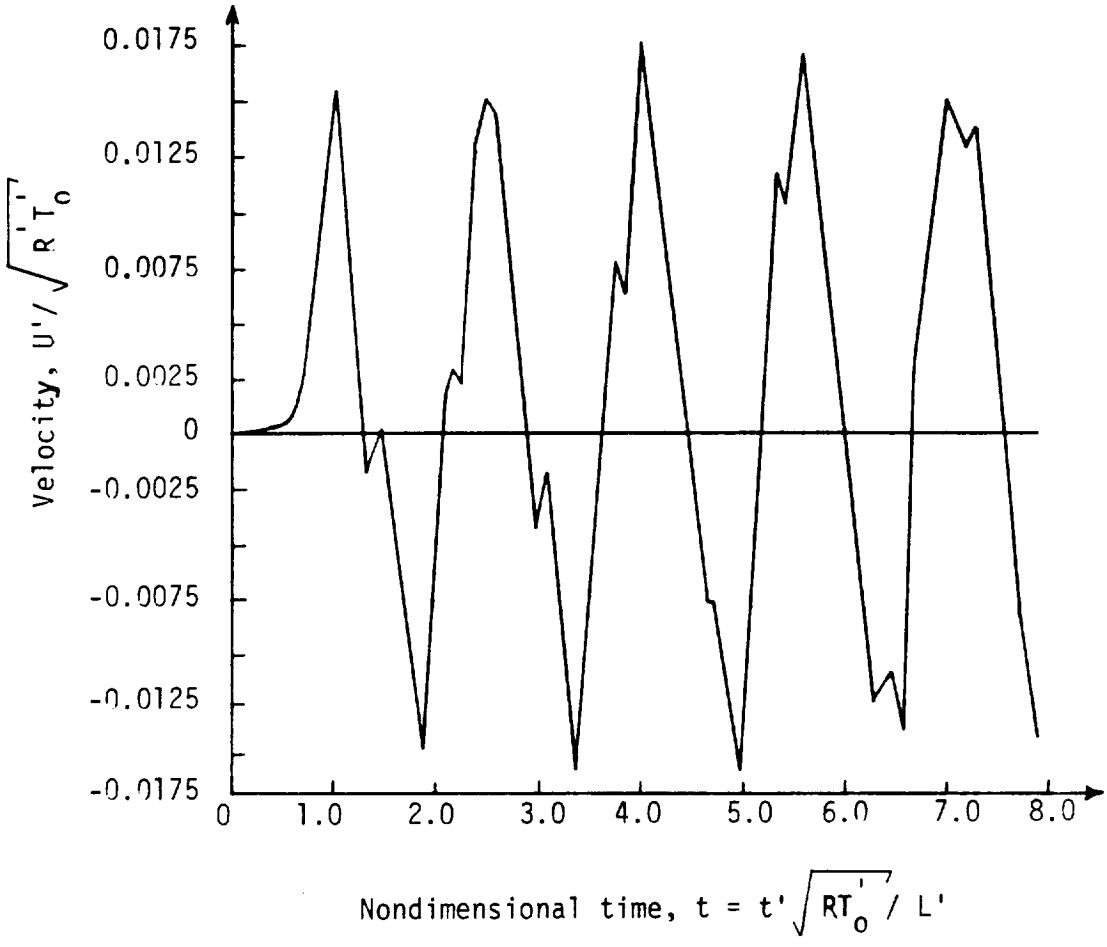

Figure II-6. Variation of Velocity With Time at Midpoint Between the Plates (Ref. 20).

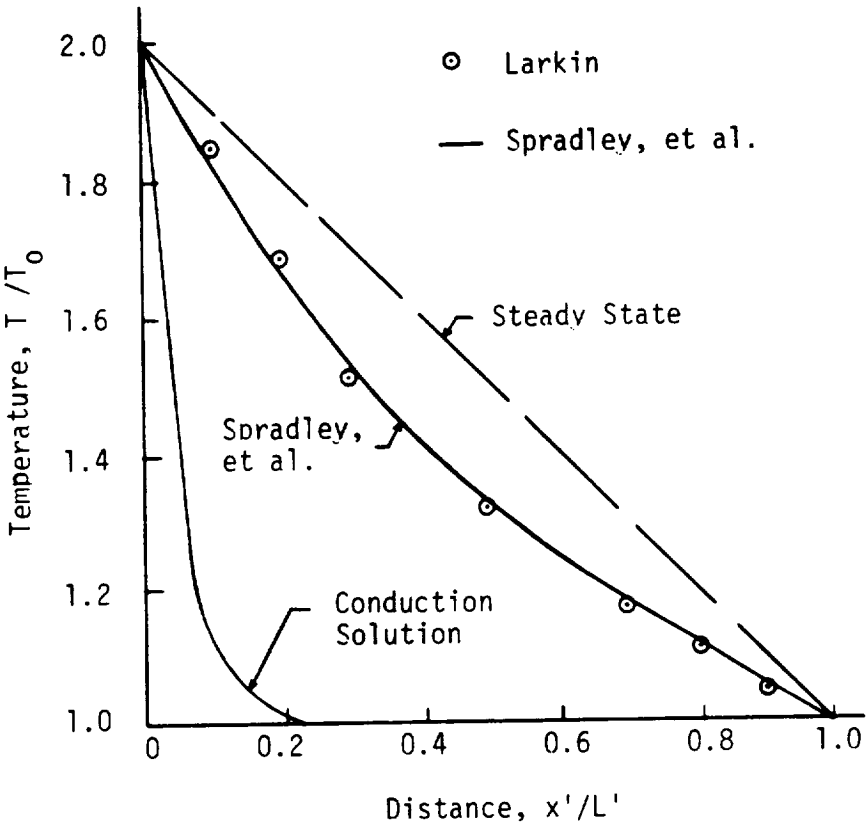

Figure II-7. Variation of Temperature With Time at 0.2 Seconds (Ref. 20).

of this problem [21], using the same one-dimensional model as in Spradley, et al.. This study accomplishes several objectives. First, it proves conclusively that dissipation terms in the energy equation remain small throughout the heating process. Second, the study shows that a small non-dimensional parameter exists in the problem which represents the ratio of the characteristic time for TAC heat transfer process to that of the characteristic time of heat diffusion by conduction. Finally, the dominant terms in the governing equations are determined and the equations are simplified. Krane and Parang, however, do not solve the simplified equations.

CHAPTER III

THE EXPERIMENTAL INVESTIGATION

Design Of The Experimental Apparatus

The apparatus consists of a cylinder containing air as the compressible fluid. The side wall of the cylinder was insulated to insure a one-dimensional heat flow. The bottom wall could either be placed in contact with dry ice to cool the air inside or be allowed to remain at the ambient temperature. To eliminate buoyancy effects in ground experiments, the top surface of the cylinder was chosen as the boundary subject to heating. Battery packs were used to supply electric power to the heater. Using a series of thermocouples, the transient temperature of the enclosed air was measured at four locations along the axis of the cylinder during the heating process. The output of the thermocouples were displayed on Omega model 450-AET digital thermometers. These displays were filmed during the flight using a high speed camera. A control circuit was designed and constructed to initiate and terminate the heating process and to operate the camera and lights. As shown in Figure III-1, the apparatus was mounted on an aluminum frame which was dropped in the 2-seconds Zero-Gravity Drop Tower Facilities of NASA Lewis Research Center.

The fluid container that was used in the

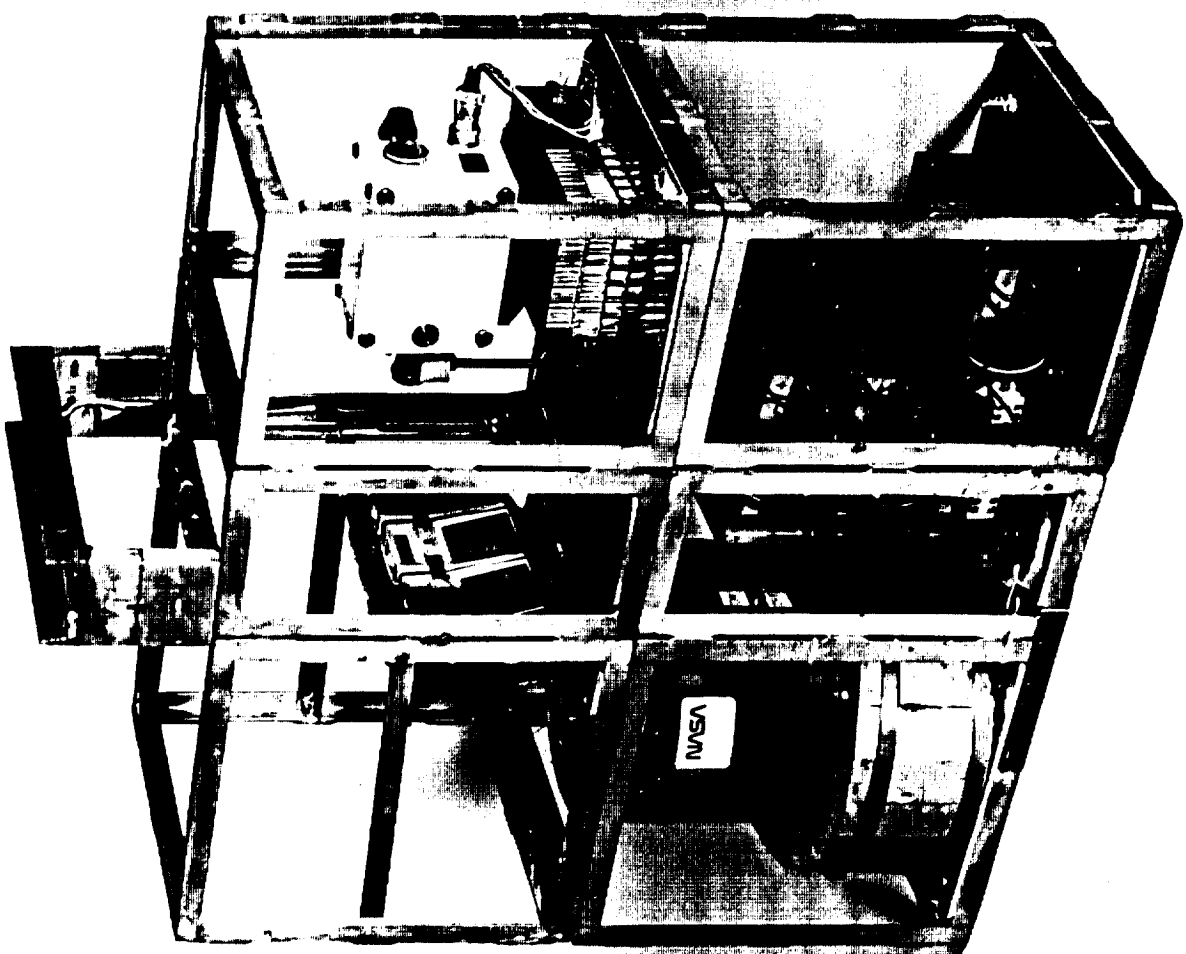

Figure III-1. The Experimental Apparatus

experimental investigation of TAC is a steel circular cylinder with a diameter of one foot. In order to determine the effects of container geometry on TAC, the cylinder was designed such that its height could be set at either one foot or one-half foot. Sheets of fiberfrax ceramic insulation were glued to the side wall of the cylinder (Figure III-2). The insulation average thermal conductivity and thickness were 0.066 Btu/Hr. Ft.^{o}F and 0.25 in., respectively. To maximize the effects of TAC, dry ice could be used to cool the bottom surface. However, early tests showed that even without using this option large temperatures differences could be imposed on the air and thus dry ice was not used in the experiments.

The design of the heating element was the most important and critical task in the investigation. A great effort was devoted to insure that the rate of increase of temperature at the heated surface would be as high as possible. Furthermore, this rapid increase in the surface temperature had to be achieved within the two seconds of experimental time and the battery pack weight limitations imposed by the flight. The heating element consisted of a stainless steel foil (type 301) connected to the packs of batteries. The foil electric resistance and thickness were o.1 ohm and 0.001 in., respectively. As shown in Figure III-3, the 6 x 12 in.

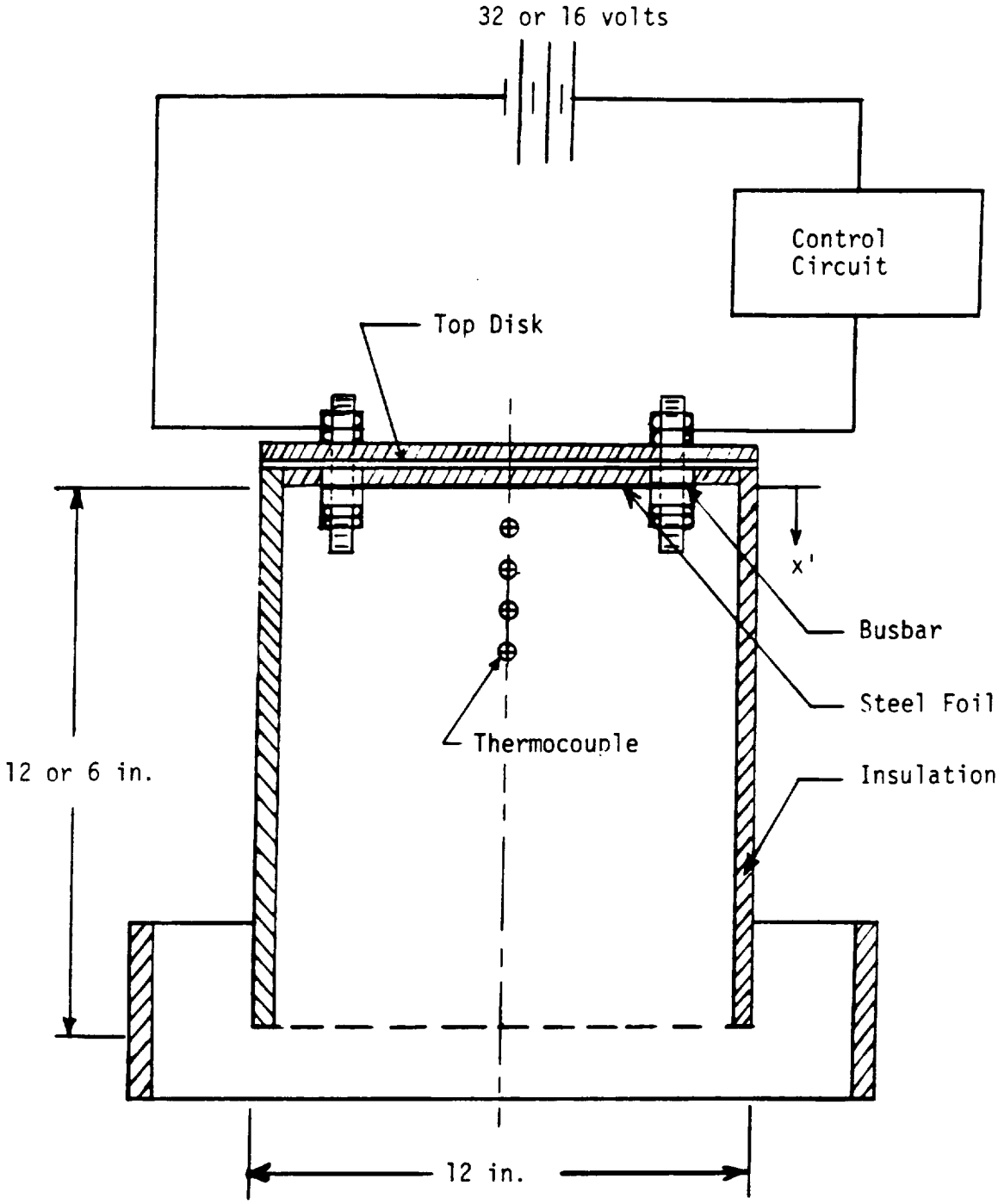

Figure III-2. Schematic Diagram of the Experimental Apparatus.

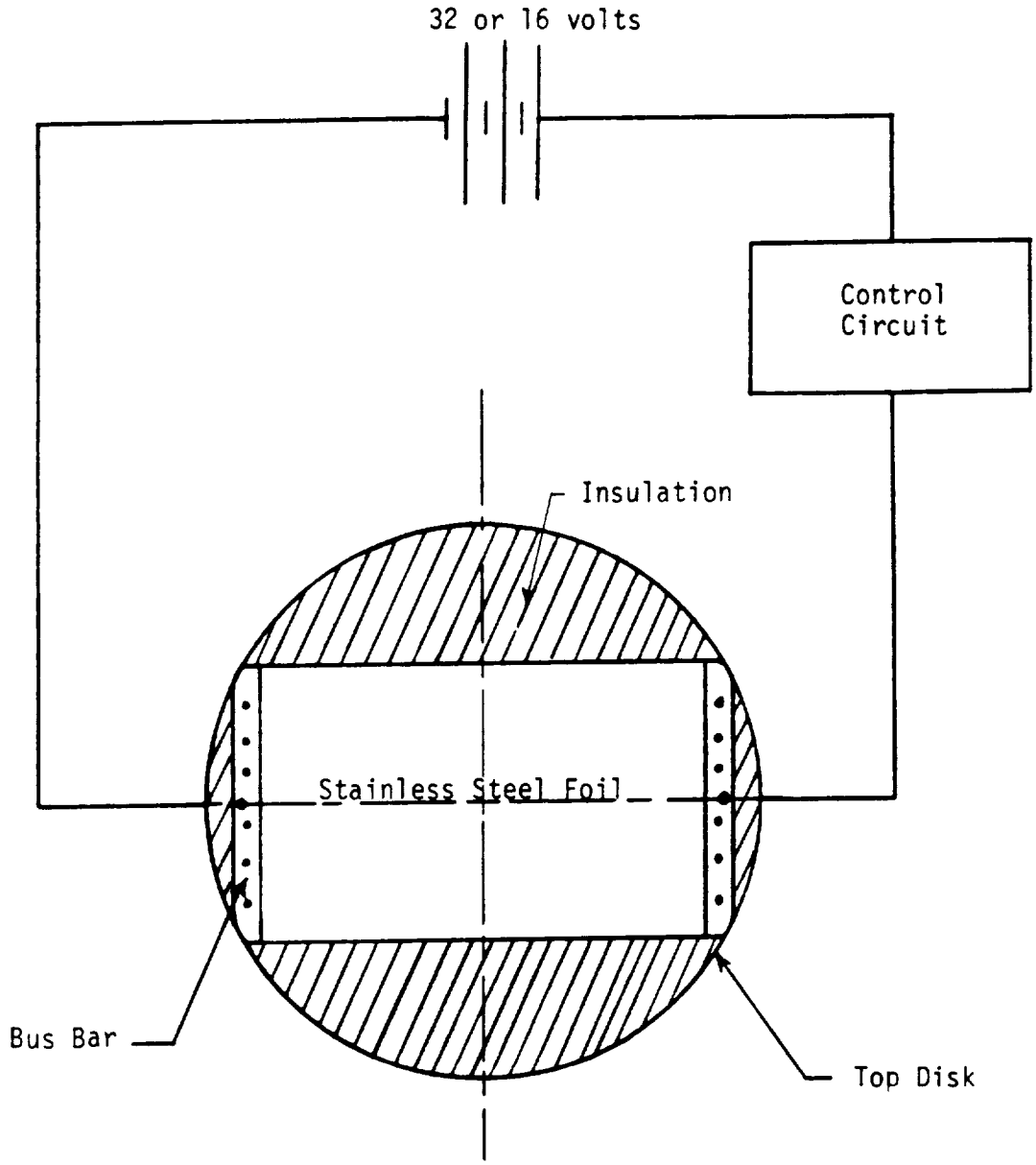

Figure III-3. Schematic Diagram of the Heating Element.

foil was attached to copper busbars to maintain a uniform flow of electric current during heating. These busbars were fastened to the top disk of the cylinder by means of six bolts for each busbar as shown in Figure III-4. Lead acid batteries were used to heat the steel foil. These batteries can release a large amount of power over a short period of time. Two battery packs were connected in parrallel to insure minimum variation of the power input to the foil during the heating process. The voltage across the foil was measured prior and during the heating. The two different battery packs used as the power source in the experiments provided 32 volts and 16 volts potential difference across the foil. Since the resistance of the heating foil prior to the heating was known, the initial nominal power input to the foil for the two settings were calculated to be 3610 and 1210 watts. This arrangement produced power inputs and heating surface temperatures far exceeding that used in the Apollo 17 HFC expereiments (by one to two order of magnitudes for power). The surface temperature of the foil which was measured directly throughout the experiments was used in all the subsequent calculations and the results presented in this study. Therefore, the initial power input values given here are not used in any calculations and are presented here only to emphasize the power settings available in the experiments. Typical

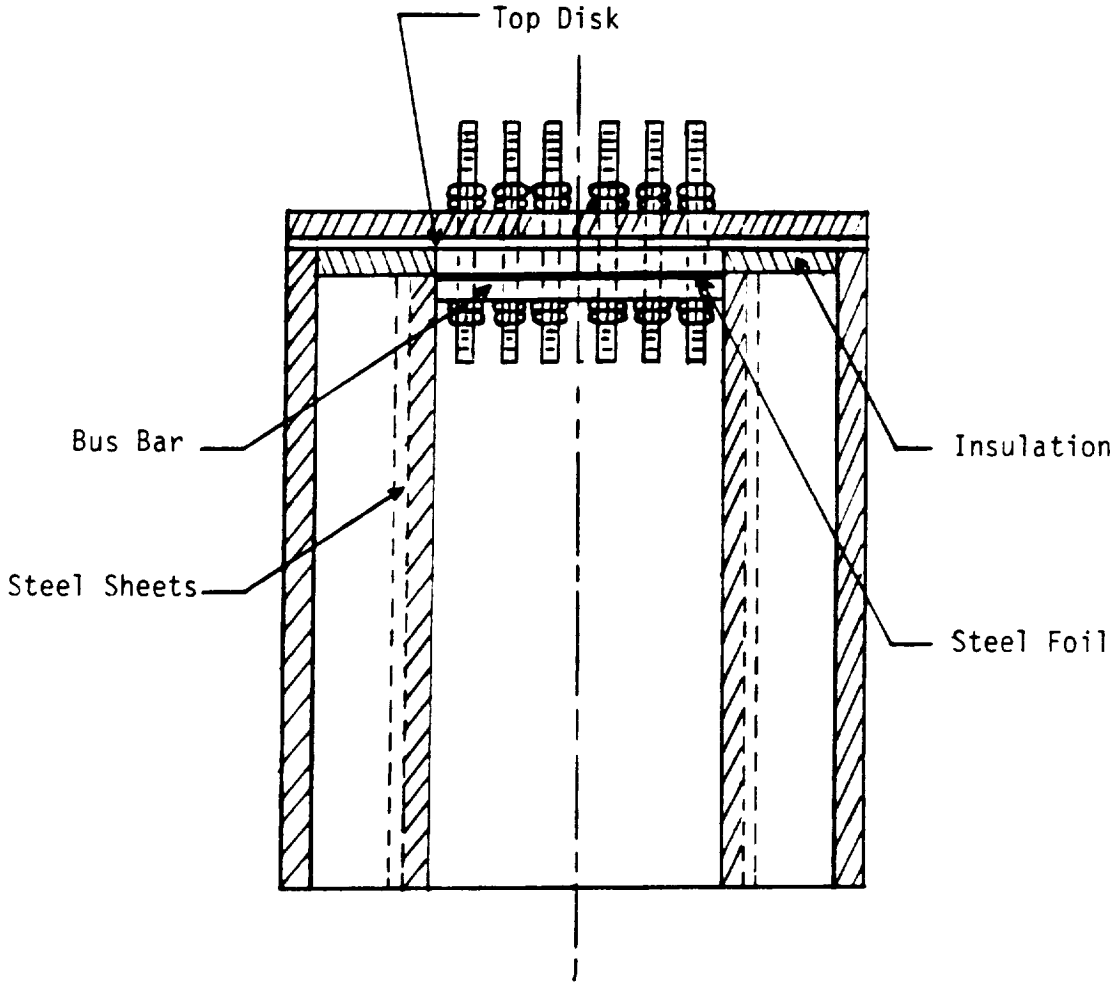

Figure III-4. Schematic Diagram of the Experimental Apparatus (Side View).

plots of the transient foil temperatures for two voltage settings are presented in Figure III-5. The sharp rise in the foil temperature was sufficient to produce a notable rise in the air temperature near the heated surface. Since the steel foil did not cover the entire area of the disk, two insulated sheets of steel were used to enclose the air directly under the heater surface (see Figure III-4).

The air temperature was measured using type E (chromel-constantan) thermocouples. since the duration of the experiments was only two seconds, thermocouples with very fast response were employed. The diameter of the thermocouple is 0.001 in. and its time constant is 0.05 seconds. With x' defined in Figure III-2, four thermocouples were placed along the cylinder axis at x'=1 in., 2 in., 3 in., and 4 in. for a cylinder height of 1 ft. and at x'=0.5 in., 1.0 in., 1.5 in., and 2.0 in. for a cylinder height of 0.5 ft. . Also, using the facilities at NASA-Lewis Research Center a thermocouple was carefully spot welded at the center of the stainless steel foil to measure its transient temperature during heating. Three digital thermometers were used to display the output of the thermocouples. These thermometers can only display three readings per second and therefore during the zero-g drop, an average of six temperature readings were recorded for every thermocouple location.

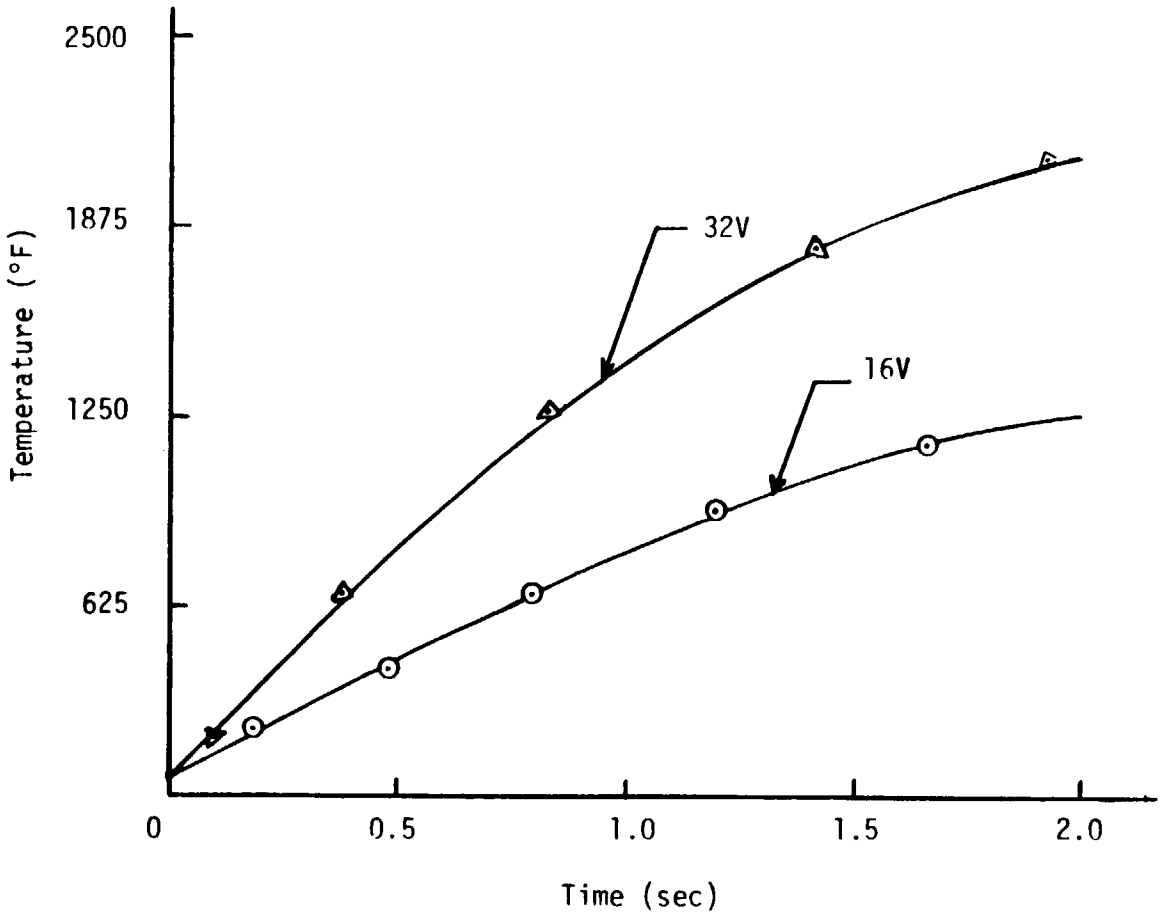

Figure III-5. Typical Heating Element Surface Temperature For Two Voltage Settings Used in the Experiments.

Before each zero-gravity experiment, the experimental apparatus was placed inside a special heavy metallic shield for drag reduction and was completely closed and balanced before dropping in the Drop Tower Facility at NASA-Lewis Research Center. A control circuit was designed to operate the electrical parts of the apparatus. A schematic diagram of the circuit is presented in the Appendix A. Using three switches located outside the shield and on the top floor of the drop tower, the heater and the camera were operated without disturbing the balance of the shield. The circuit was designed to perform the following tasks:

1. to automatically turn the heater on at a preset time prior to the start of the drop. The preset time varied from ten seconds (for preheating) to zero seconds (no preheating).

2. to start the camera approximately five seconds before dropping the apparatus, thus, allowing the camera motor to reach a uniform speed.

3. to turn on the camera lights when heating is initiated.

4. to trigger a timer that automatically shuts off the lights, the camera, and the heater three second after the start of the drop.

Using the same experimental apparatus, measurements of the enclosd air temperature were made in the gravity

environment to determine the effects of gravity on TAC heat transfer.

In order to verify the accuracy of the thermometers, a series of temperature measurements were performed under gravity conditions using Hewlett Packard model 3497A Data Acquisition System (DAS) and Hewlett Packard model 9826 computer. The HP 3497A can measure temperatures at a speed that is 4 times faster than the the speed of the digital thermometers. Also, the response time of the data acquisition system is much faster than that of the thermometers. Therefore, the magnitude of the error due to the instrumentation is much smaller when this data acquisition system is employed. In these experiments three thermocouples were used to measure the transient temperature of the confined air and the stainless steel foil. The DAS was employed to measure the transient thermoelectric voltage across each thermocouple. The Hp 9826 computer is equipped with an internal clock which was used to determine the time of the voltage measurements. A computer program was developed to read and store the voltage-time data during heating. When the heating process was terminated the voltage data was recalled and the equivalent temperature was calculated using a polynomial curve fit equation. The output was obtained in the form of time-temperature tables and temperature verses time curves for the three

thermocouples. To verify the accuracy of the thermometers, several runs were performed using the Hp data acquisition system and the Omega digital thermometers simultaneously. The computer program used and a sample of the results are presented in the Appendix B. The results show that the temperature data obtained using the thermometers are in reasonable agreement with the data recorded by the computer.

In order to improve the accuracy of the data obtained using the thermometers, a data correction procedure was developed to reduce the experimental error introduced by the time delay of the thermometers. This time delay is the time interval between the instant a temperature measurement is made and the instant the value of this measurement is displayed. The data was modified by considering the temperature displayed at time t to be the temperature measured at time $(t' - \Delta t'/2)$, where $\Delta t'$ is the time interval between the last two readings. This procedure was applied to the temperature-time data obtained using the thermometers. Since the response time of the data acquisition system is very short, the correction procedure was not applied to the data recorded by the computer . Finally, the corrected data for three runs were also compared to the computer output. The results indicate that the corrected data is in good

agreement with the HP data and therefore the error due to the thermometers response time is eliminated.

Experimental Procedure

The heater batteries were charged for 20-30 minutes following each drop. During this time a thorough check of all the parts of the apparatus was performed. The heating element was disengaged from the power source and the open-circuit voltage of the heater batteries was measured and recorded before and after recharging. The wiring of the heater was thoroughly checked prior to each experiment. The lights and timer were also checked by operating the circuit while the heater and the camera were disconnected. To determine the initial nominal power input to the heater for the two voltage settings used, the closed-circuit voltage of the heater batteries was measured during the experiments performed under gravity conditions. When the enclosed air temperature reached a uniform value, the apparatus was dropped in the 2-seconds Zero-Gravity Drop Tower Facility at NASA-Lewis Research Center.

Keeping the thermocouple attached to the heater was the only major problem encountered during the experiments. Due to the high foil temperature and the impact effects, the thermocouple was frequently breaking upon impact. The problem was partially resolved, however,

by using a thermocouple of the same type with a slightly larger diameter (0.002 in.).

Experimental Results

The results of the experimental investigation are presented in Figures III-6 to III-23. These results were derived from forty experimental runs in which the cylinder height and the heating rate were varied. Twenty of these runs were performed under zero-gravity conditions. Several runs were repeated three times to insure the consistency of the data and the accuracy of the results. Each figure consists of three curves showing the measured non-dimensional air temperature at two locations near the heated surface and the transient heater temperature. Some of these figures represent the data obtained from two or three repeated runs performed under the same voltage setting and cylinder height. The air temperature was non-dimensionalized using the average heater temperature and the initial air temperature for each run. Thus, the non-dimensional air temperature was chosen as:

$$\bar{T} = \frac{T' - T_0'}{T'^* - T_0'}$$

Where T'^* and T_0' are the average heater temperature and the initial air temperature, respectively.

Figures III-6 and III-7 show the non-dimensional air temperature measured during free fall at $\dot{x}$=1 in. and $\dot{x}$=4 in. . The low voltage setting (16 volts) used produced a foil temperature near 1275 ^{o}F at $\dot{t}$= 2 seconds. The transient heater temperature is also shown in Figures III-6 and III-7. The height of the cylinder was set at 1 ft. Although these figures represent the data obtained during two similar runs performed under the same conditions, the results were plotted on two separate graphs due to the notable difference in the average heater temperature calculated for these runs. This difference in the average foil temperature was caused by the amount of energy released by the batteries. It is near impossible to recharge the batteries to the same previous level following each run, thus, it is difficult to perfectly control the power input to the foil. However, some of the repeated runs show almost identical results. Figure III-8 represent the data obtained from two runs performed in the gravity environment. The same experimental case was employed, that is low voltage setting and long cylinder height. This figure confirms the consistency of the results since the data recorded during both runs are in good agreement. It is clear that a significant rise in the air temperature was produced even for the low power setting.

The air temperature measured at $\dot{x}$=2 in. and $\dot{x}$=3

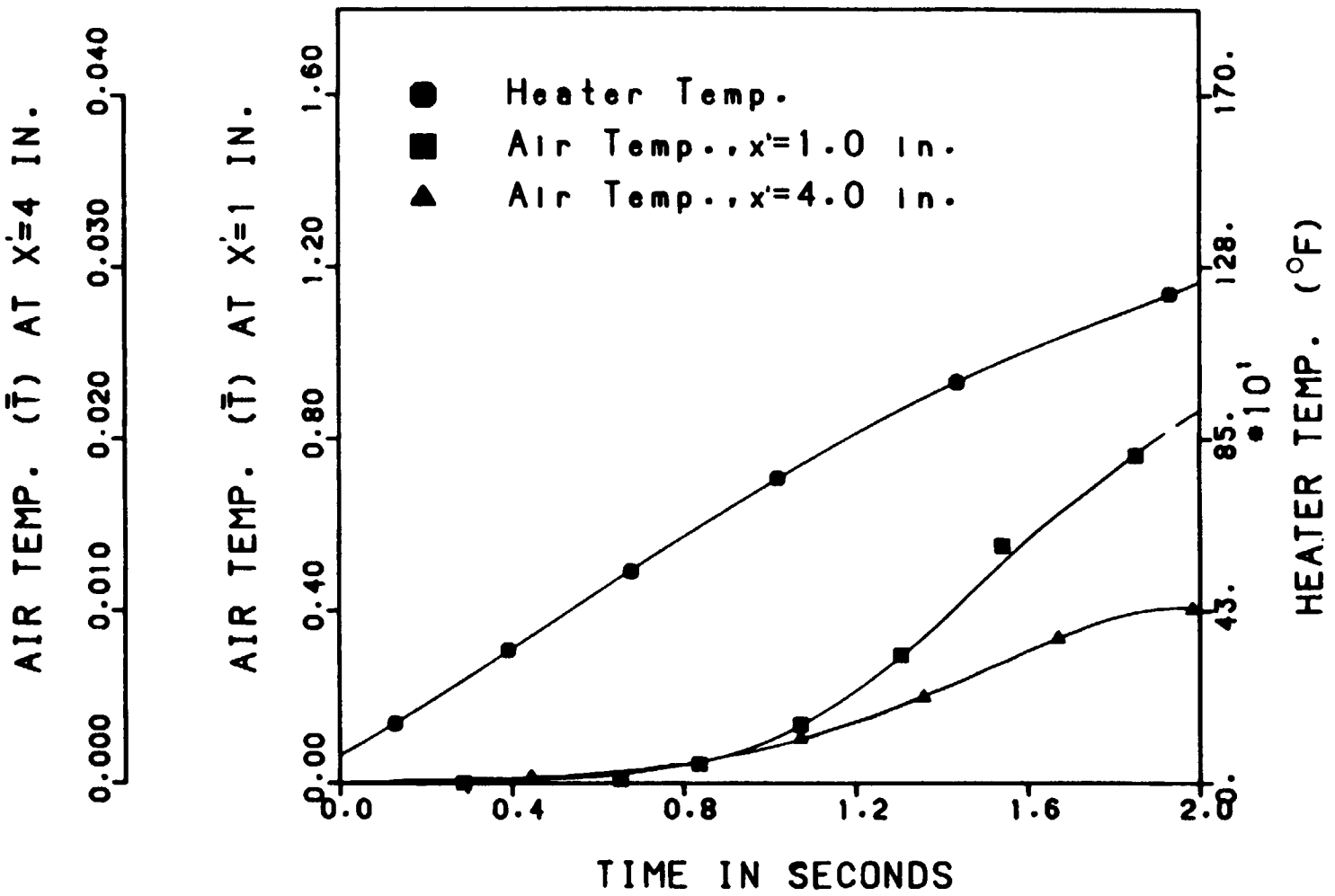

Figure III-6. Variation of Temperature in Zero-Gravity as a Function of Time With V_i' =18 Volts, L'=12 in., T'^* = 665 ° F, and T_o' =69 ° F.

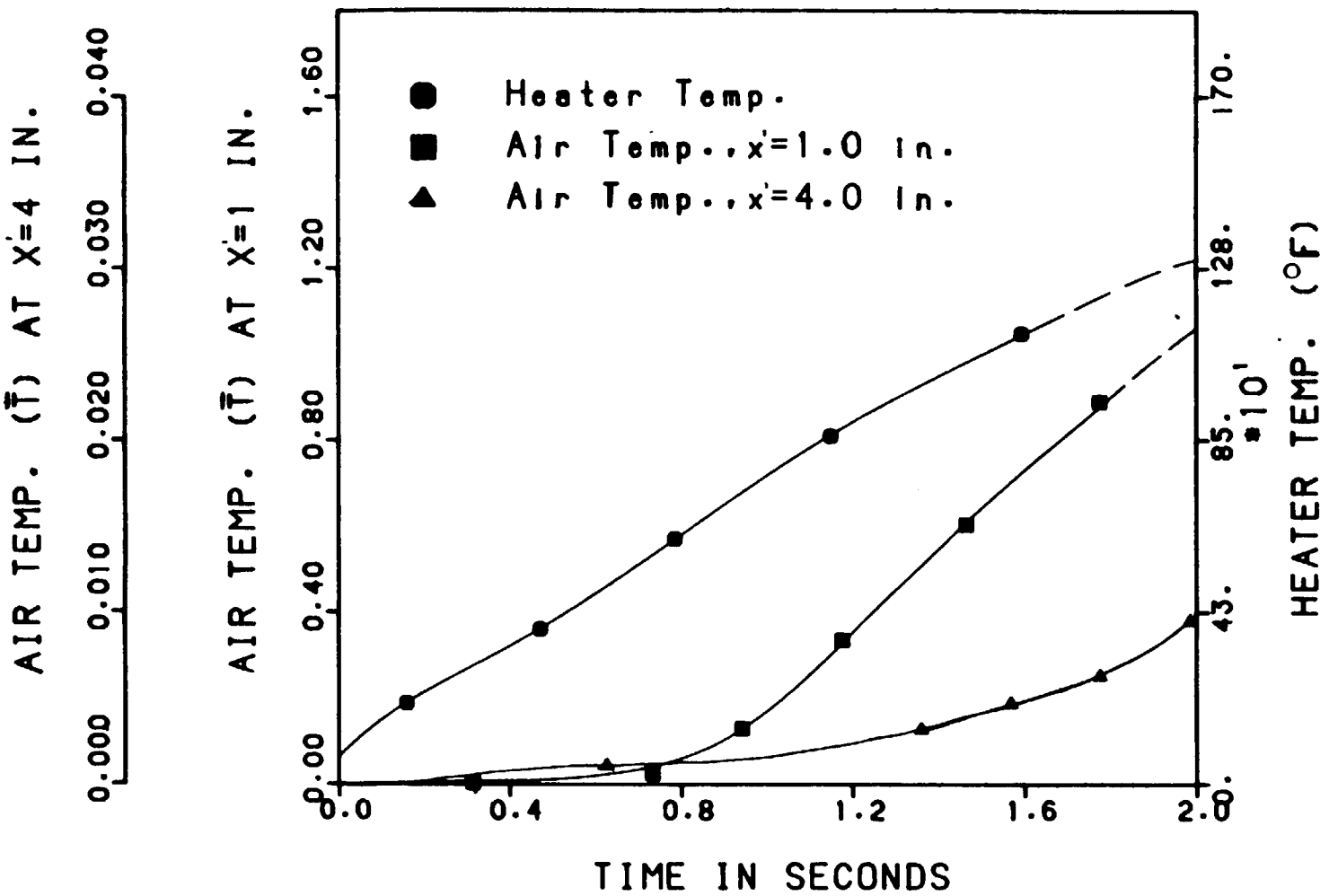

Figure III-7. Variation of Temperature in Zero-Gravity as a Function of Time With V_i'=18 Volts, L'=12 in., T'^*= 703 ° F, and T_o'=69 ° F.

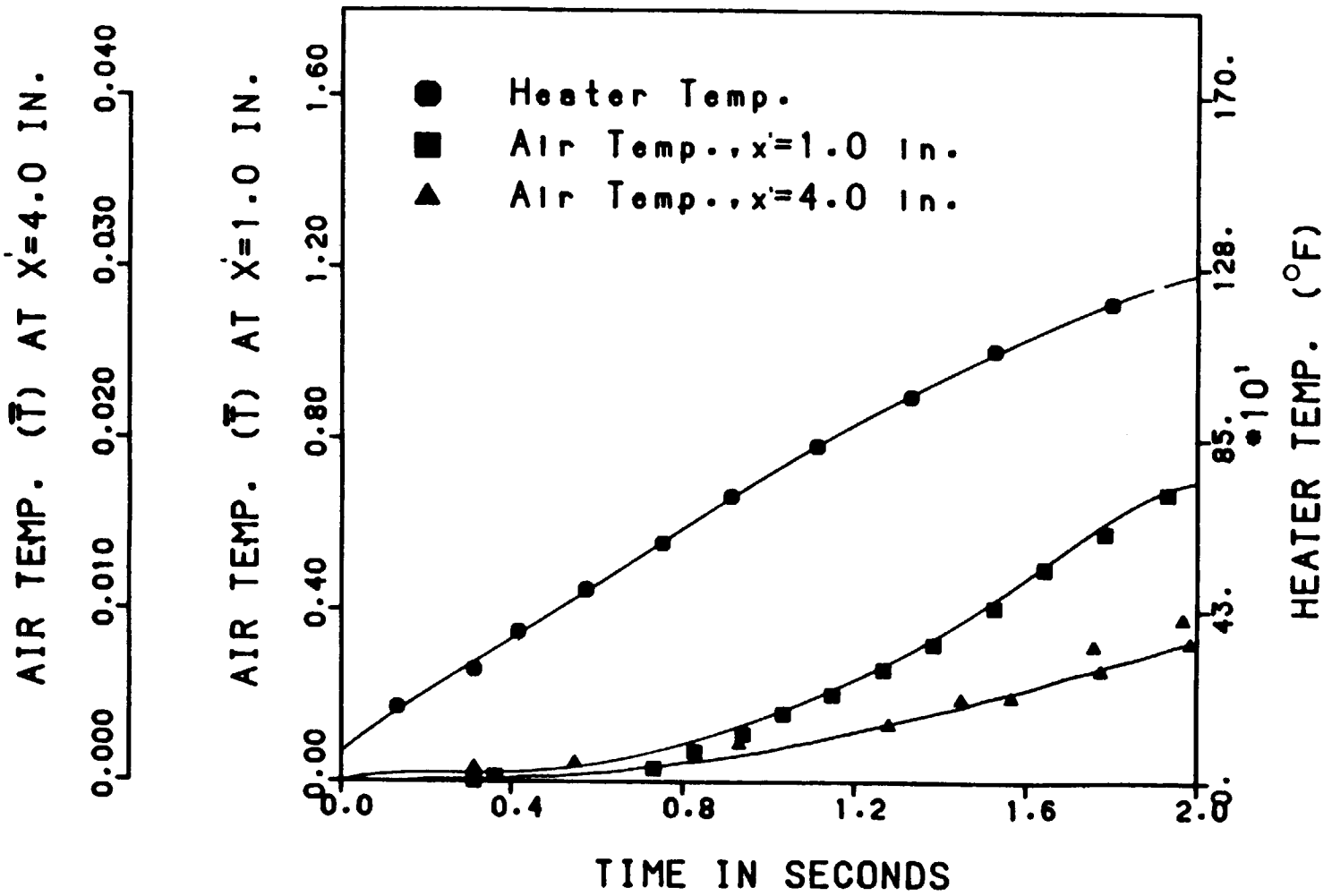

Figure III-8. Variation of Temperture in the Gravity Environment as a Function of Time With V_i'=18 Volts, L'=12 in., T'*= 701 °F, and T_o' =71 °F.

in. is shown in Figures III-9 and III-10. Low voltage setting was used and the cylinder height was kept at 1 ft. . Figures III-9 and III-10 show the results obtained in zero-gravity and gravity environments, respectively. Each figure was derived from two similar runs. It is interesting to note that although the heater temperature was higher in the zero-g runs, the air temperature measured under gravity conditions shows higher values than those obtained during free fall.

Figures III-11 and III-12 present the data obtained for the low voltage setting (16 volts) and short cylinder case (0.5 ft.). The air temperature was measured at x'=0.5 in. and x'=2.0 in. . The data generated by performing three repeated runs were used to plot each figure. The results show that, under both gravity and zero-gravity conditions, the non-dimensional air temperature rise at x'= 2.0 in. increases in the early heating stage and then decrease during the rest of the heating process. This behavior, however, does not occur at x'= 2.0 in. .

With the thermocouples placed at x'= 0, x'= 1.0 in., and x'= 1.5 in., the results of the temperature measurements performed at low voltage setting and at 0.5 ft. cylinder height are presented in Figures III-13 and III-14. These figures show the data obtained in zero-g and gravity fields. Unlike Figures III-11 and III-12 which show an increase and then decrease in the

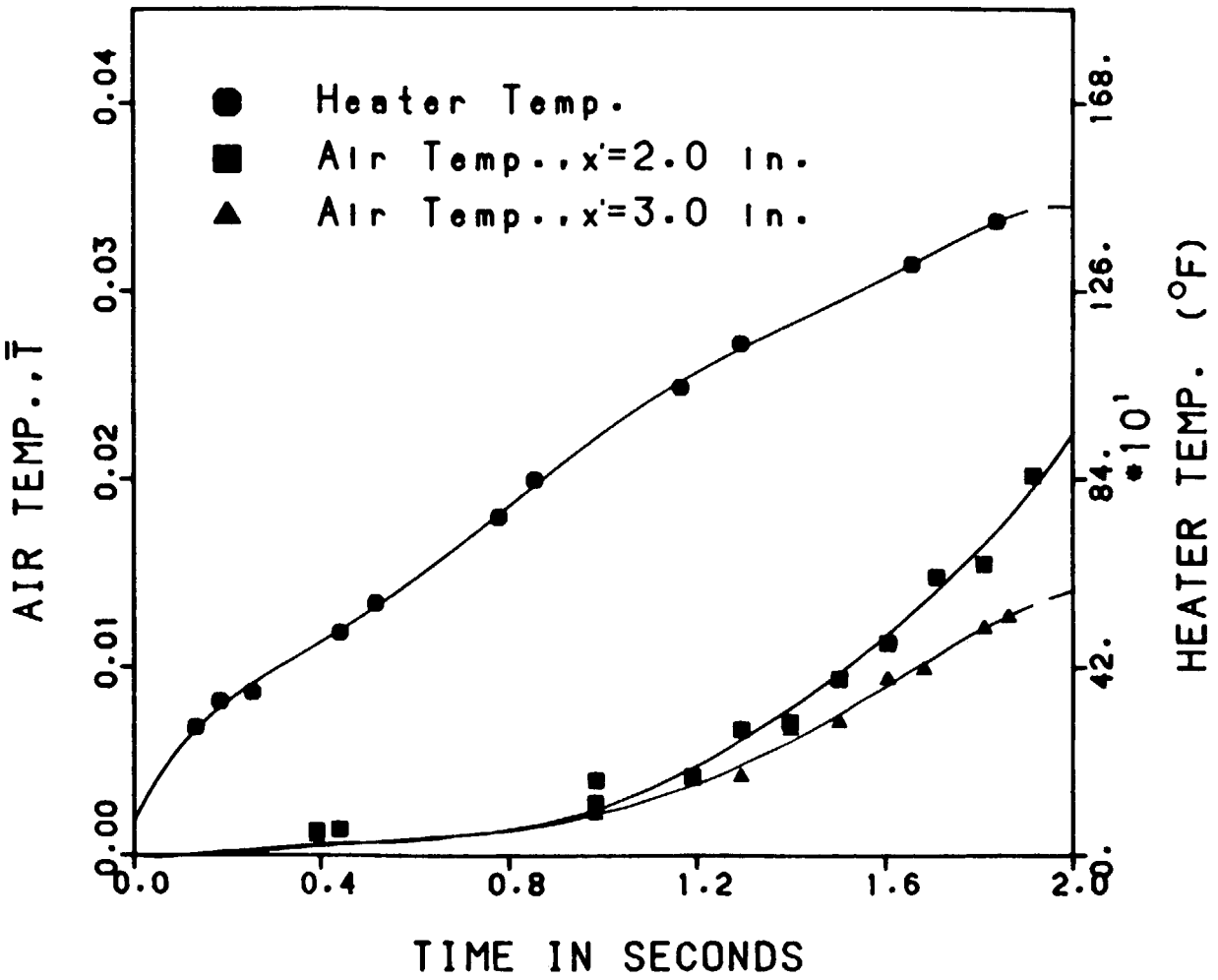

Figure III-9. Variation of Temperature in Zero-Gravity as a Function of Time With V_i'=18 Volts, L'=12 in., T'^*= 783 °F, and T_o'=74 °F.

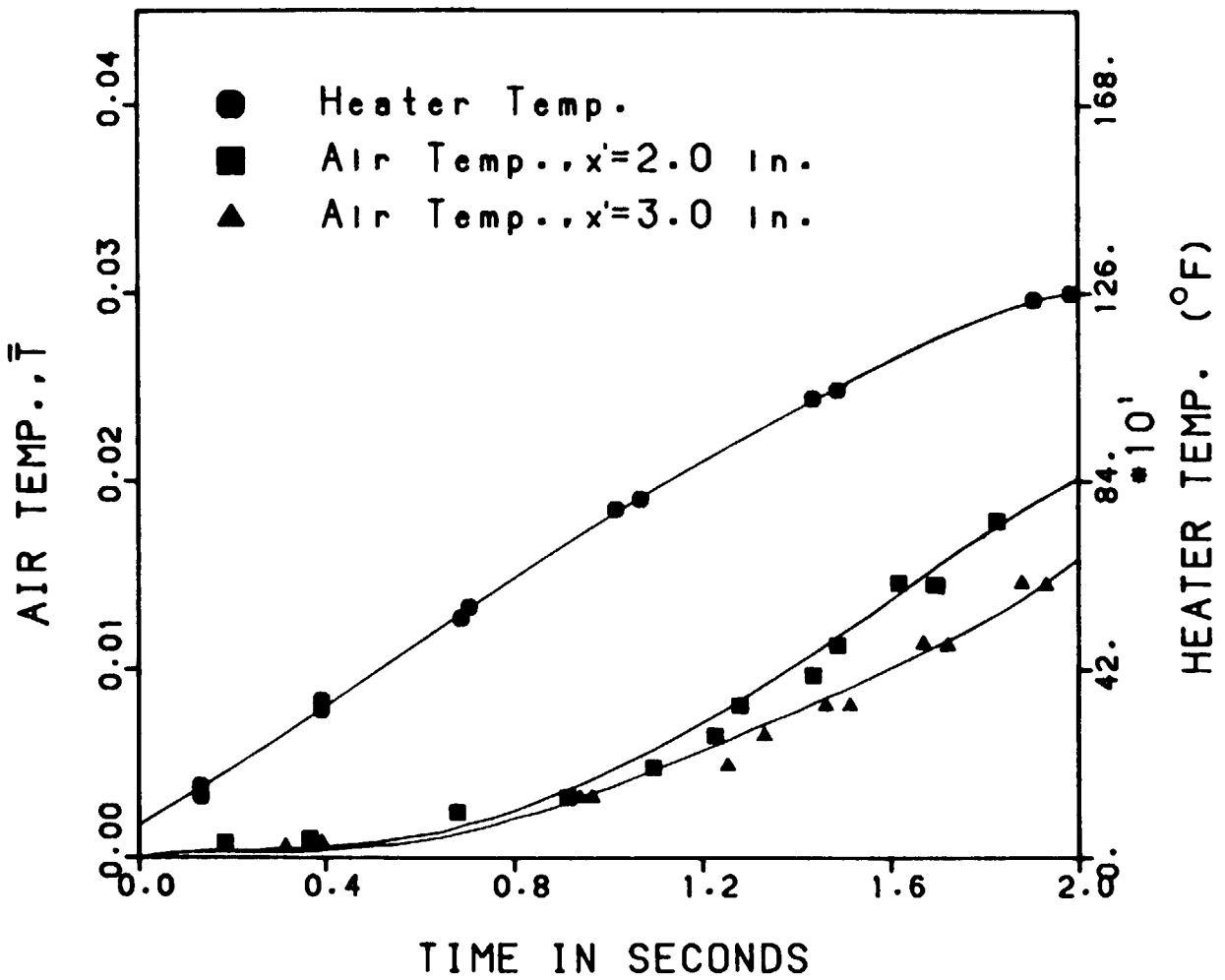

Figure III-10. Variation of Temperture in the Gravity Environment as a Function of Time With V_i'=18 Volts, L=12 in., T'^*= 687 °F, and T_O'=73 °F.

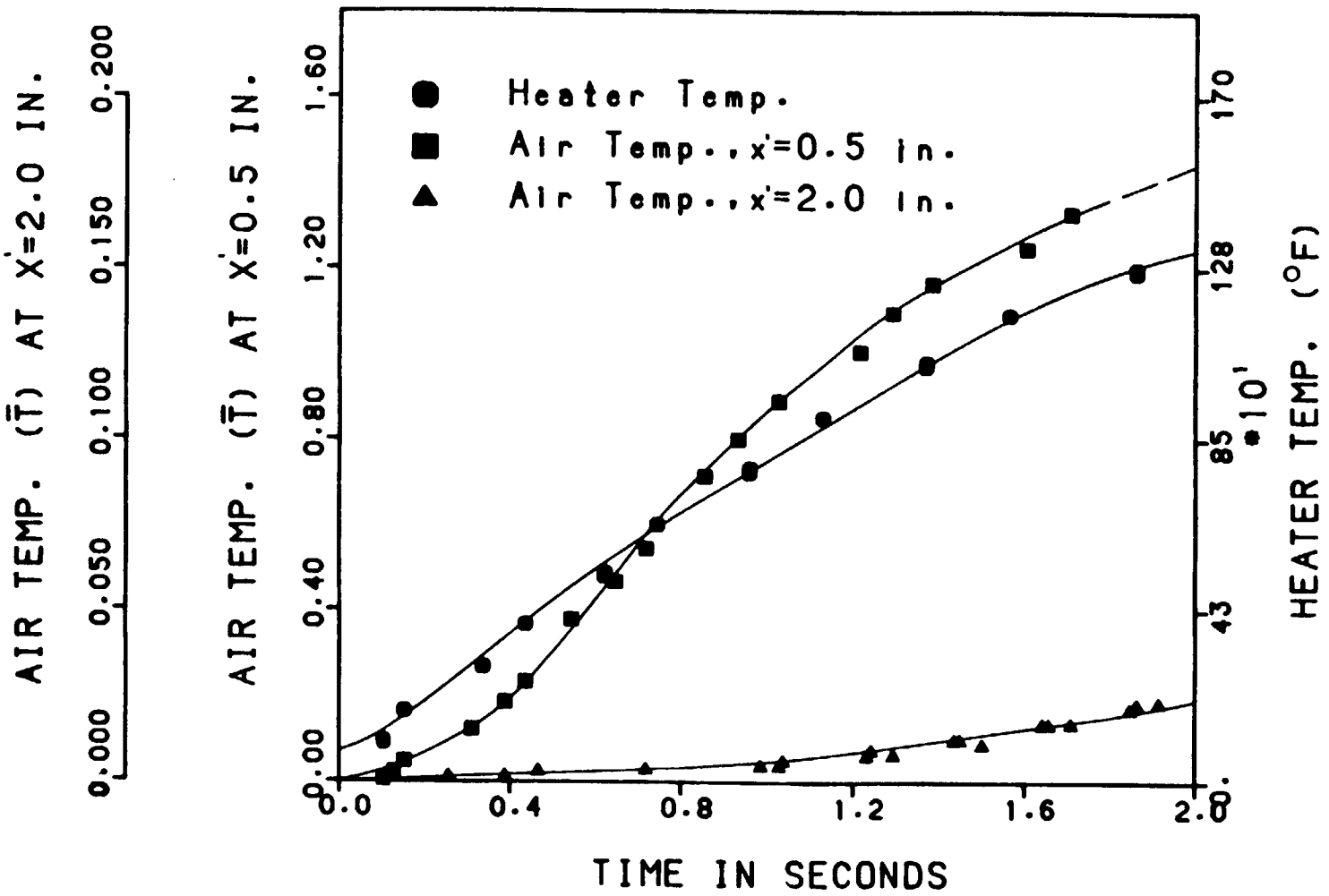

Figure III-11. Variation of Temperature in Zero-Gravity as a Function of Time With V_i' =18 Volts, L'=6 in., T'*= 735 °F, and T_o' =73 °F.

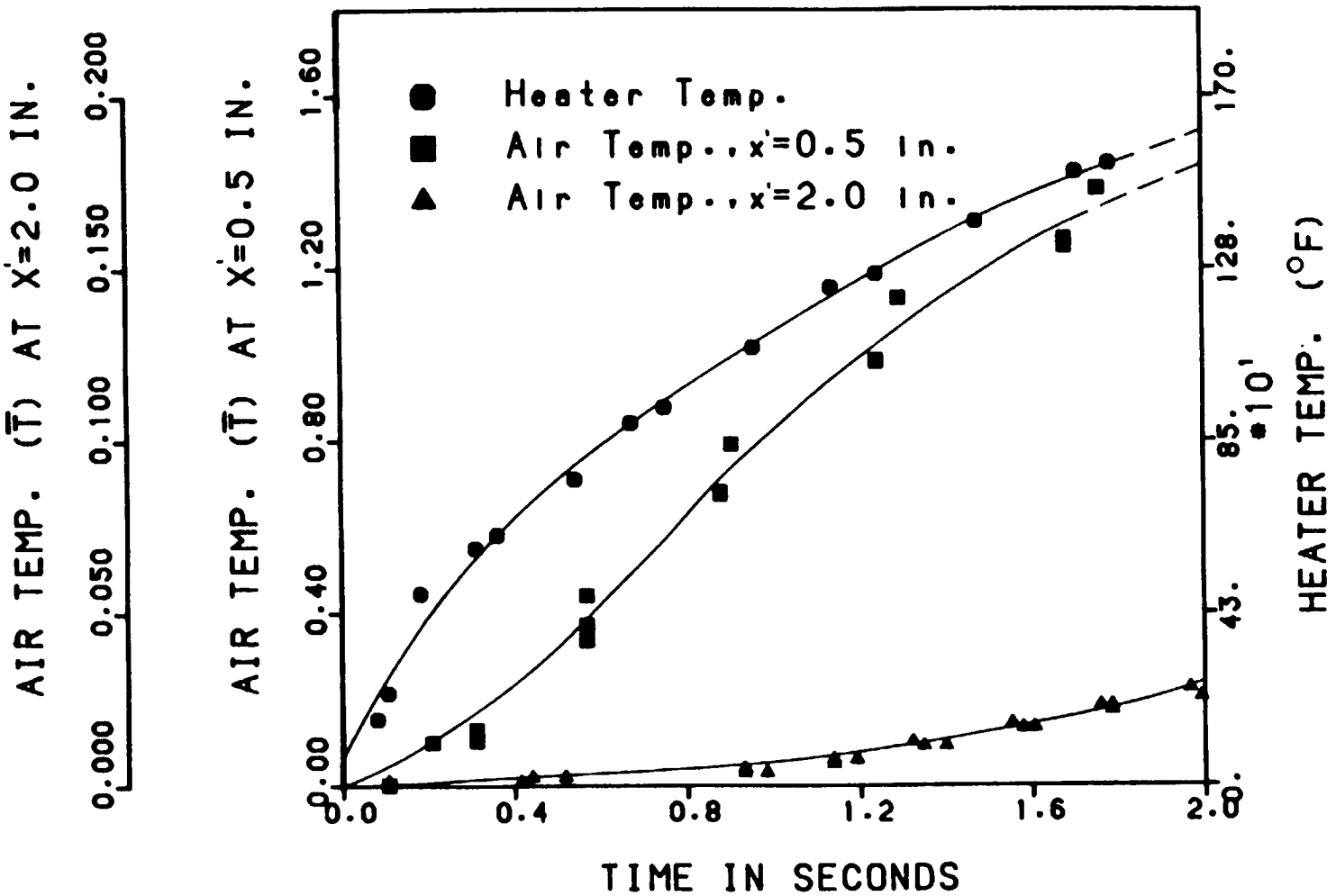

Figure III-12. Variation of Temperture in the Gravity Environment as a Function of Time With V_i'=18 Volts, L'=6 in., T'^*= 852 °F, and T_o'=73 °F.

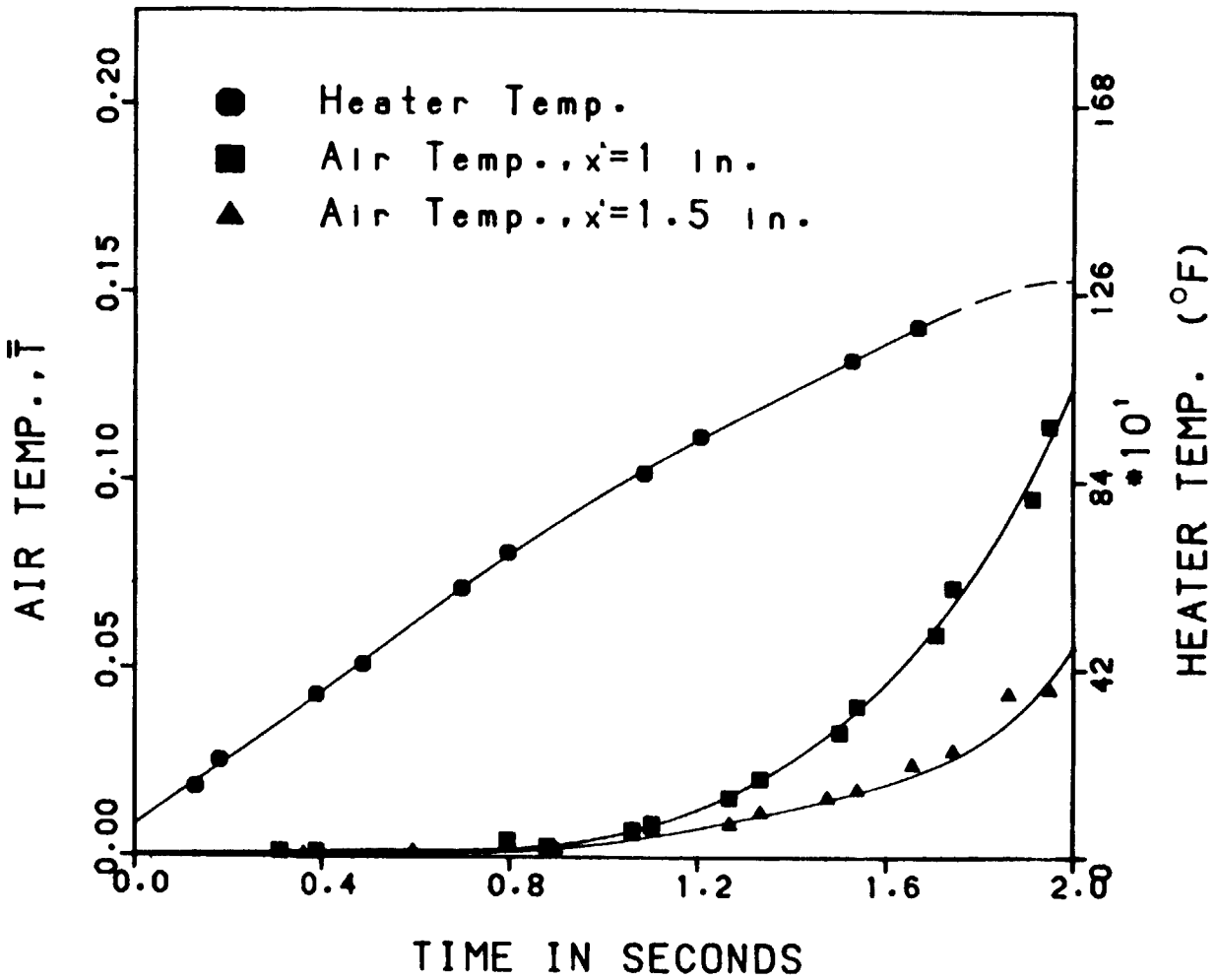

Figure III-13. Variation of Temperature in Zero-Gravity as a Function of Time With V_i'=18 Volts, L'=6 in., T'*= 752 °F, and T_o'=72 °F.

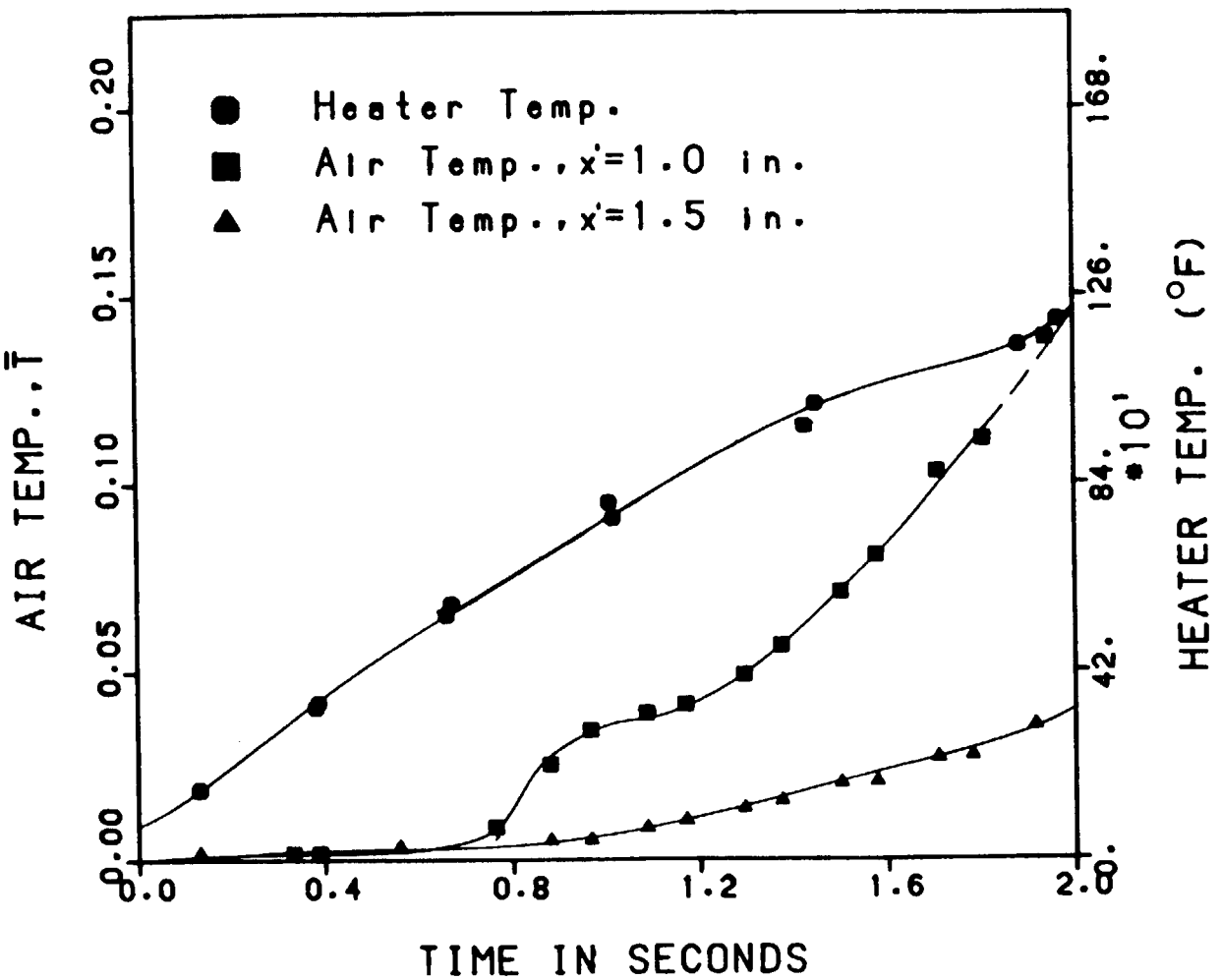

Figure III-14. Variation of Temperture in the Gravity Environment as a Function of Time With V'_i=18 Volts, L'=6 in., T'^*= 664 ° F, and T'_0=77 ° F.

rate of air temperature rise at $\dot{x}$= 0.5 in., Figure III-14 indicates that the rate of air temperature rise at $\dot{x}$= 1.0 in. is not monotonic. It is also important to mention that while the heater temperature shown in Figure III-13 is slightly higher than that of Figure III-14, only the air temperature measured at $\dot{x}$= 1.0 in. in the zero-gravity environment shows lower values than those obtained, at the same location, under gravity conditions.

When the high voltage setting (32 volts) was used, heater temperatures well above 1800 °F were recorded at the end of the heating process. Figures III-15 and III-16 show the extent of the elevated foil temperature reached during these experiments. Figure III-15 represent the temperature data obtained from one run performed in the zero-gravity field at $\dot{x}$= 0, $\dot{x}$= 1 in., and $\dot{x}$= 4 in. . The cylinder height was set at 1 ft. . The results obtained under the same conditions but in the gravity environment are presented in Figure III-16. Both figures show an increase and then a decrease in the rate of air temperature rise measured at the two locations. However, this behavior is more notable in the curves showing the air temperature at $\dot{x}$= 1.0 in. .

Figures III-17 and III-18 show the results of the temperature measurements obtained at $\dot{x}$= 2.0 in. and $\dot{x}$= 3.0 in. using the high voltage setting and the long cylinder case ($\dot{L}$= 1 ft.). The data obtained for the high

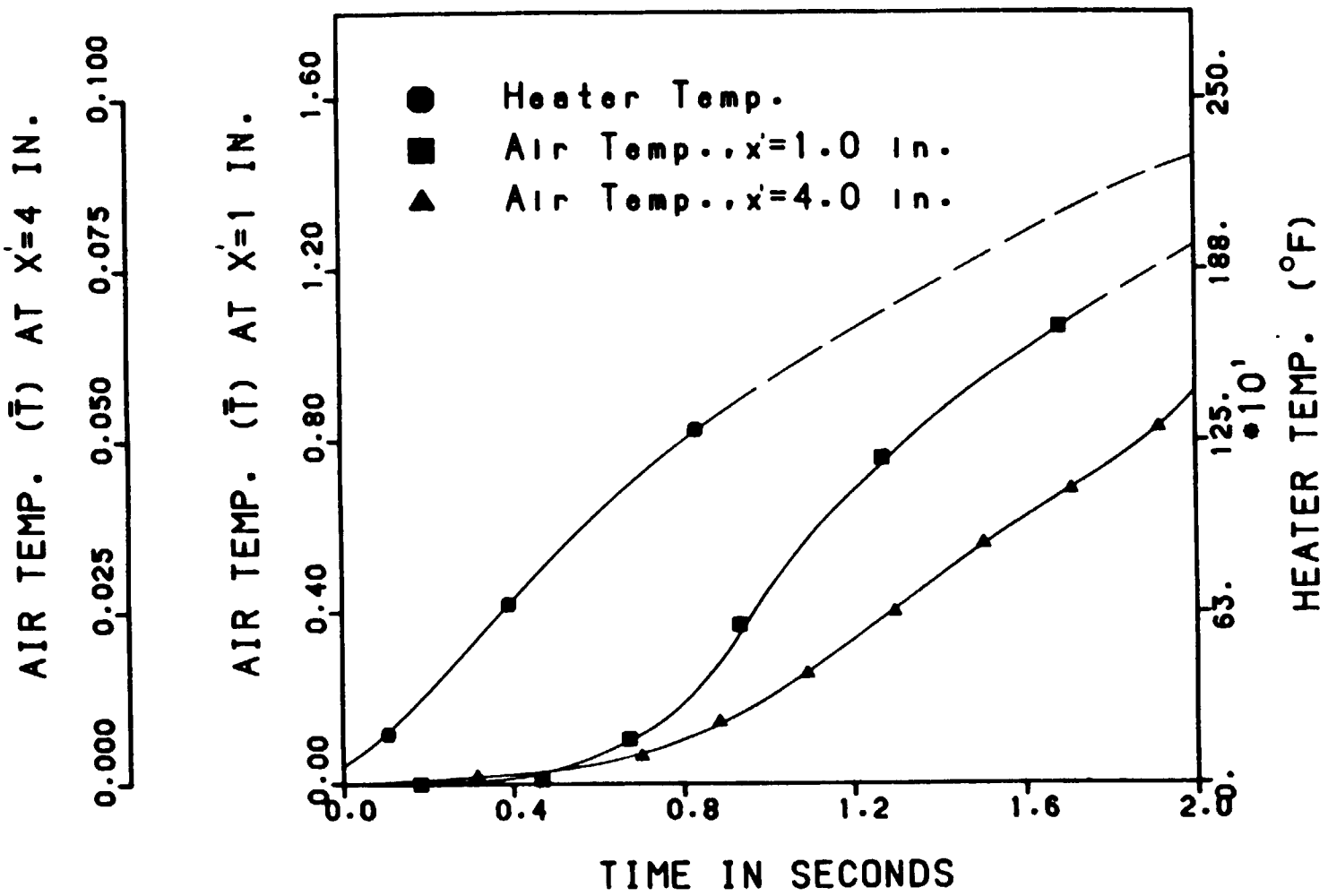

Figure III-15. Variation of Temperature in Zero-Gravity as a Function of Time With V_i'=36 Volts, L'=12 in., T'*= 1069 °F, and T_o'=68 ° F.

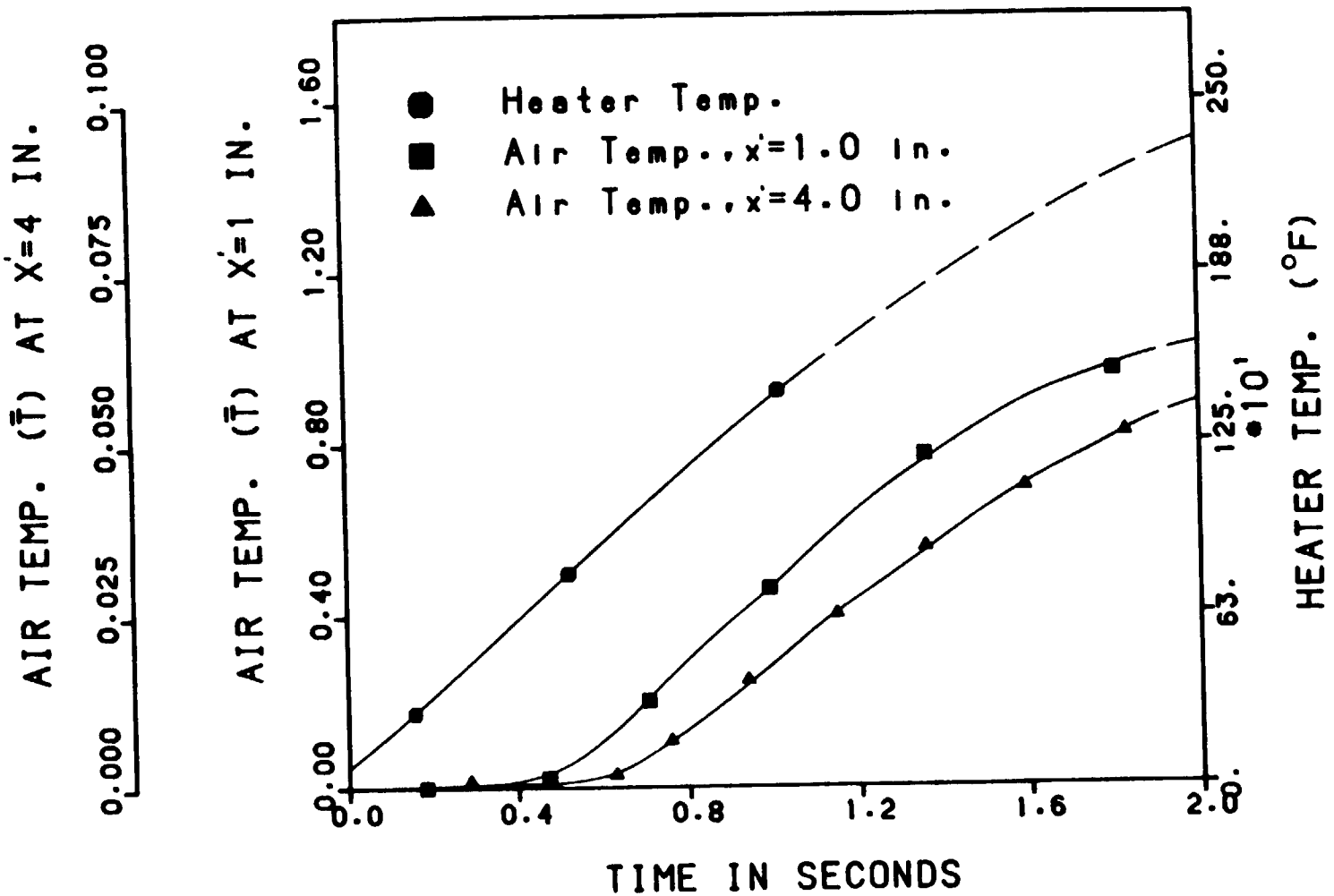

Figure III-16. Variation of Temperture in the Gravity Environment as a Function of Time With V_i'=36 Volts, L'=12 in., T'^*= 1109 °F, and T_o'=76 ° F.

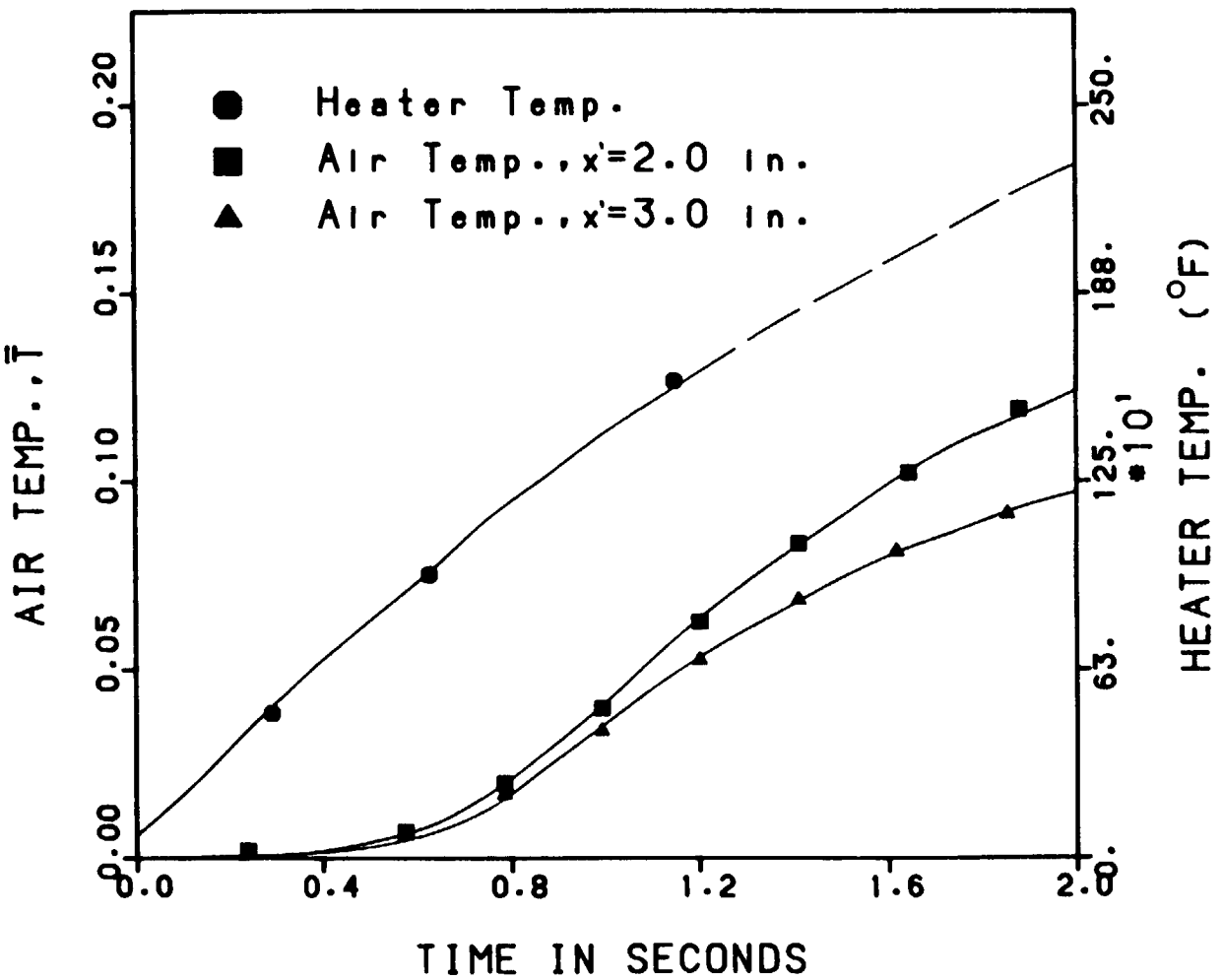

Figure III-17. Variation of Temperature in Zero-Gravity as a Function of Time With V_i'=36 Volts, L=12 in., T'^*= 1083 ° F, and T_0=76 °F.

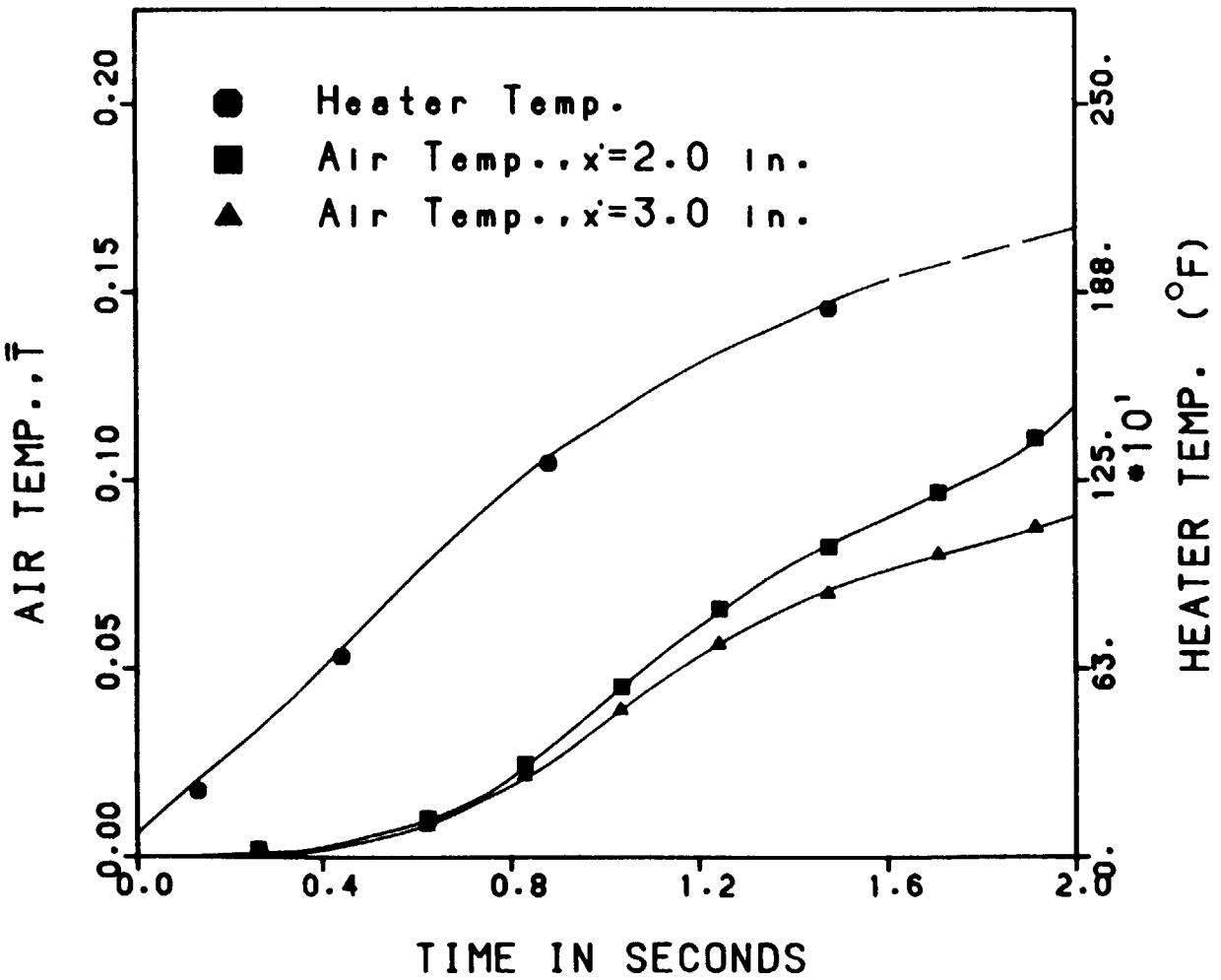

Figure III-18. Variation of Temperture in the Gravity Environment as a Function of Time With V_i'=36 Volts, L'=12 in., T'^*= 1047 °F, and T_o'=76 ° F.

volatge setting and the short cylinder height (0.5 ft.) are presented in Figure III-19. Since the thermometers do not display temperature readings that are above 1844 °F, dash lines are used to indicate that the temperature display limit was exceeded.

The transient air temperature measured during free fall at $\dot{x}$= 1.0 in. and at $\dot{x}$= 1.5 in. is shown in Figures III-20 and III-21. The voltage used and the cylinder height were 32 volts and 0.5 ft. , respectively. The results of the temperature measurements performed on the ground using the same heating rate and cylinder height are plotted in Figures III-22 and III-23. Although the heater temperature shown in Figures III-22 and III-23 are almost identical, the air temperature measured at $\dot{x}$= 1.0 in. and plotted in Figure III-23 show much higher values than those shown in Figure III-22.

An uncertainty analysis for the experimental data was performed and, in the interest of the clarity of presentation, are given in the Appendix F at the end of this report.

The actual temperature data taken during the experiments are reproduced for convenience in the Appendix G.

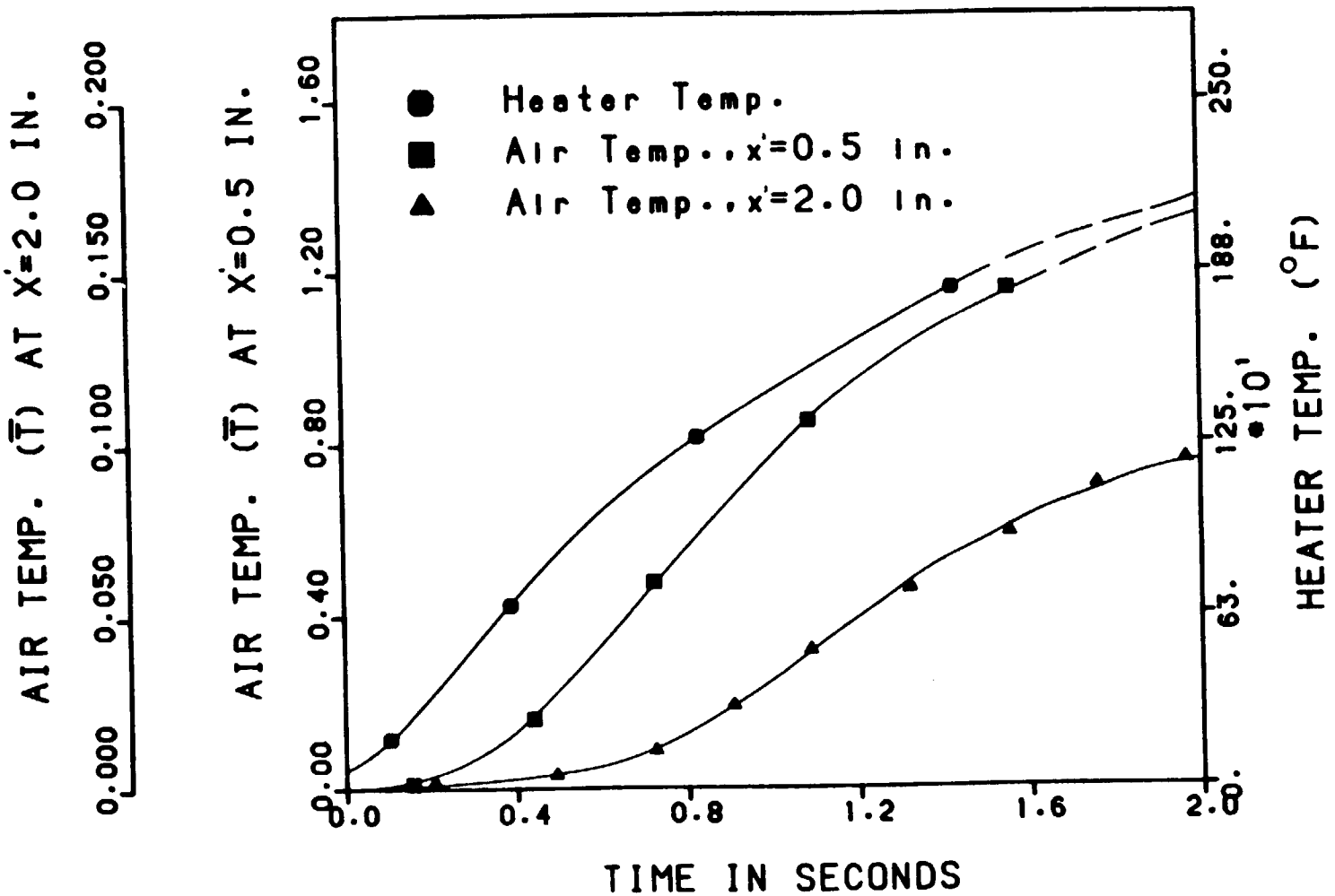

Figure III-19. Variation of Temperature in Zero-Gravity as a Function of Time With V_i'=36 Volts, L'=6 in., T'*= 1068 °F, and T_o'=70 °F.

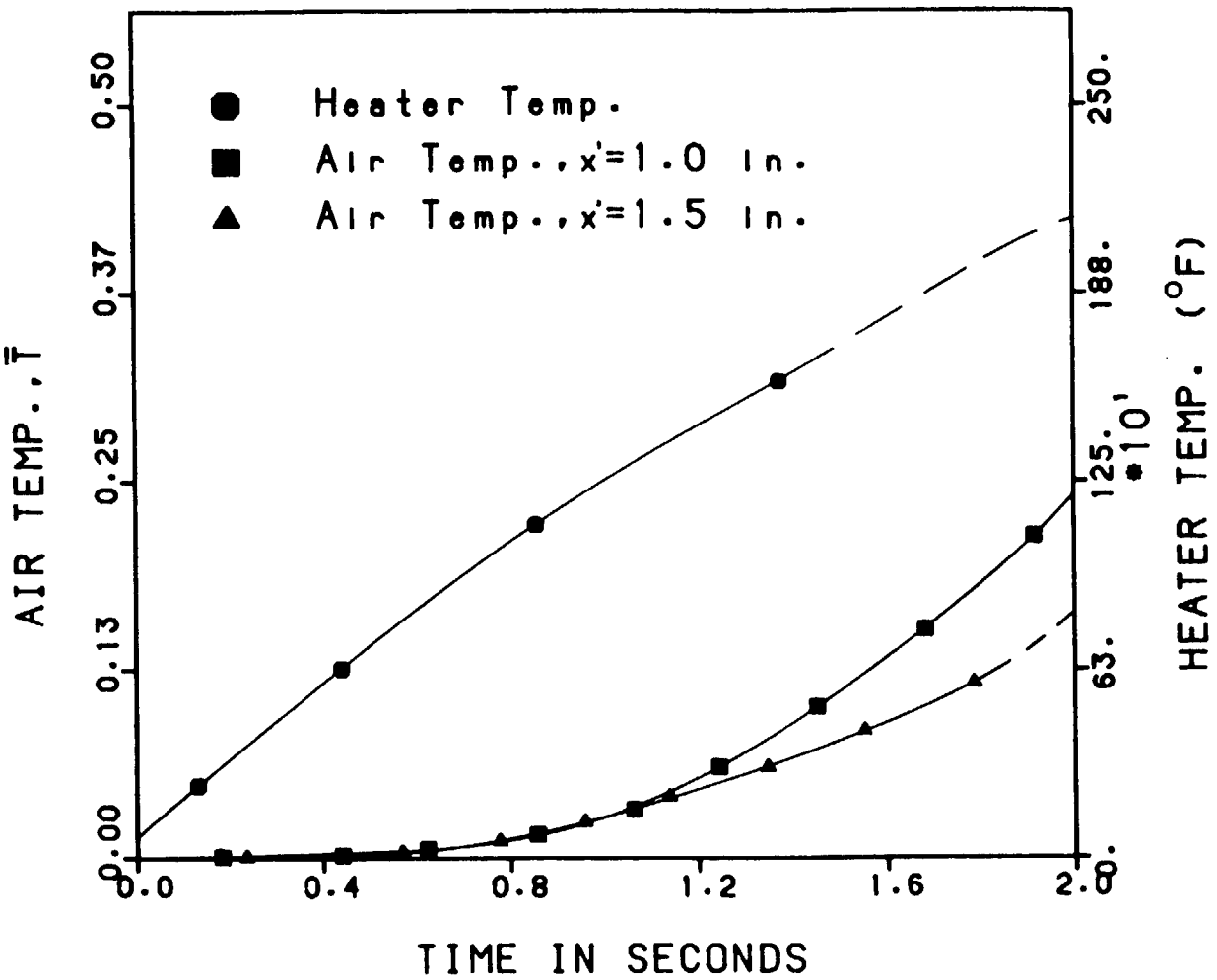

Figure III-20 Variation of Temperature in Zero-Gravity as a Function of Time With V_i'=36 Volts, L=6 in., T'^*= 1026 ° F, and T_o' =76° F.

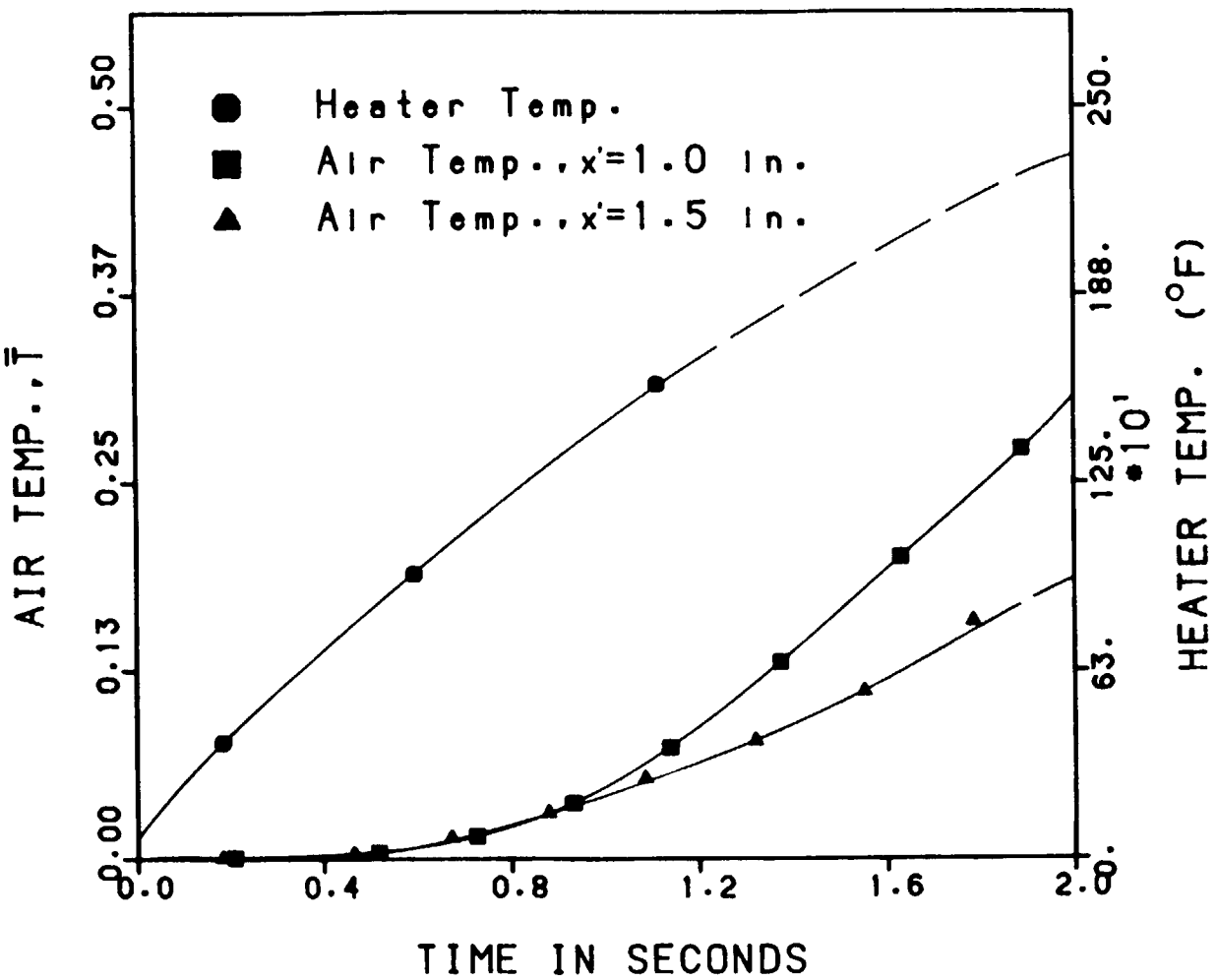

Figure III-21. Variation of Temperature in Zero-Gravity as a Function of Time With V_i'=36 Volts, L'=6 in., T'^*= 1203 ° F, and T_0'=68° F.

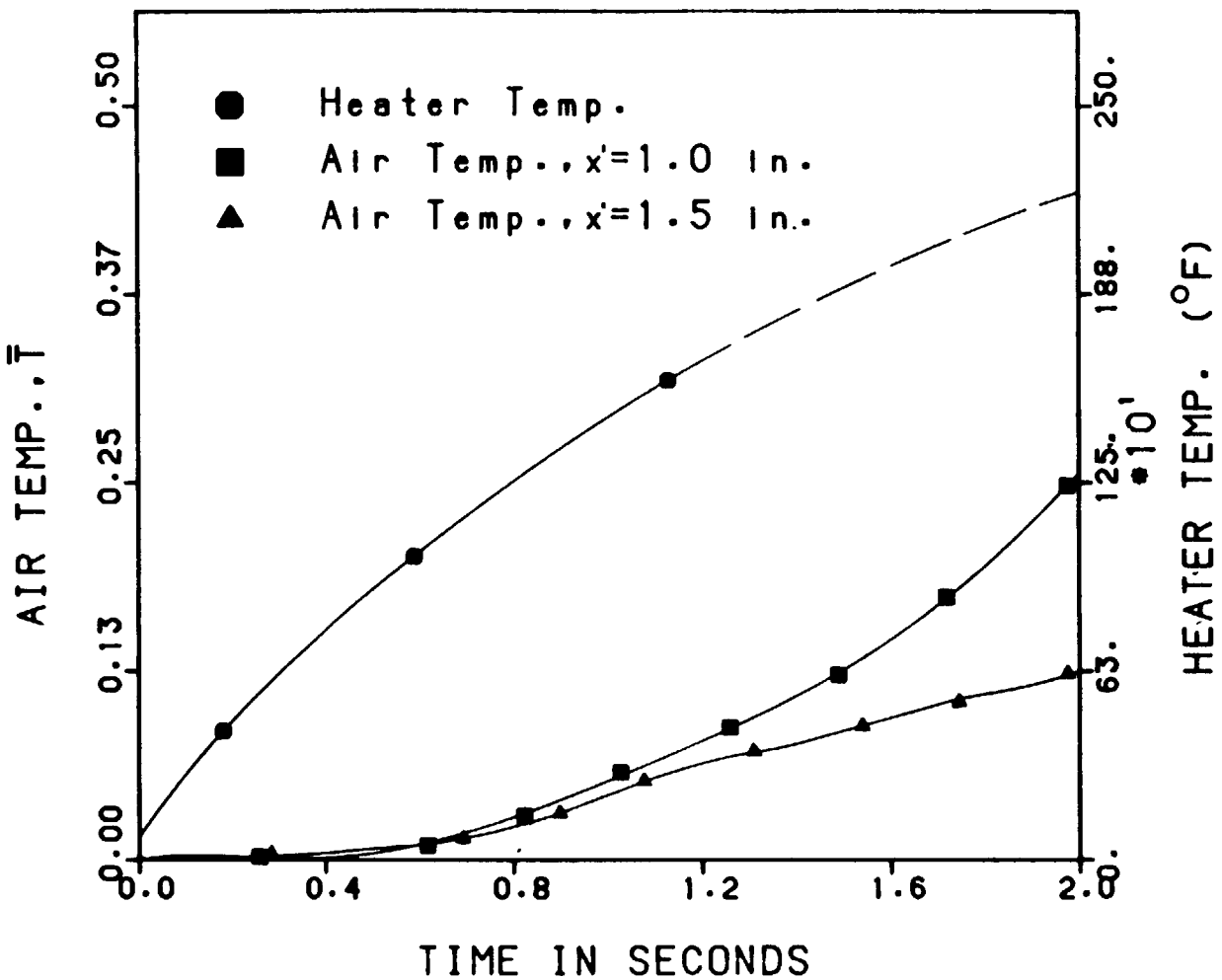

Figure III-22. Variation of Temperture in the Gravity Environment as a Function of Time With V_i'=36 Volts, L'=6 in., T'^*= 1145 ° F, and T_o' =76 ° F.

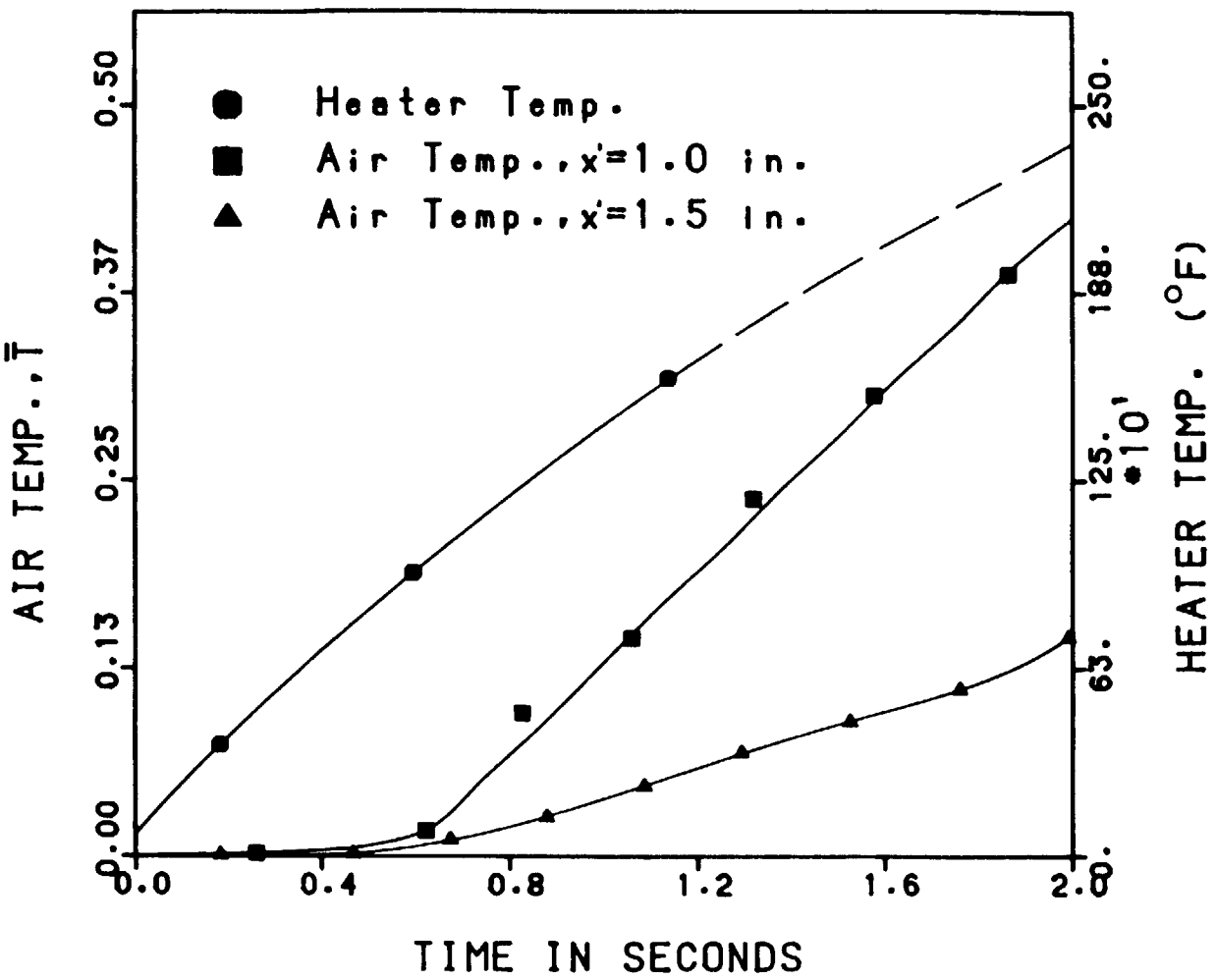

Figure III-23. Variation of Temperture in the Gravity Environment as a Function of Time With V_i'=36 Volts, L'=6 in., T'*= 1145 ° F, and T_o' =76 ° F.

CHAPTER IV

THE ANALYTICAL INVESTIGATION

In the analytical study a theoretical model similar to that of Spradley, Bourgeois, Fan, and Grodzka [20] was developed. Instead of imposing a step change in temperature at the heated surface, the actual transient heater temperature measured during the experiments was used as the temperature boundary condition at $\dot{x}= 0$.

The major tasks accomplished in this part of the study were:

1. the development of a computer program used to obtain polynomial curve fit equations that describe the heater temperature measured during the experiments.

2. employing an implicit finite difference scheme by means of which the transient temperature profiles in the air were determined based on a conduction-only solution using the actual boundary conditions of the experiments. The calculated temperature distribution in the enclosed air were compared to the experimental data to determine the effects of TAC on the rate of heat transfer achieved in the experiments.

3. a computer program was developed to estimate the error in the temperature measurements due to radiation heat transfer absorbed by the thermocouples.

4. the development and application of an explicit

numerical algorithm similar to Spradley et al. to solve the unsteady one-dimensional governing equations for thermoacoustic convection heat transfer problem incorporating the experimental boundary conditions for both gravity and zero-gravity environments.

The Pure Conduction Solution

The solution of the conduction heat transfer problem described by the one-dimensional time-dependent heat conduction equation was obtained using finite difference approximations. The air specific heat (C'_p) was assumed constant since it is relatively not a strong function of temperature. The air density (ρ') and thermal conductivity (k') were allowed to vary with temperature during the calculations. A schematic diagram of the geometry of the problem is shown in Figure IV-1. The governing equations of the conduction heat transfer problem is given by

$$\frac{\partial}{\partial x'}\left(k'(T')\frac{\partial T'}{\partial x'}\right)=\rho'(T')C'_p\frac{\partial T'}{\partial t'} \qquad (4.1)$$

The boundary and initial conditions are:

$T'(x'=0,t')=f(t')$ Heated Wall (4.2)

$T'(x'=L',t')=T'_o$ Isothermal Wall (4.3)

$T'(x',t'=0)=T'_o$ Initial Isothermal Condition (4.4)

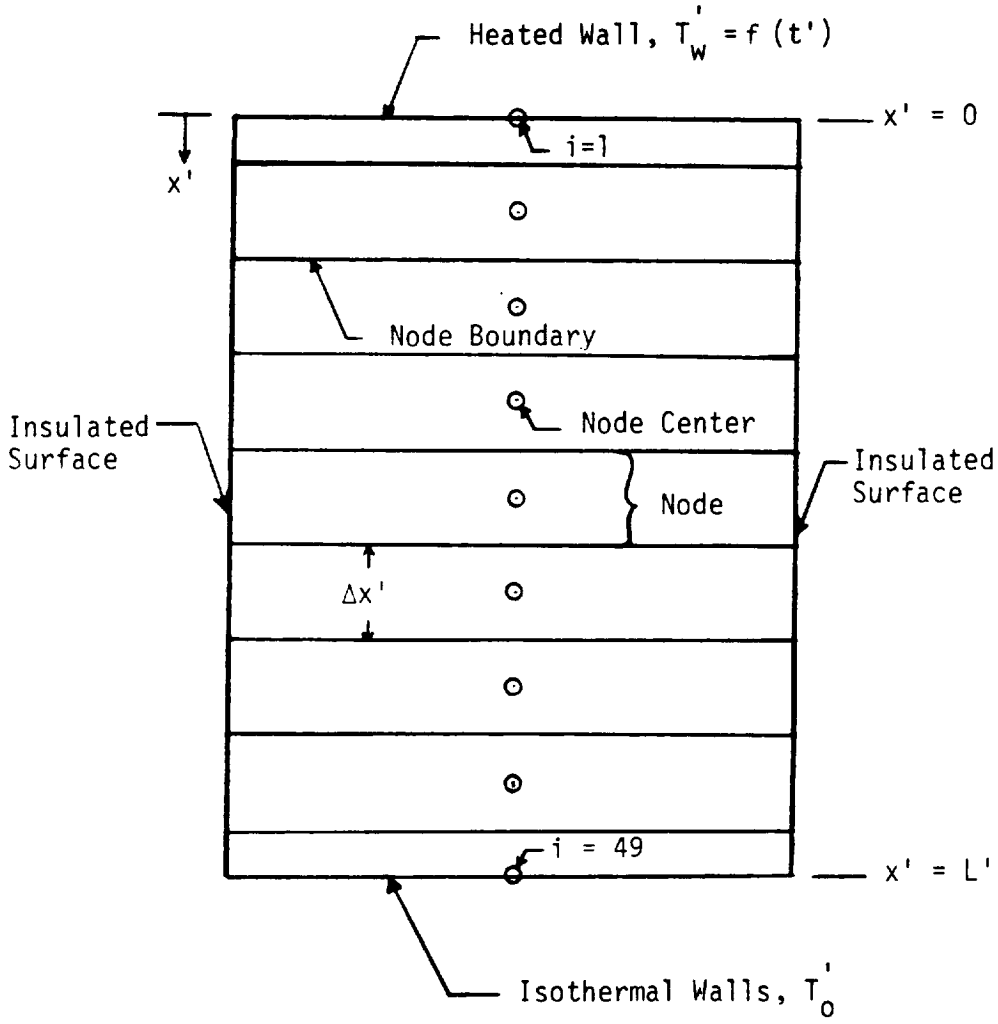

Figure IV-1. Nodal System Used in the Conduction-Only Numerical Heat Transfer Model.

The transient heater temperature was approximated using the following curve fit polynomial.

$$f(t') = a\,t'^{6} + b\,t'^{5} + c\,t'^{4} + d\,t'^{3} + e\,t'^{2} + g\,t + h$$

The coefficients of the curve fit equation (a,b,c,d,e,and g) were calculated using the transient heater temperature data recorded during the experimental runs. The least square method was used to derive the equations relating the experimental data and the curve fit coefficients. These equations were then solved using a computer program developed to calculate the curve fit coefficients.

As shown in Figure IV-1, a grid with 49 node points was employed. The grid spacing is designated by $\Delta x'$ and the first node center is located at the surface subject to heating. A set of linear algebraic equations describing the transient air temperature field were derived. The followings present a detail derivation of these equations:

An energy balance performed on a node i yields:

$$K'_{i-\frac{1}{2}} \frac{A'}{\Delta x'} (T'_{i-1} - T'_{i})^{n+\frac{1}{2}} - K'_{i+\frac{1}{2}} \frac{A'}{\Delta x'} (T'_{i} - T'_{i+1})^{n+\frac{1}{2}} = \rho'^{n}_{i} A' \Delta x' \frac{\partial T'}{\partial t} \Big|_{i}^{n+\frac{1}{2}} \quad (4.5)$$

where

$$K^n_{i-\frac{1}{2}} = \frac{K^n_i + K^n_{i-1}}{2} \tag{4.6}$$

and

$$K^n_{i+\frac{1}{2}} = \frac{K^n_i + K^n_{i+1}}{2} \tag{4.7}$$

In order to avoid iteration methods, the values of the air thermal conductivity and density evaluated based on the previous temperature profile were used to update the temperature distribution.

substituting

$$\left.\frac{\partial T'}{\partial t'}\right|^{n+\frac{1}{2}}_i \simeq \frac{T'^{n+1}_i - T'^{n}_i}{\Delta t'}$$

$$(T'_{i-1} - T'_i)^{n+\frac{1}{2}} \simeq \tfrac{1}{2}\left[(T'_{i-1} - T'_i)^n + (T'_{i-1} - T'_i)^{n+1}\right]$$

$$(T'_i - T'_{i+1})^{n+\frac{1}{2}} \simeq \tfrac{1}{2}\left[(T'_i - T'_{i+1})^n + (T'_i - T'_{i+1})^{n+1}\right]$$

equation (4.5) becomes:

$$\left(\frac{2\rho'_i C'_p}{\Delta t'} + \frac{K'_{i-\frac{1}{2}} + K'_{i+\frac{1}{2}}}{\Delta x'^2}\right)T^{n+1}_i - \frac{K'_{i-\frac{1}{2}}}{\Delta x'^2}T^{n+1}_i - \frac{K'_{i+\frac{1}{2}}}{\Delta x'^2}T'^{n+1}_{i+1} =$$

$$\left(\frac{2\rho'_i C'_p}{\Delta t'} - \frac{K'_{i-\frac{1}{2}} + K'_{i+\frac{1}{2}}}{\Delta x'^2}\right)T'^{n}_i + \frac{K'_{i-\frac{1}{2}}}{\Delta x'^2}T^n_{i-1} + \frac{K'_{i+\frac{1}{2}}}{\Delta x'^2}T'^{n}_{i+1} \tag{4.8}$$

Let

$$B_i = \frac{K'_{i-\frac{1}{2}}}{\Delta x'^2} \tag{4.9}$$

$$C_i = \frac{K'_{i+\frac{1}{2}}}{\Delta x'^2} \tag{4.10}$$

$$D'_i = \rho_i C_p / \Delta t' \tag{4.11}$$

$$A'_i = 2D'_i + B'_i + C'_i \tag{4.12}$$

$$E'_i = 2D'_i - B'_i - C'_i \tag{4.13}$$

substituting equations (4.9) to (4.13) into (4.8) give

$$A'_i T'^{,n+1}_i - B'_i T'^{,n+1}_{i-1} - C'_i T'^{,n+1}_{i+1} = E'_i T'^{,n}_i + B'_i T'^{,n}_{i-1} + C'_i T'^{,n}_{i+1} \tag{4.14}$$

Equation (4.14) represents a set of algebraic equations forming a tri-diagonal matrix. These linear equations can now be easily solved to calculate the unsteady temperature distribution in the air at a new time level (n+1).

Let

$$T'^{,n+1}_i = \alpha_i + \beta_i T'^{,n+1}_{i+1} \tag{4.15}$$

and

$$T'^{,n+1}_{i-1} = \alpha_{i-1} + \beta_i T'^{,n+1}_i \tag{4.16}$$

where α_i , β_i , α_{i-1} ,and β_{i-1} are intermediate variables.

The substitution of equation (4.16) into equation (4.14) yields

$$A_i' T_i'^{n+1} - B_i'(\alpha_i + \beta_{i-1} T_i'^{n+1}) - C_i' T_{i+1}'^{n+1} = E_i' T_i'^{n} + B_i' T_{i-1}^{n} + C_i' T_{i+1}'^{n} \qquad (4.17)$$

comparing the above equation to equation (4.15) implies

$$\alpha_i = \frac{E_i' T_i'^{n} + B_i' T_{i-1}'^{n} + C_i' T_{i+1}'^{n} + \alpha_{i-1}\beta_i}{A_i - \beta_{i-1} B_i} \qquad (4.18)$$

and

$$\beta_i = \frac{C_i'}{A_i' - \beta_{i-1} B_i} \qquad (4.19)$$

The boundary condition at $x'=0$ is now introduced by writing equation (4.14) for i=2

$$A_2' T_2'^{n+1} - B_2' T_1'^{n+1} - C_2' T_3'^{n+1} = E_2' T_2'^{n} + B_2' T_1'^{n} + C_2' T_3'^{n} \qquad (4.20)$$

comparing equation (4.20) to equation (4.15) results in

$$\alpha_2 = \frac{E_2' T_2'^{n} + C_2' T_3'^{n} + B_2'(T_1'^{n} + T_1^{n+1})}{A_2'} \qquad (4.21)$$

and

$$\beta_2 = \frac{C_2'}{A_2'} \qquad (4.22)$$

The solution to the transient air temperature field at n+1 was obtained according to the following computational steps:

1. the variable thermal properties of air, $K'(T')$ and $\rho'(T')$, were calculated using the known temperature distribution at time level n. Curve fit equations relating the air density and conductivity to the air temperature were used to determine these properties. The coefficients of the curve fit polynomials were obtained using a curve fit computer program and the appropriate data from Reference [22].

2. α_2 and β_2 were determined by first calculating A_2, B_2, C_2, and D_2 and then substituting these values into equation (4.23) and (4.24).

3. equations (4.18) and (4.19) were solved to calculate α_i, and β_i for i=3 to 48.

4. the air temperature at time level n+1 was calculated by solving equation (4.15) starting with i=49 and working backward until i=3. Notice that the boundary condition at $x'=L'$ would be introduced when solving for $T'_{i,j}$.

A computer program (Appendix C) was developed to solve the set of the tri-diagonal equations given by equation (4.14). The results obtained are discussed in the next chapter.

Estimation Of The Effects Of Radiation Heat Transfer On The Temperature Measurements

Due to the high heater surface temperatures achieved during the two seconds heating process and the small diameter of the thermocouple used in the experiments, it is expected that the radiation emitted by the stainless steel foil produces significant effects on the thermocouple output. A preliminary estimation of such effects showed that the radiation heat transfer to the thermocouple located at x'=1.0 in. causes a temperature rise of approximately 14 ^{o}F $\pm$ 6 ^{o}F when the low voltage setting (16 volts) is employed. Since the radiation effects are appreciable, a more accurate analysis of the radiation problem was performed by developing a computer program to calculate the transient temperature rise of the thermocouple caused solely by radiation heat transfer. The following assumptions were utilized in deriving the governing equations:

1. The radiation emitted by the side wall and the bottom surface of the cylinder are negligible.

2. The radiation reflected at the bottom surface has small effects on the measured temperature.

3. The absorptivity of the thermocouple is 1.0.

4. The configuration factor $F_{1\to3}$ was calculated assuming the steel foil covers the entire area of the top surface of the cylinder.

5. Negligible absorption and scattering of the air medium.

Assumptions 3 and 4 were employed to ascertain the maximum possible contribution of radiation to the measured values of temperature in the experiments. A schematic diagram of the geometry of the problem is shown in Figure IV-2.

The rate of radiation heat transfer emitted from the stainless steel foil during a short time interval $\Delta t'$ is given by:

$$q_e = \varepsilon_s(T'_{av})\,\sigma\,A'_s\,T'^{4}_{av}(t) \qquad (4.23)$$

where

$$T'_{av} = \frac{T'^{n+1}_w - T'^{n}_w}{2}$$

T'^{n+1}_w and T'^{n}_w represent the foil temperatures at the end and at the begining of the time interval, respectively.

The emissivity of stainless steel , ε_s , was assumed a function of temperature of the heating surface in the calculations. A polynomial curve fit of order six relating the stainless steel emissivity to temperature was used in this analysis. The polynomial coefficients were calculated utilizing the curve-fit computer program

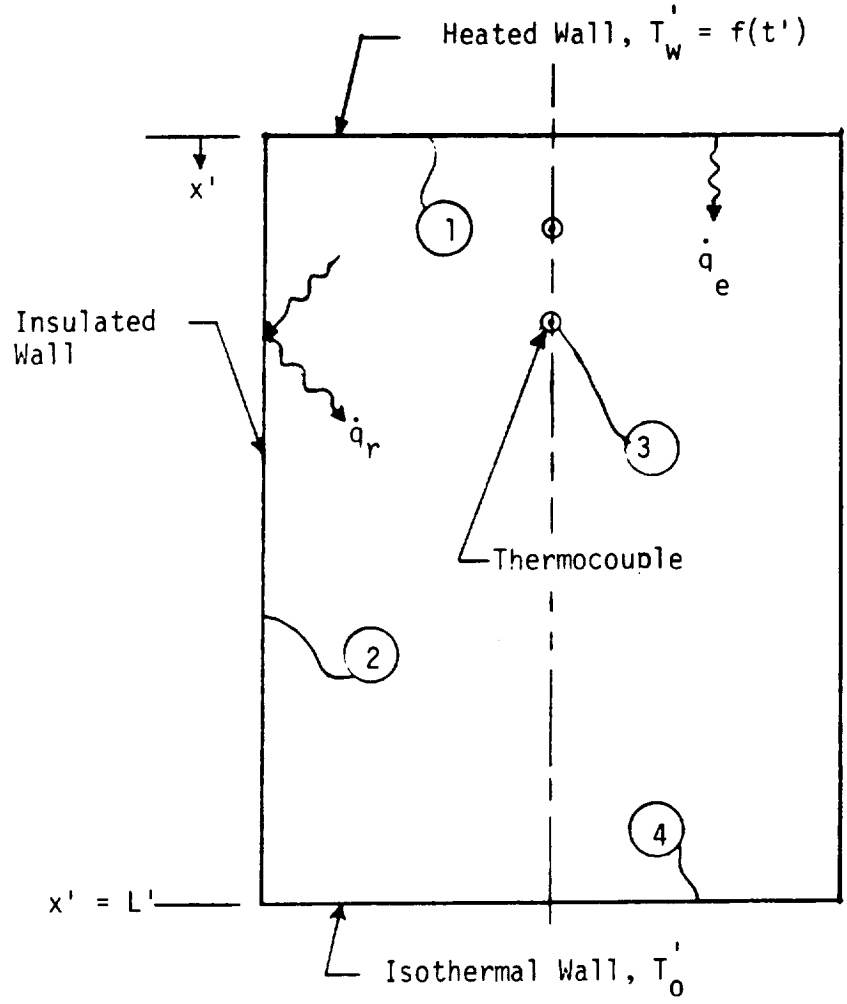

Figure IV-2. Configuration Used in the Radiation-Only Numerical Heat Transfer Model.

and emissvity-temperature data obtained from Reference [23]. Due to the small diameter of the thermocouples, a small change in the emissivity could result in a significant change in the thermocouple temperature rise. Therefore, to insure that the emissivity-temperature data used to obtain the curve fit polynomial is sufficiently accurate, another radiation property Reference, [24], was consulted to add confidence in the reliability of the data. The data listed in this reference agreed with those in Reference [23]. The emissivity curve fit polynomial used is given by the following equation:

$$\varepsilon_s(T'_{av}) = A'_1 T'^{,6}_{av} + A'_2 T'^{,5}_{av} + A'_3 T'^{,4}_{av} + A'_4 T'^{,3}_{av} + A'_5 T'^{,2}_{av} + A'_6 T'_{av} + A'_7$$

where

$$A'_1 = 0.129 \times 10^{-25} (°F)^{-6}$$

$$A'_2 = 0.106 \times 10^{-15} (°F)^{-5}$$

$$A'_3 = 0.181 \times 10^{-12} (°F)^{-4}$$

$$A'_4 = 0.164 \times 10^{-9} (°F)^{-3}$$

$$A'_5 = 0.479 \times 10^{-6} (°F)^{-2}$$

$$A'_6 = 0.152 \times 10^{-3} (°F)^{-1}$$

$$A'_7 = 0.21$$

The rate of direct incident radiation striking the thermocouple surface is

$$q_d'(t') = \varepsilon_s \sigma' F_{2\to3} A_s' T_{av}'^4 \qquad (4.24)$$

where

$F_{i\to j}$ is the configuration factor between the heater and the thermocouple.

The rate of reflected radiation incident on the thermocouple is given by:

$$q_r'(t') = R_i \sigma' F_{1\to2} F_{2\to3} A_s' T_{av}'^4 \qquad (4.25)$$

where R is the reflectivity of the insulating material.

Assuming the thermocouple absorbs 100 percent of the incoming radiation, the rate of absorbed radiation becomes

$$q_a'(t') = (F_{1\to3} + F_{1\to2} F_{2\to3} R_i')(\varepsilon_s \sigma' A_s') T_{av}'^4 \qquad (4.26)$$

The configuation factors $F_{1\to3}$, $F_{1\to2}$, and $F_{2\to3}$ were evaluated using the following equations obtained from Reference [25].

$$F_{3\to1} = \tfrac{1}{2}\left(1 - \frac{1}{\sqrt{1 + \left(\frac{R_d'}{h_1'}\right)^2}}\right) \qquad (4.27)$$

$$F_{3\to4} = \tfrac{1}{2}\left(1 - \frac{1}{\sqrt{1+\left(\frac{R_d'}{h_2'}\right)^2}}\right) \qquad (4.28)$$

where R_d' is the radius of the cylinder, h_1' is the distance between the top disk and the thermocouple, and h_2' is the distance between the bottom disk and the thermocouple.

$F_{3\to2}$ can now be evaluated using the equation

$$F_{3\to1} + F_{3\to4} + F_{3\to2} = 1.0$$

$F_{1\to3}$ and $F_{2\to3}$ were calculated by utilizing the reciprocity relationship:

$$A_a F_{a\to b} = A_b F_{b\to a}$$

The configuration factor $F_{1\to2}$ was determined by solving the following equations:

$$F_{1\to2} + F_{1\to4} = 1.0$$

$$F_{1\to4} = \tfrac{1}{2}\left(x' - \sqrt{x'^2 - 4\left(\frac{R_2'}{R_1'}\right)^2}\right)$$

where

$$R_1' = \frac{R_d'}{L'}, \quad R_2' = \frac{R_d'}{L'}, \quad x' = 1 + \frac{1 + R_2'^2}{R_1'^2}$$

The rate of radiation emitted by the thermocouple during the time interval $\Delta t'$ is given by

$$q'_{e_t}(t') = \sigma' A'_t T'^{4}_t (t') \tag{4.29}$$

Therefore, the rate of heat gain becomes:

$$q'_g(t') = q'_a(t') - q'_{e_t}(t')$$

Assuming negligible heat loss from the thermocouple, then

$$q'_g(t') = \rho'_t V'_t C'_{p_t} \Delta T'_t(t')$$

where the density (ρ'_t) and the specific heat (C'_{p_t}) of the thermocouple at the junction are the average density and average specific heat of chromel and constantan, respectively.

therefore,

$$\Delta t'_t(t) = \frac{q'_g(t')}{\rho'_t V'_t C'_{p_t}} \tag{4.30}$$

The above equations were solved for the two thermocouple locations employed in the experiments using the computer program listed in the Appendix D. A time increment of 0.05 seconds was used in the calculations. The geometrical data and the material properties used in this analysis are shown in Table IV-1.

Table IV-1. Geometrical Characteristics and Material Properties Used in the Computation of the Effects of Radiation Heat Transfer on Thermocouple Output.

Property	Value
C'_{p_t}	0.1 Btu / lbm°F
ρ'_t	551 lbm/ft^3
R_t	0.80
σ	1.714×10^{-9} Btu / hr ft^2 °R^4
D'_t	0.01 in.
R'_d	6 in.
A'_s	66 in^2
$\Delta t'$	0.05 sec.

The TAC Heat Transfer Numerical Model

The non-dimensional conservation equations derived in chapter II were solved employing an explicit finite difference algorithm. The transient velocity, density, pressure, and temperature profiles for an air medium were determined using the actual heater surface temperature measured in the experiments as the temperature boundary condition at the heated surface. The results obtained for both gravity and zero-gravity environments are compared to the results of the conduction-only solution in the following chapter.

The governing non-dimensional equations describing this TAC model are:

Continuity:

$$\frac{\partial \rho}{\partial t} + \frac{\partial}{\partial x}(\rho u) = 0 \qquad (2.12)$$

Newton's Second Law:

$$\frac{\partial}{\partial t}(\rho u) + \frac{\partial}{\partial x}(\rho u u) = -\frac{\partial P}{\partial x} + a\,\frac{L'g'}{R'T_o'}\,\rho + \frac{4}{3}\left(\frac{1}{Re}\right)\frac{\partial^2 u}{\partial x^2} \qquad (4.31)$$

Energy:

$$\rho\frac{\partial T}{\partial t} + \rho u\frac{\partial T}{\partial x} = -(\gamma - 1)P\frac{\partial u}{\partial x} + \left(\frac{\gamma}{Re\,Pr}\right)\frac{\partial^2 t}{\partial x^2} \qquad (2.14)$$

State:

$$P = \rho T \tag{2.15}$$

where

$$a = \begin{cases} 1 & \text{Gravity Environment} \\ 0 & \text{Zero-Gravity Environment} \end{cases}$$

The dimensionless initial and boundary conditions are:

$$U(x,t=0)=0 \ , \quad T(x,t=0)=1 \ , \quad \rho(x,t=0)=1 \tag{2.16}$$

$$U(x=0,t)=U(x=1,t)=0 \tag{2.17}$$

$$T(x=0,t)= f(t')/T_o' \tag{4.32}$$

$$T(x=1,t)=1 \tag{2.19}$$

Where $f(t')$ represents the dimensional transient heater temperature of the foil obtained in the experiments.

The finite difference formulation used by Spradley, et al. to solve the conservation equations was closely followed in this analysis. The approximate equations representing the various derivative terms that appear in equations (2.12) to (2.14) are shown in Tables IV-2, IV-3, IV-4. Except for the $\left.\frac{\partial^2 T}{\partial x^2}\right|_1^n$ and $\left.\frac{\partial^2 T}{\partial x^2}\right|_k^n$ terms, the equations listed in the above tables are the same as those used by Spradley, et al. in the solution of the infinite parallel plate TAC heat transfer problem. For

Table IV-2. Newton's Second Law in Finite Difference Form

Newton's 2nd Law:

$$\frac{\partial}{\partial t}(\rho u) + \frac{\partial}{\partial x}(\rho u u) = -\frac{\partial P}{\partial x} + a\frac{L'g'}{RT_o'}\rho + \frac{4}{3}\left(\frac{1}{Re}\right)\frac{\partial^2 u}{\partial x^2}$$

Finite Difference Equations:

$$(\rho u)_i^{n+1} = (\rho u)_i^n - \Delta t\left[\delta_x(\rho u u)_i^n + \delta_x(P_i^n) - a\frac{L'g'}{RT_o}(\rho_i^n) - \frac{4}{3}\frac{1}{Re}\delta_x^2(u_i^n)\right]$$

$$\delta_x(\rho u u)_i^n = \frac{(\rho u)_{i+1}^n u_{i+1}^n - (\rho u)_i^n u_i^n}{\Delta x} \qquad \text{for } u_i^n < 0$$

$$\delta_x(\rho u u)_i^n = \frac{(\rho u)_i^n u_i^n - (\rho u)_{i-1}^n u_{i-1}^n}{\Delta x} \qquad \text{for } u_i^n \geq 0$$

$$\delta_x(\rho u u)_1^n = \frac{(\rho u)_1^n u_1^n - (\rho u)_2^n u_2^n}{2\Delta x}$$

$$\delta_x(\rho u u)_k^n = -\frac{(\rho u)_k^n u_k^n - (\rho u)_{k-1}^n u_{k-1}^n}{2\Delta x}$$

$$\delta_x(P)_1^n = \frac{P_2 - P_1}{\Delta x}$$

$$\delta_x(P_i^n) = \frac{P_{i+1}^n - P_{i-1}^n}{2\Delta x}$$

$$\delta_x(P_k)^n = \frac{P_k - P_{k-1}}{\Delta x}$$

$$\delta_x^2(u_i^n) = \frac{u_{i+1}^n - 2u_i^n + u_{i-1}^n}{\Delta x^2}$$

$$\delta_x^2(u_1^n) = \frac{u_2^n - 3u_1^n}{\Delta x^2}$$

$$\delta_x^2(u)_k^n = \frac{u_{k-1}^n - 3u_k^n}{\Delta x^2}$$

Table IV-3. Continuity Equation in Finite Difference Form

Continuity Equation:

$$\frac{\partial}{\partial t}\rho = -\frac{\partial}{\partial t}(\rho u)$$

Finite Difference Equations:

$$\rho_i^{n+1} = \rho_i^n - \Delta t\left[\delta_x(\rho u)_i^{n+1}\right]$$

$$\delta_x(\rho u)_i^{n+1} = \frac{(\rho u)_{i+1}^{n+1} - (\rho u)_{i-1}^{n+1}}{2\Delta x}$$

$$\delta_x(\rho u)_1^{n+1} = \frac{(\rho u_1^{n+1}) + (\rho u_2^{n+1})}{2\Delta x}$$

$$\delta_x(\rho u)_k^n = -\frac{(\rho u)_k^{n+1} + (\rho u)_{k-1}^{n+1}}{2\Delta x}$$

$$u_i^{n+1} = \frac{\rho u_i^{n+1}}{\rho_i^{n+1}}$$

Table IV-4. Energy Equation in Finite Difference Form

Energy Equation:

$$\frac{\partial T}{\partial t} + u\frac{\partial T}{\partial x} = -\frac{(\gamma-1)}{\rho} P \frac{du}{dx} + \frac{\gamma}{\rho}\left(\frac{1}{Re\,Pr}\right)\frac{d^2T}{dx^2}$$

Finite Difference Equations:

$$T_i^{n+1} = T_i^n - \Delta t\left[u_i^{n+1}\delta_x(T_i^n) + \frac{\gamma-1}{\rho_i^{n+1}} P_i^n \delta_x(u_i^{n+1}) - \frac{\gamma}{\rho_i^{n+1}}\left(\frac{1}{Re\,Pr}\right)\delta_x^2(T_i^n)\right]$$

$$\delta_x(u_i^{n+1}) = \frac{u_{i+1}^{n+1} - u_{i-1}^{n+1}}{2\Delta x}$$

$$\delta_x(u)_1^{n+1} = \frac{u_1^{n+1} + u_2^{n+1}}{2\Delta x} \qquad \delta_x(u)_k^{n+1} = -\frac{u_k^{n+1} + u_{k-1}^{n+1}}{2\Delta x}$$

$$\delta_x(T_i^n) = \begin{cases} (T_{i+1}^n - T_i^n)/\Delta x & u_i^n < 0 \\ (T_i^n - T_{i-1}^n)/\Delta x & u_i^n \geq 0 \end{cases}$$

$$\delta_x(T_1^n) = \begin{cases} (T_2 - T_1)/\Delta x & u_1^n < 0 \\ (T_1 - T_w)/(0.5\,\Delta x) & u_1^n \geq 0 \end{cases}$$

$$\delta_x(T_k^n) = \begin{cases} (T_k^n - T_{k-1}^n)/\Delta x & u_k^n \geq 0 \\ (T_o^n - T_k^n)/(0.5\,\Delta x) & u_k^n < 0 \end{cases}$$

$$\delta_x^2(T_i^n) = \frac{T_{i+1}^n - 2T_i^n + T_{i-1}^n}{\Delta x^2}$$

$$\delta_x^2(T_1)^n = \frac{4}{3}\left(\frac{T_2 - 3T_1^n + 2T_w^n}{\Delta x^2}\right)$$

$$\delta_x^2(T_k^n) = \frac{4}{3}\left(\frac{T_{k-1}^n - 3T_k^n + 2}{\Delta x^2}\right)$$

i=1 and i=k, the first and last node centers (see Figure IV-3), Spradley et al. used equations (4.33) and (4.34) to evaluate the second spatial derivative of temperature. However, a derivation of the approximate equations showed that the correct form of these equations would be as listed in Table IV-4.

$$\left.\frac{\partial^2 T}{\partial x^2}\right|_1^n = \frac{T_2^n - 3T_1^n + 2(T_w'/T_o')}{\Delta x^2} \qquad (4.33)$$

$$\left.\frac{\partial^2 T}{\partial x^2}\right|_k^n = \frac{T_{k-1}^n - 3T_k^n + 2}{\Delta x^2} \qquad (4.34)$$

The computer program used to solve the finite difference equations is listed in the Appendix E. A time step increament of $\Delta t = 0.015$ units and a grid spacing of $\Delta x = 0.0455$ were employed in the calculations. The equation representing Newtons Second Law was treated first to calculate (ρu_i^{n+1}). The spatial first derivative of (ρu_i^{n+1}) was then evaluated and substituted in the continuity equation to determine the new density profile. The air velocity at all node centers were then calculated at the new time level and substituted in the energy equation to compute T_i^{n+1}. Finally, the new pressure distribution was determined using the equation of state.

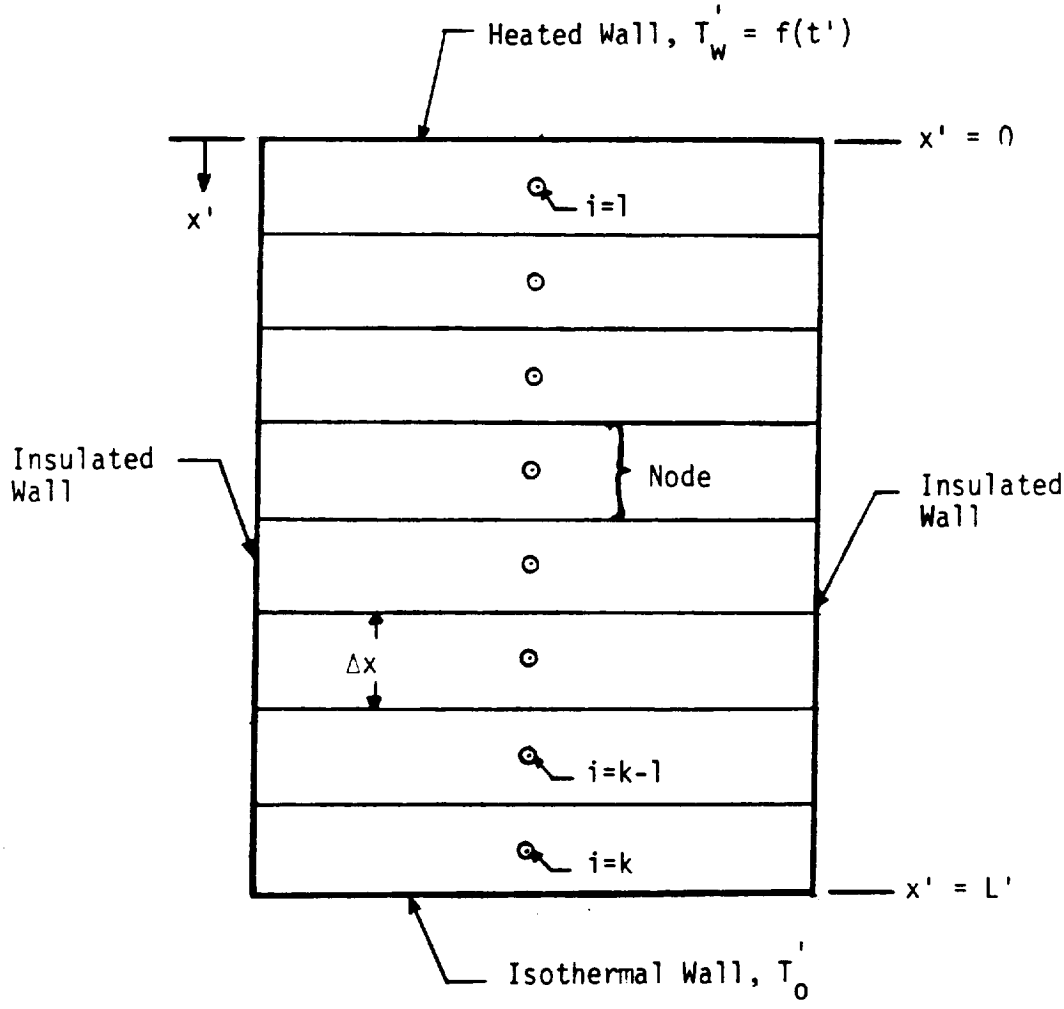

Figure IV-3. Nodal System Used in the TAC Heat Transfer Numerical Model.

Results for one run employing the low power setting and a cylinder height of one foot were obtained for both gravity and low gravity environments. A complete listing of the data used in the computations is given in Table IV-5.

In order to verify the results of the TAC computer code (Appendix E), the solution to the infinite parallel plate problem was obtained using the same boundary and initial conditions in Reference [20] and given in chapter II. The results obtained were in agreement with those presented in Figures II-6 and II-7.

Table IV-5. Geometrical Characteristics and Air Properties Used in the TAC Heat Transfer Numerical Model

Property	Value
L'	30.48 cm
$g'L' / R'T'_o$	3.516×10^{-5}
T'_o	533 °R
T'^*	1322 °R
P'_o	1.013×10^6 dyne/cm^2
ρ'_o	1.2124×10^{-3} gm/cm^3
μ'	1.8279×10^{-4} gm/cm sec
C'_v	0.1715 cal/gm °K
γ	1.4
R'	6.86×10^{-2} cal/gm-°K
K'	60.8×10^{-6} cal / cm sec°K
Δt	0.015
Δx	1/22

CHAPTER V

DISCUSSION OF RESULTS

The figures presented on the following pages represent some of the results of the analytical investigation. Each of these figures shows the non-dimensional temperature rise in the air measured at one thermocouple location along with the transient air temperature predicted by the conduction-only solution. For comparison purposes, the rise in the thermocouple temperature due to heat transfer by radiation is also presented in these figures. The results obtained for the high voltage setting and a cylinder height of 6 inches are illustrated in Figures V-1 and V-2. These figures show the significance of the radiation effects on the output of the thermocouple located at $\dot{x}$= 1.0 in. . Even for the high voltage setting (32 volts) the rate of heat transfer by conduction appears to be very small compared to the rate of heat transfer measured in the experiments.

Figure V-3 shows the temperature results obtained at $\dot{x}$=1.0 in. employing the high voltage setting (32 volts). The height of the cylinder used in the calculations was one foot. The non-dimensional air temperature presented in this figure shows similar behavior as those of Figures V-1 and V-2.

The results obtained for the low voltage setting (16

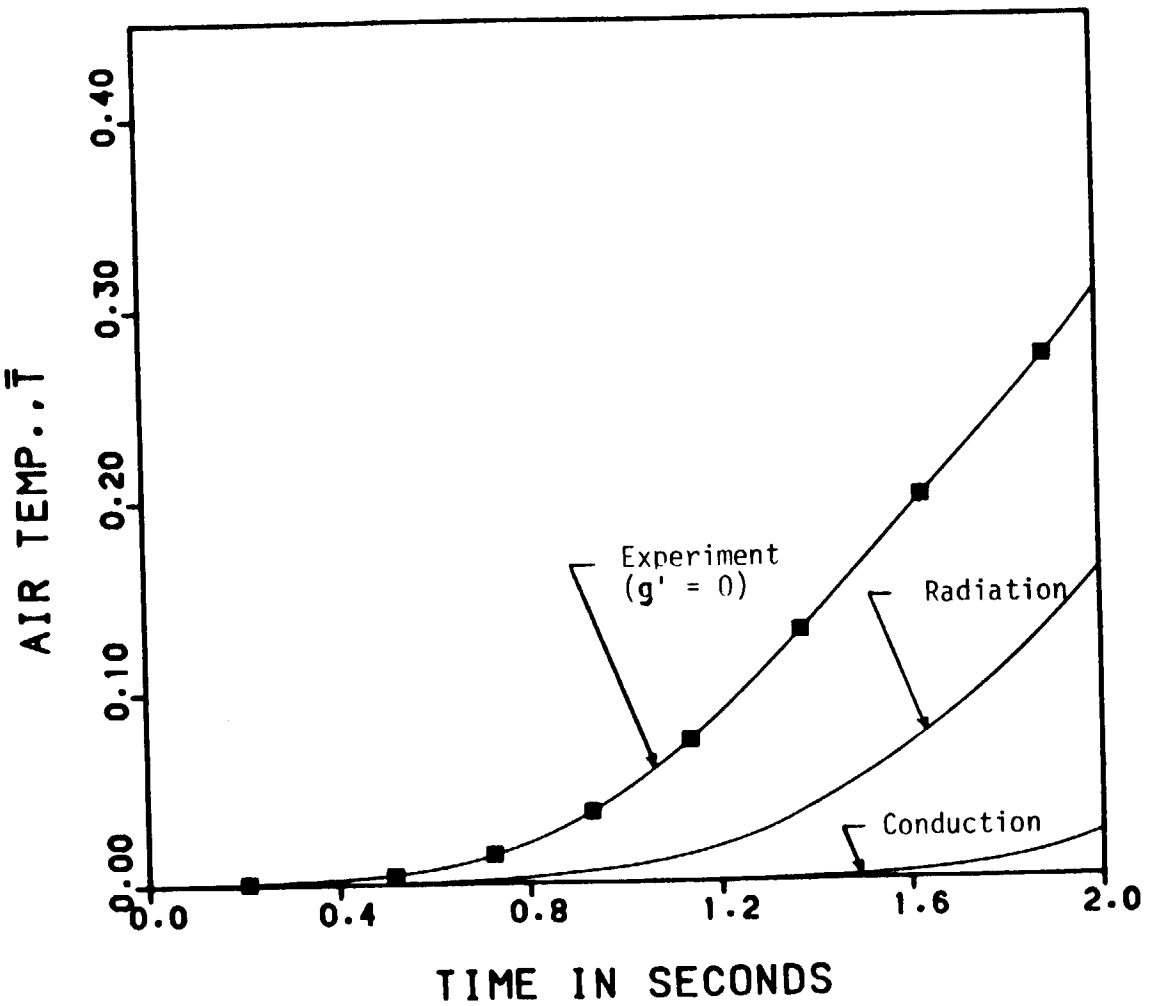

Figure V-1. Comparison of the Conduction, Radiation Effect, and Experimental Results at X'=1 in. With V_i'=36 V, L'=6 in., T'^* = 1203 °F, and T_o' = 68 °F.

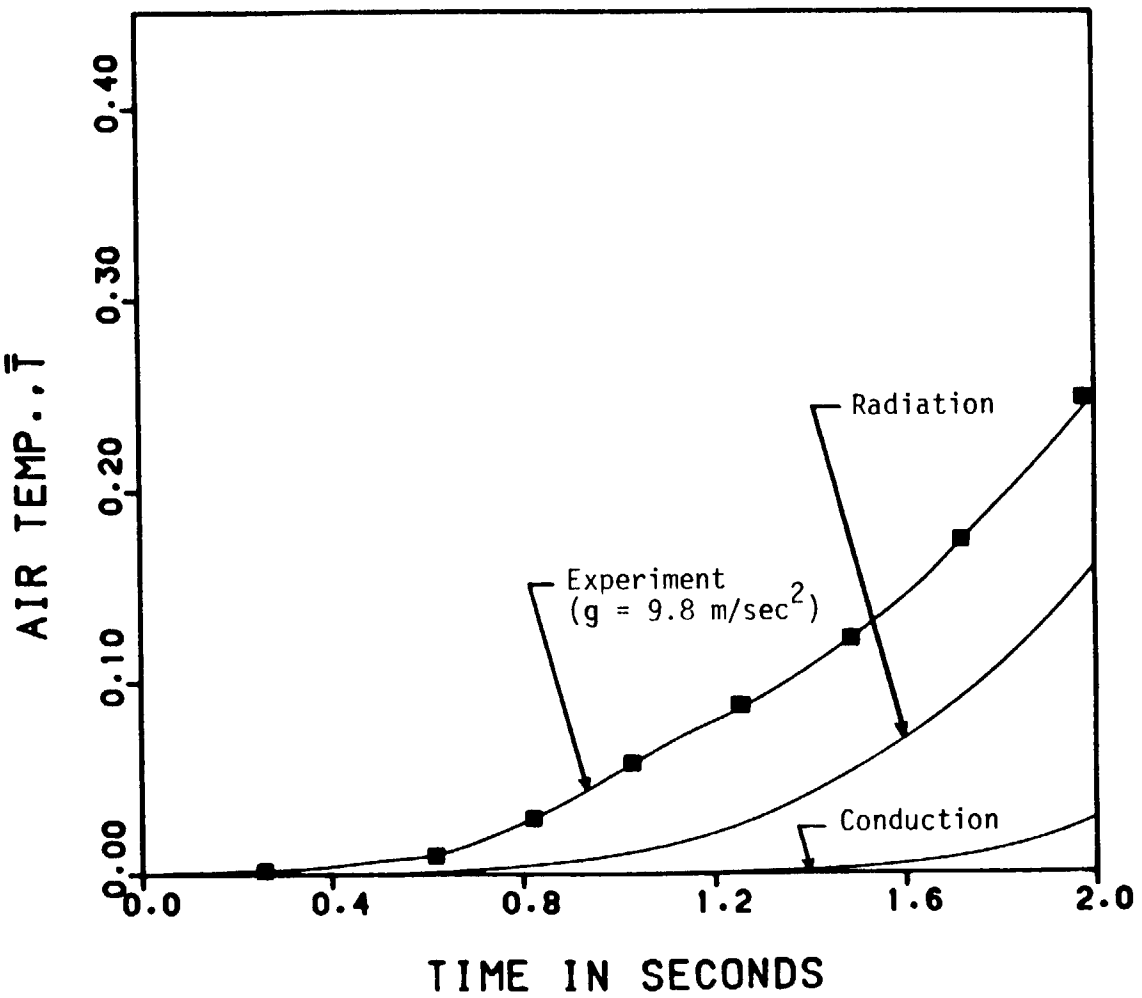

Figure V-2. Comparison of the Conduction, Radiation Effect, and Experimental Results at X'=1 in. With V_i'=36 V, L'=6 in., T'^* = 1145 °F, and T_o' = 76 °F.

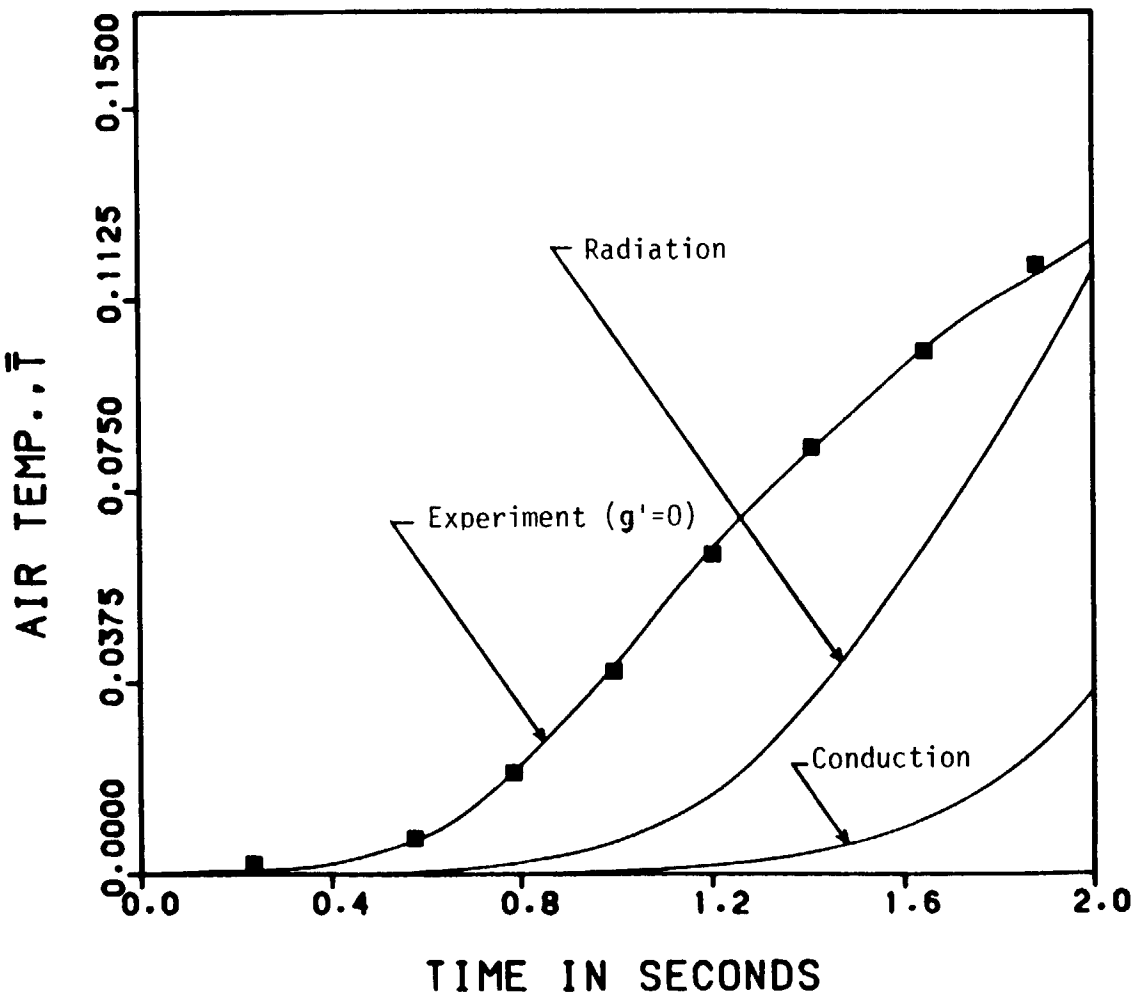

Figure V-3. Comparison of the Conduction, Radiation Effect, and Experimental Results at $\dot{X}$=2 in. With V_i'=36 V, $\dot{L}$=12 in., T'^* = 1109 °F, and T_o' = 76 °F.

volts) and short cylinder case are presented in Figures V-4 and V-5. The transient air temperature measured in the experiments at $\dot{x}$= 1.0 in. under both gravity and zero-gravity conditions shows higher values than those obtained by the conduction solution. Figure V-4 shows that, after two seconds of heating, the non-dimensional rise in the air temperature recorded during the heating process is approximately 18 times higher than its conduction counterpart and 5.5 times higher than the thermocouple temperature rise due to radiation effects. The non-dimnsional air temperature measured under gravitational conditions (Figure V-5) also shows much higher values than those calculated based on heat transfer by conduction alone.

The temperature data measured at $\dot{x}$=0.5 in. using the low voltage setting are compared to the conduction and radiation solutions in Figure V-6. With the height of the cylinder set at 6 inches, this figure shows that the non-dimensional temperature rise in the air calculated at $\dot{x}$=0.5 in. based on the conduction-only solution is consistently higher than the thermocouple temperature rise caused by heat transfer due to radiation. Also, as in previous cases, the temperatures measured in the experiments are significantly higher than the corresponding ones either in conduction-only or radiation-only heat transfer models.

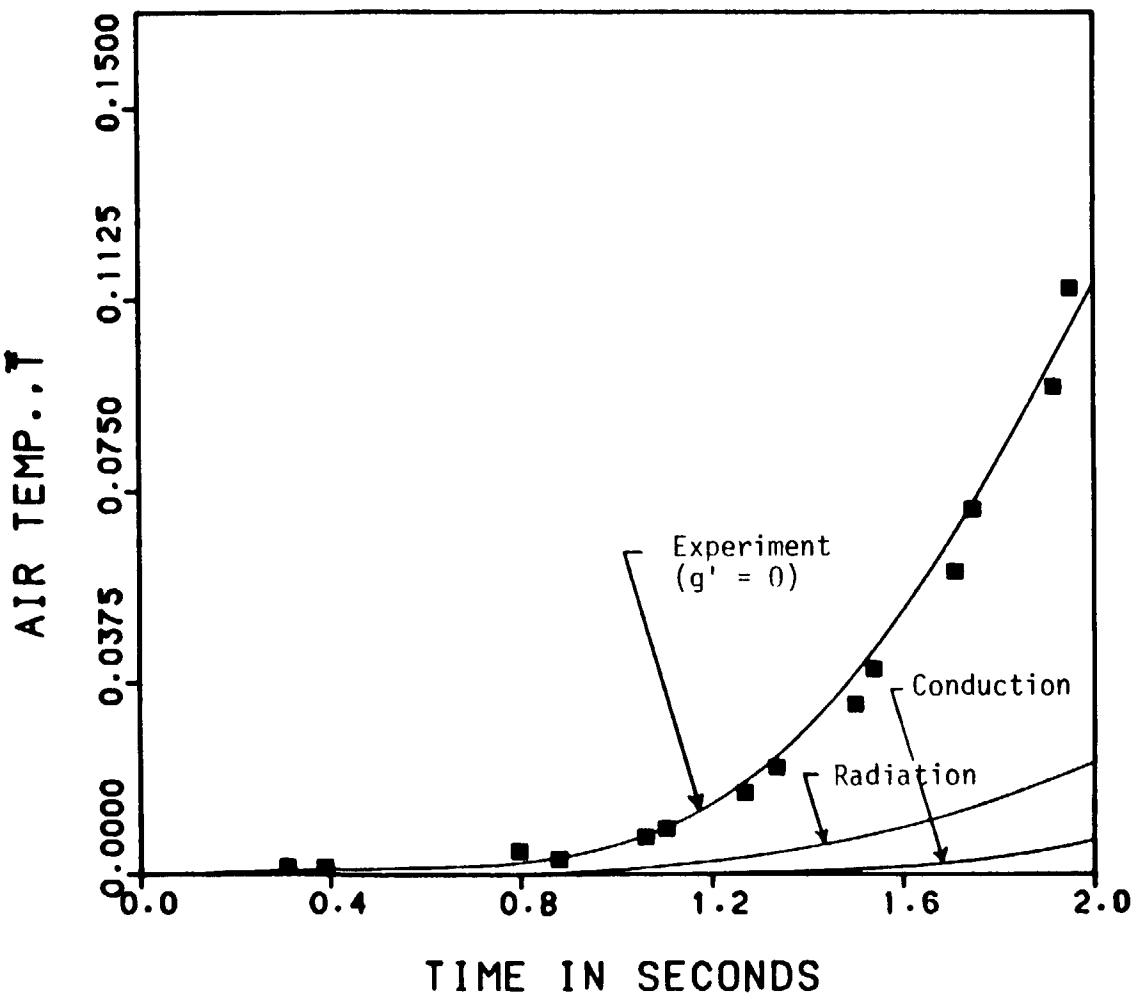

Figure V-4. Comparison of the Conduction, Radiation Effect, and Experimental Results at X=1 in. With V'_i=18 V, L=6 in., T'^* = 752 °F, and T'_o = 72 ° F.

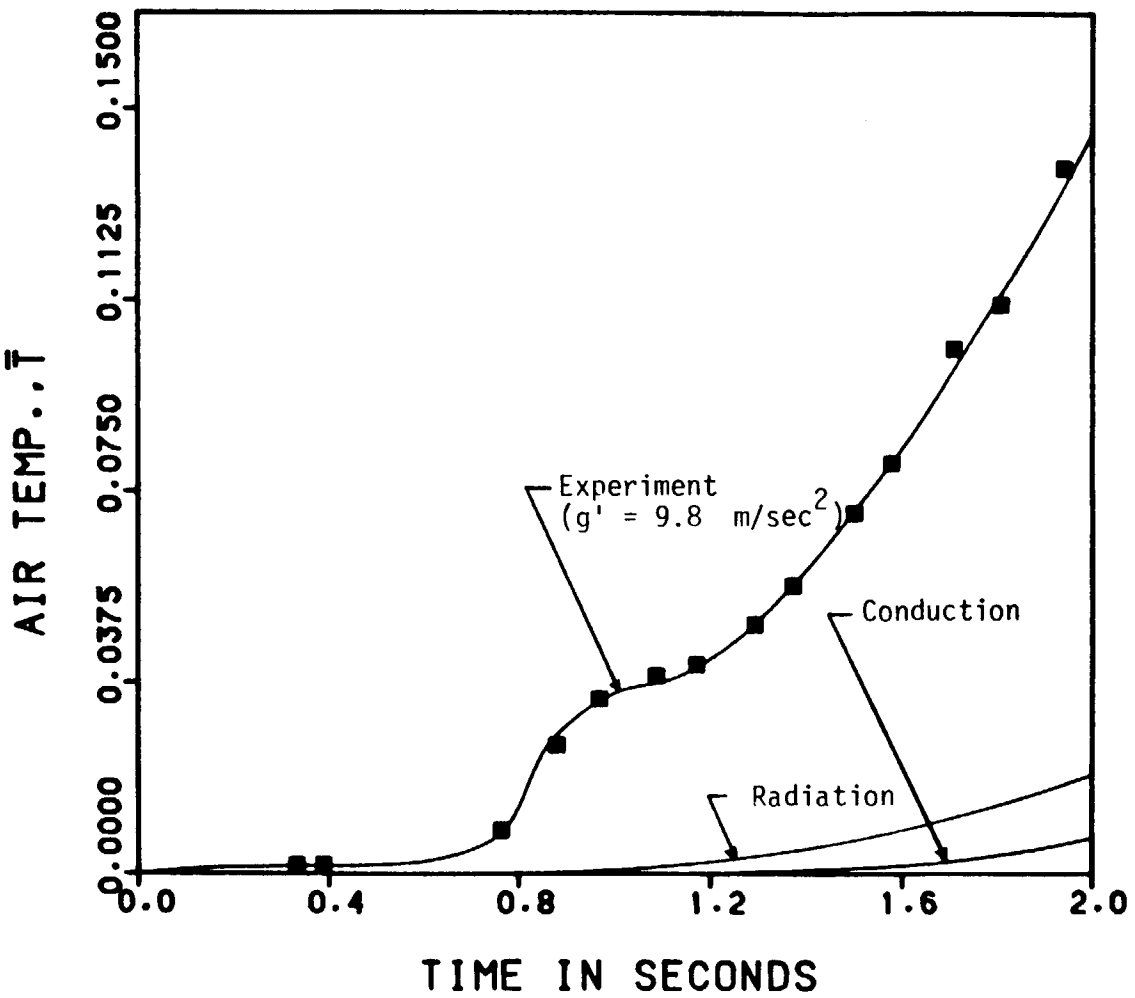

Figure V-5. Comparison of the Conduction, Radiation Effect, and Experimental Results at $X'=1$ in. With $V_i'=18$ V, $L'=6$ in., $T'^* = 664\,^\circ$F, and $T_o' = 77\,^\circ$F.

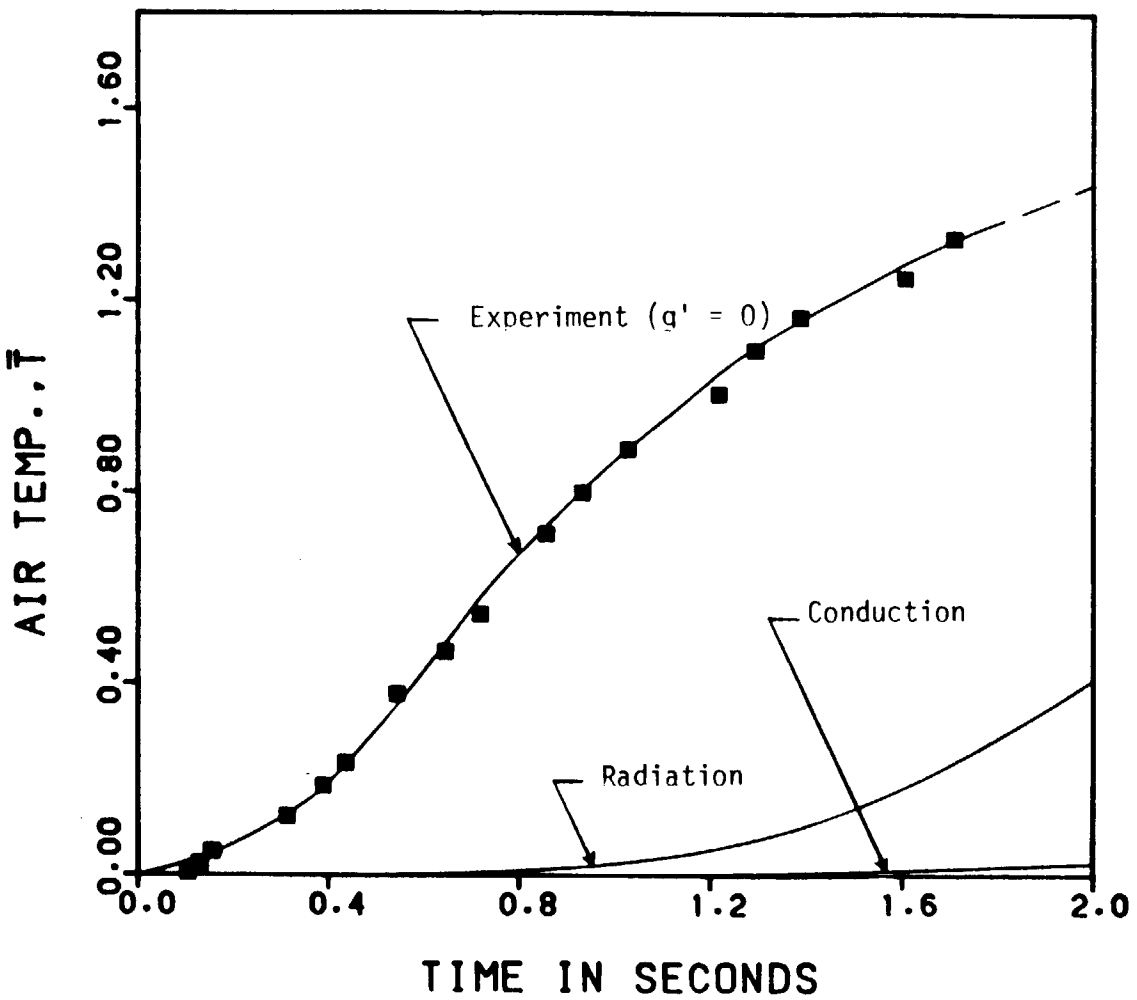

Figure V-6. Comparison of the Conduction, Radiation Effect, and Experimental Results at X'=0.5 in. With V_i'=18 V, L'=6 in., T'^*= 735 °F, and T_o' = 73 °F.

The results of the temperature measurements and the conduction and radiation numerical computations for an input voltage of 16 volts and long cylinder case (L'=12 in.) are presented in Figures V-7 and V-8. As observed, the temperature at x'=1.0 in. for pure conduction and the radiation effects on the temperature readings for this case are very small compared to the experimental data. These figures show negligible radiation and conduction temperature rise within the two seconds heating time.

It should be noted that when the radiation effects on the temperature measurements are higher than those of conduction as in all figures except Figure V-6, the combined effects of conduction and radiation are consistently smaller than the experimental results representing the thermoacoustic convection heat transfer. Also, it is important to note that in these cases since the computed temperature rise in the thermocouple due to radiation is higher than the temperature of the surrounding air, heat is lost from the thermocouple to the air and, thus, the thermocouple temperature would actually be less than that predicted by the radiation solution. When the thermocouple is placed close to the heater surface and the conduction effects become dominant as in Figure V-6, the combined conduction and radiation effects can be approximated by the sum of the temperature rise calculated by the conduction-only and the

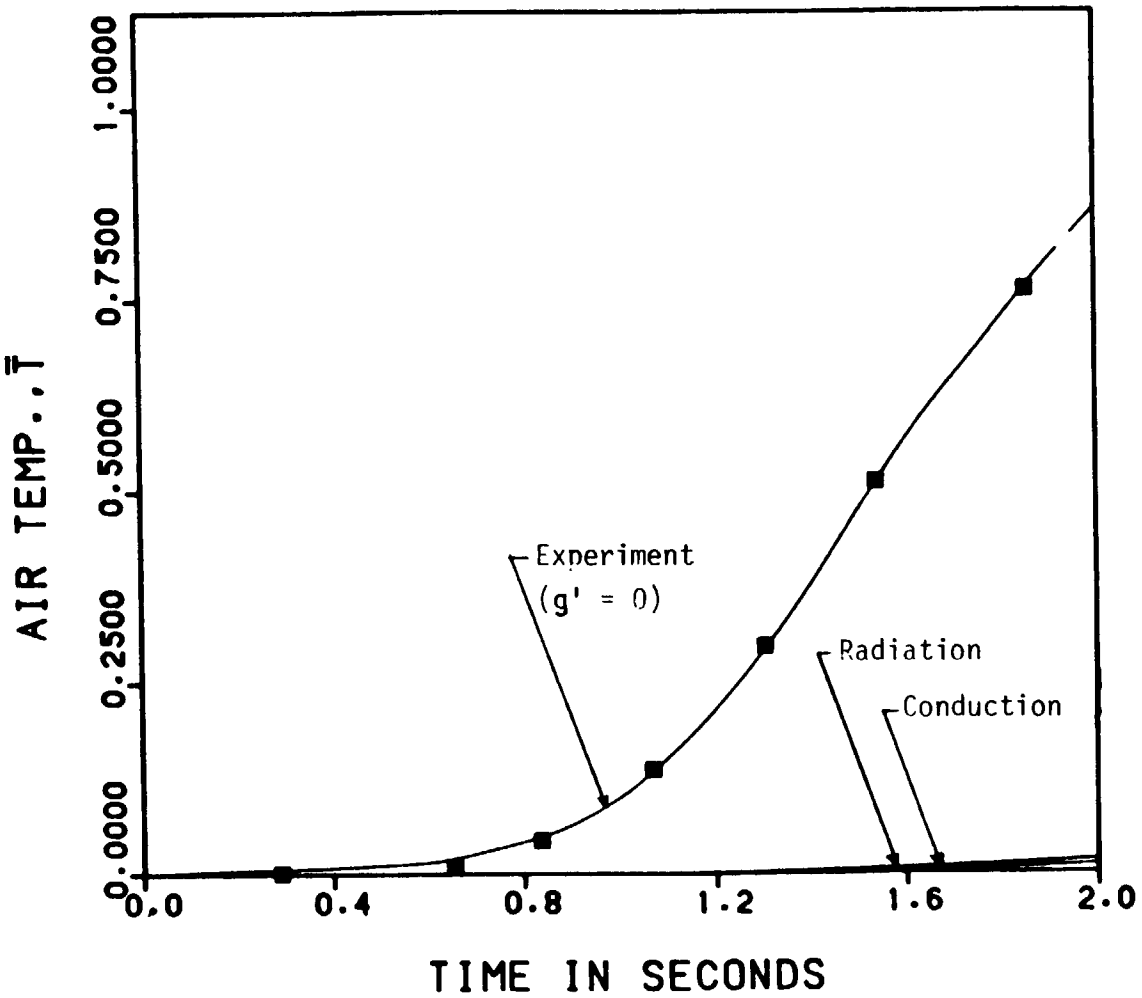

Figure V-7. Comparison of the Conduction, Radiation Effect, and Experimental Results at X'=1 in. With V'_i=18 V, L'=12 in., T'^*= 665 ° F, and T'_o = 69 ° F.

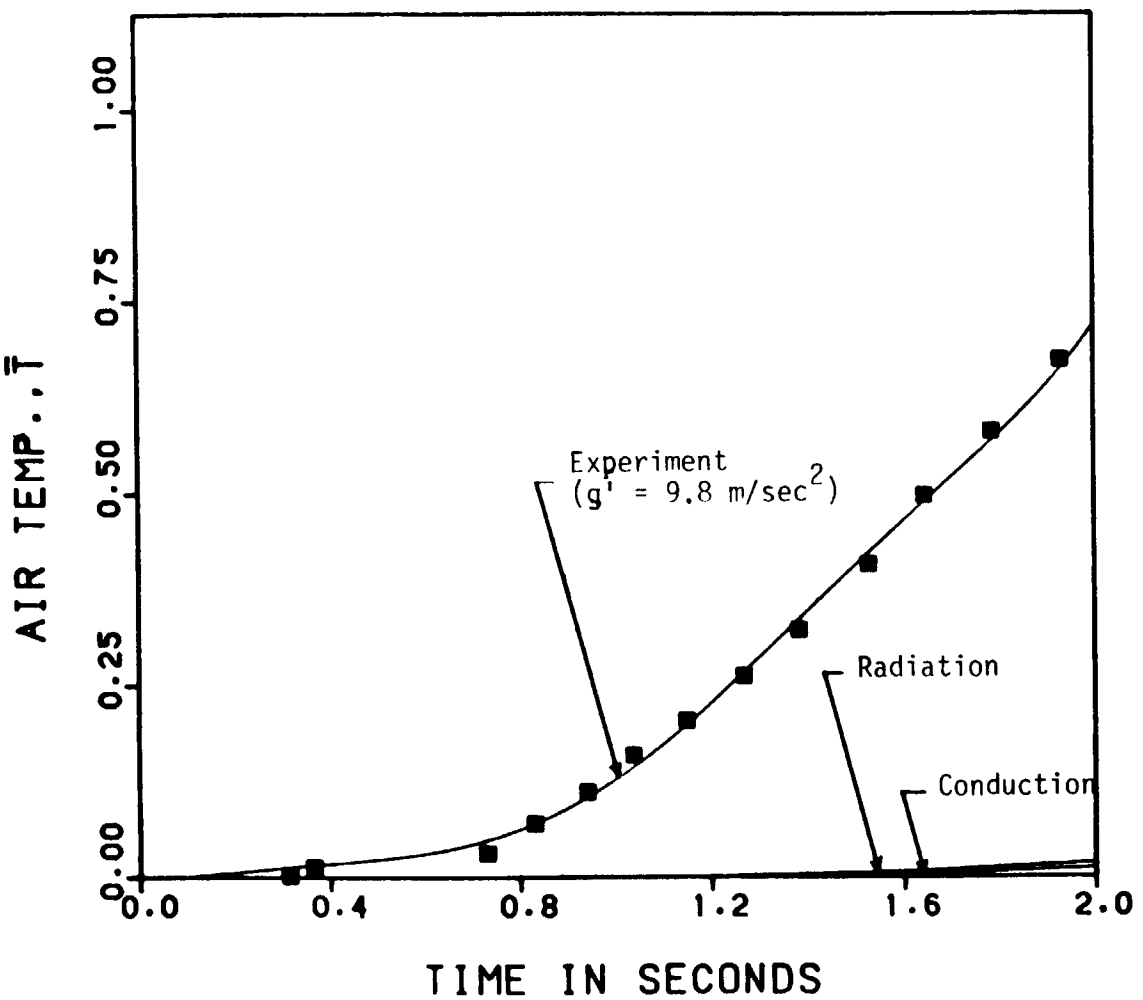

Figure V-8. Comparison of the Conduction, Radiation Effect, and Experimental Results at $X'=1$ in. With $V'_i=18$ V, $L'=12$ in., $T'^* = 701\,^\circ$F, and $T'_0 = 71\,^\circ$F.

radiation-only solutions. Thus, based on Figures V-1 to V-8, it is observed that the heat transfer rate to the air that occurred during the experiments is much higher than that calculated by the conduction-only solution. Therefore, fluid motion and convection heat transfer were present during the zero-gravity and the gravity experiments.

The difference between the TAC experimental results and the pure conduction numerical solution can be observed from a slightly different angle by examining Figure V-9. Here the non-dimensional temperature ($\bar{T}$) is presented as a function of the non-dimensional length, X'/L', at two different times for a typical case (L' = 6 in., V_i' = 16 volts) and is compared with the corresponding results from the conduction-only solution. As expected, it is observed that the region affected by the transfer of heat is significantly larger for the TAC results. Also, the temperature profiles are observed to be quite different in the two cases. That is, there is much less temperature drop away from the heated surface in the TAC mode as compared to the pure conduction mode. At the edge of the fluid layer affected by TAC the temperature drop is observed to become exceedingly sharper as shown in this figure.

The difference between the TAC and pure conduction is further emphasized when the total (cumulative) heat

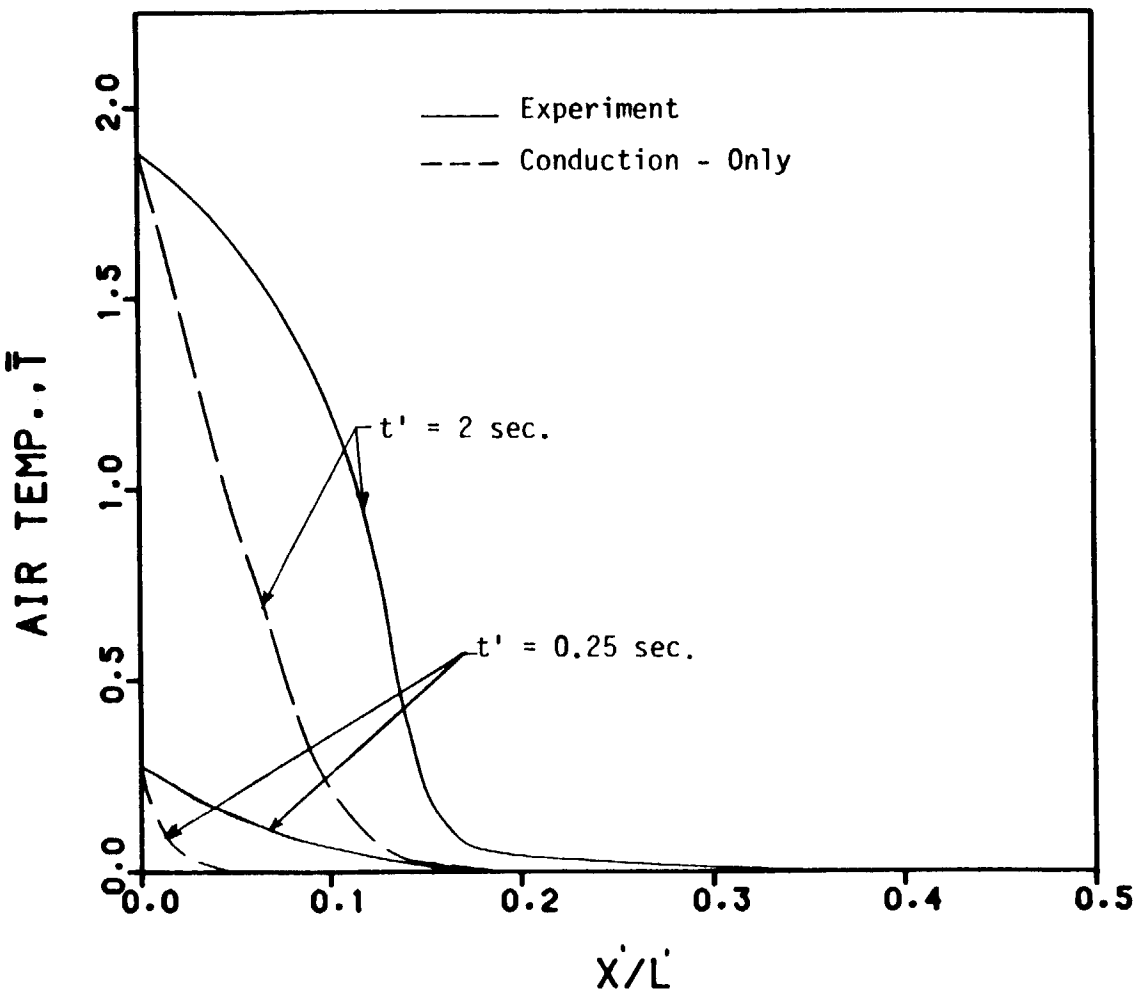

Figure V-9. Comparison of the Axial Variation of Temperature Between the Pure Conduction and the Experimental Results For V_i'=18 V, L'=6 in., T'^* = 735 °F, and T_o' =73 °F.

transfer to the air at time t' is investigated in each of these two cases. Figure V-10 illustrates the ratio of the total heat transfer to the air by TAC to that of conduction-only numerical results as a function of time. The results for this typical case (L'= 6 in., V_i'= 16 volts) show that the total TAC heat transfer can be as large as 15 times the total heat transfer by pure conduction. As expected, the ratio decreases with increase in time and should approach the steady state value of 1.

The physical reasons behind these observations is believed to be related to the differences in the fundamental mechanism of TAC and pure conduction heat transfer. Two factors that are directly related to the fluid compressibility can be singled out as responsible for the significant differences observed in the temperature and heat transfer in these two heat transfer models.

The fluid compressibilty in TAC allows for an average expansion of the heated fluid layers over longer times which contributes to the "spread" of the heated region. This explains in part the relatively larger region of heat penetration and the corresponding slower temperature drop in this region. Another important factor present in the TAC is the continuous thermal generation of pressure waves at the heated surface which

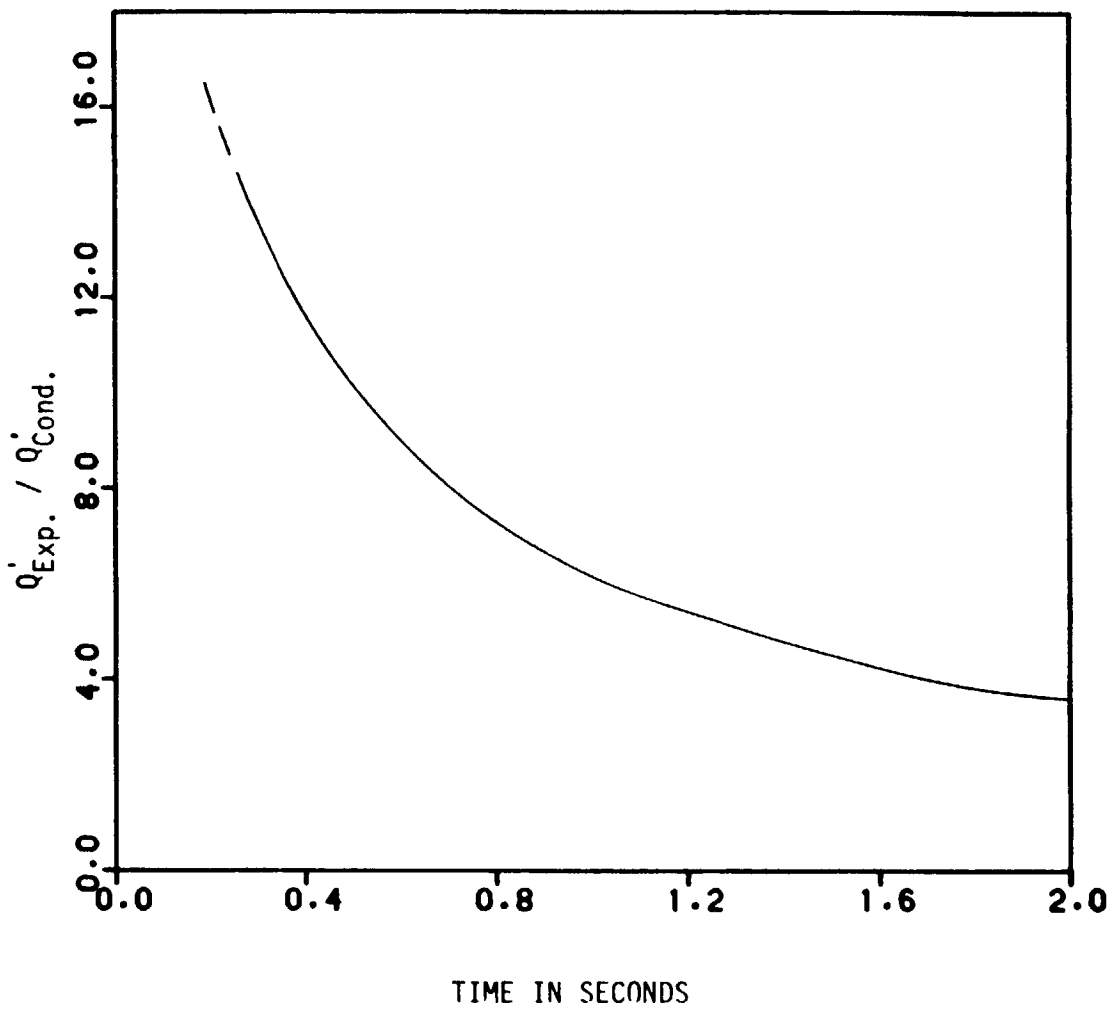

Figure V-10. The Ratio of Heat Transfer Observed Experimentally to That of Pure Conduction as a Function of Time For $V_i' = 18$ V, $L'=6$ in., $T'^* = 735$ °F, and $T_o' = 73$ °F.

are reflected by the solid boundaries of the confined region at a very rapid rate and on a much shorter time scale. These pressure waves which are initially weak compress and expand the fluid layers periodically. The fluid layers absorb more energy at the compressed mode and thus facilitate the transfer of heat through the medium. These fluid layers act as heat pumps by absorbing energy at higher pressure and releasing it at their expansion phase to the next layer and thus are akin to a series of small "Ericsson Cycles" aiding the transfer of heat through successive fluid layers.

Both of these factors, that is, an average effective expansion of the heated fluid layers and the rapid periodic compression and expansion of fluid layers, are both related fundamentally to the compressibilty of the medium in TAC which is absent in the pure conduction model. They are believed to be the basis for the larger heat penetration region, the rapid rise of the air temperature away from the heated surface, and the particular characteristic of the spatial temperature profiles in the TAC heat transfer mode.

Typical results of the thermoacoustic convection analytical model are illustrated in Figure V-11. The non-dimensional transient temperature profiles in the air were calculated for both gravity and zero-gravity conditions using the unsteady temperature boundary

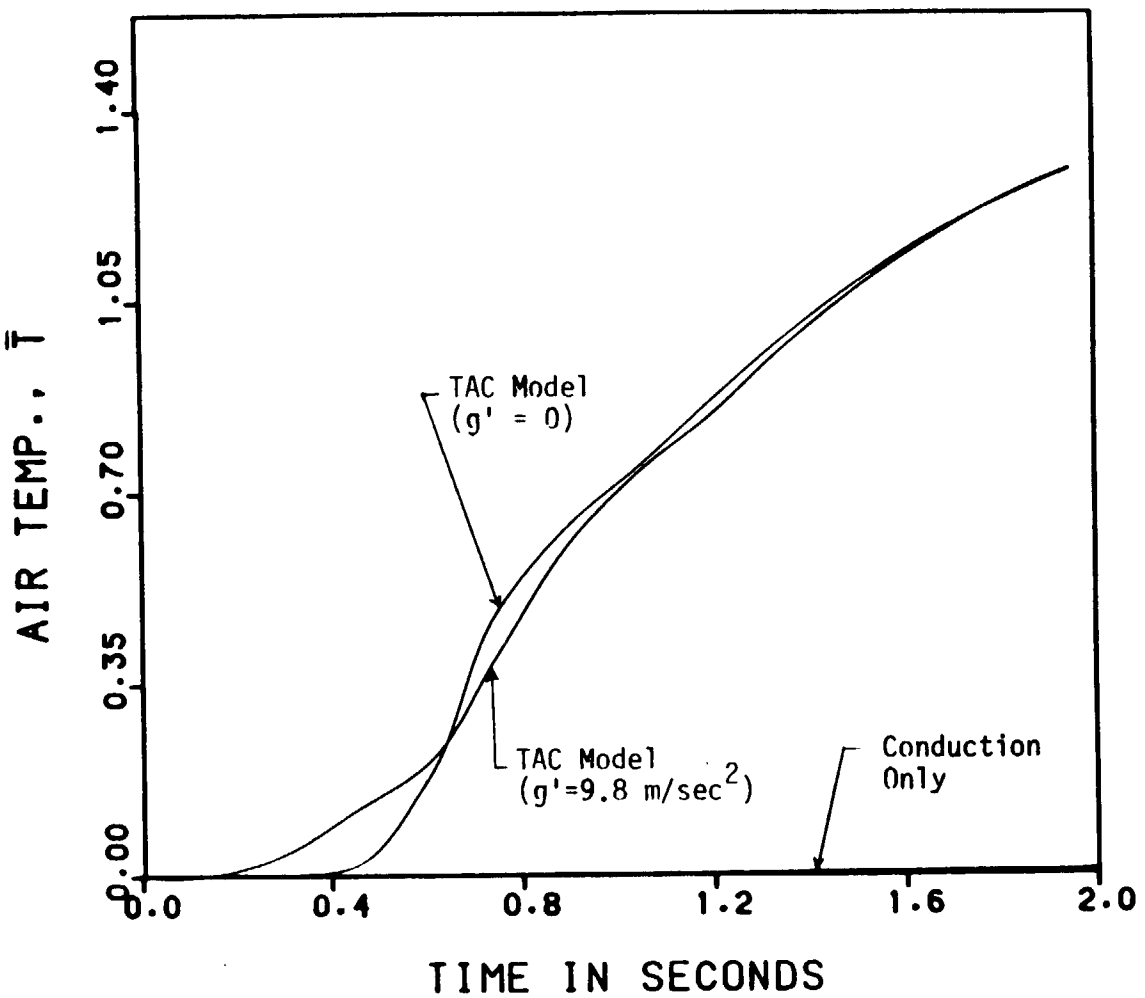

Figure V-11. Comparison of the Results of the TAC Numerical Model With the Pure Conduction Solution For V_i'=18 V, L'=12 in., T'* = 862 °F, and T_o' = 73 °F.

condition at $\dot{x}=0$ obtained from the experiments. Figure V-11 shows that the gravitational forces play an important role in enhancing the rate of heat transfer in the early stages of heating. However, as the heating continues the computed temperature distribution in the air under both gravity and zero-gravity conditions approaches equal values and eventually become identical. It is clear that during the early heating stage the rate of heat transfer to the air for $\dot{g}=0$ is small compared to that calculated in the gravity environment. As the temperature at each node in the enclosed gas rises with time it is presumed that the decrease in the local density reduce the relative importance of the gravity effects. Therefore, it is expected that the effects of gravity on the TAC heat transfer become less significant as the heating progresses. Figure V-11 shows that gravity has almost no effects on the rate of air temperature rise after 1.6 seconds of heating. It is also interesting to note that the shape of the curves representing the calculated non-dimensional air temperature are similar to those derived from the experiments. It is clearly observed that the variation of temperature with time obtained in the numerical analysis agree qualitatively with that obtained in the experimental results. However, the results of the TAC numerical model show temperature values that are much

higher than the measured data. This discrepancy is due to the following reason.

As mentioned earlier, the numerical computations presented here are based on the model used in Reference [20]. In this model the mass of the confined fluid remains fixed and no fluid is allowed to leave the container. Therefore, the computed values show large fluid pressures after short heating times. For example, based on the computed fluid properties from the one-dimensional heat transfer model of Reference [20], it is observed that after less than two seconds of heating the increase in the average fluid pressure is approximately 0.5 atmosphere (a 50 % increase). In the experimental setups used in the drop tower facility, it was not desirable to allow high fluid pressures in the cylindrical container. Therefore, no attempt was made to completely seal and leak-proof the container. Because of these reasons the numerical model does not include all of the experimental conditions and, therefore, a quantitative comparison of the computed fluid properties such as temperature with the experimental data is not appropriate. However, the numerical model provides a qualitative confirmation of the experimental results. That is, the presence of a significant TAC heat transfer is evident when the results are compared with the conduction-only solution. Also the computed results

presented in Figure V-11 illustrates the effects of the inclusion of the gravity term in the equations. Furthermore, the experimental data show that the temperature in the zero-gravity tests remain higher than in the gravity tests as also observed in the numerical results. It should however be mentioned that this difference is not significant and remains within the experimental uncertainty.

CHAPTER VI

CONCLUSIONS

Several important conclusions can be drawn from the experimental and analytical investigation of TAC heat transfer presented here. The fluid temperature measurements in both gravity and zero-gravity environments indicate a substantially larger rate of heat transfer and a more extended region of heat penetration in the experiments as compared to the pure conduction heat transfer mode. These results confirm the presence of TAC and its significance as a heat transfer mechanism. Also, it is found that the difference in the experimental results obtained for the zero-gravity and gravity environments are not significant and are within the experimental uncertainty of the experiments. As compared with the experimental observations, the numerical results of the TAC model used in this study show a much higher rate of increase for the fluid temperature in the cylindrical geometry. The reasons for this discrepancy were discussed earlier in detail.

LIST OF REFERENCES

1. Steg, L. "Materials Sciences in Space With Applications to Space Processing." Progress in Astronautics and Aeronautics, vol. 52, 1977.

2. Dodge, F. T. , "Fluid Physics, Thermodynamics, and Heat Transfer Experiments in Space: Final Report of the Overstudy Committee." NASA CR-1347842,1975.

3. Sondhauss, C. "Uber die Schallschwiagungen der Luft in Erhitzten Glasrohren Und in Gedeckten Pfeifen Von Ungleicher Weite." Annln. Physics., vol. 79.

4. Rayleigh, Lord. "The Explanation of Certain Acoustical Phenomenon." Nature, vol. 18,1878, P. 319,London.

5. Feldman, K. T. ,Jr. "A Study of Heat Generated Pressure Oscillation in a Closed End Tube." Ph.D Dissertation, Mechanical Engineering, University of Missouri, Columbia, MO, 1966.

6. Feldman, K. T. ,Jr., Carter, R. L. "A Study Of Heat Driven Pressure Oscillations in a Gas." J. Heat Transfer, vol. 92, Series C, no 3, August,1970, pp. 536-541.

7. Rijke, P. L. "Notice of a New Method of Causing a Vibration of the Air Contained in a Tube Open at Both Ends." Phil. Mag.,Ser. 4, vol. XVII,1859, pp. 419-422.

8. Blackshear, P. L. ,Jr. "Driving Standing Waves by Heat Addition." NACA Tech. Note 2772,1952.

9. Carrier, G. G. "The Mechanics of the Rijke Tube." Quarterly J. of Applied Math. ,vol. 12,pp.383-395.

10. Collyer, A. A. , Ayres, D. J. "The Generation of Sound in a Rijke Tube Using Two Heating Coils." J. of Physics. D5, pp. 174-175.

11. Collyer, A. A. , Ward, F. J. "Generation of Harmonics in a Rijke Tube by Using a Single Heated Element." J. Sound Vib. , vol. 27, pp 275-277,1973.

12. Merk, H. J. "Analysis of Heat Driven Oscillations of Gas Flow." Appl. Sci. Res. ,Sect. A. , vol. 6, pp. 402-420,1957.

13. Merk, H. J. "Analysis of Heat Driven Oscillations of Gas Flow." IV Discussion of the Theoretical Results Concerning Flame-Driven Oscillations." Appl. Sci. Res. ,A7, pp. 192-204.

14. Neuringer, J. L. , Hudson, J. E. "Investigations of Sound Vibrations in a Tube Containing a Heat Source." J. Acoust. Soc. Amer. ,vol. 24, pp.667-674,1952.

15. Bailey, J. J. "a Type of Flame Excited Oscillations in a Tube."J. Appl. Mech.,vol. 24,pp. 333-339, 1957.

16. Putnam, A. A. ,Dennis, W. R. "Organ-pipe Oscillations in a Burner With Deep Ports."J. Acous. Soc. Amer., vol. 26,pp. 260-269,1956.

17. Larkin, B. K. "Heat Flow to a Confined Fluid in Zero gravity." Prog. in Astronautics and Aeronautics: Planetary Bodies, vol. 20,1967, pp. 819-833.

18. Grodzka, P. G. , Fan,C. ,Hedden,R. O. "the Apollo 14 Heat Flow and Convection Demonstration Experiments: Final Results of the Data Analysis".LMSC-HREC D22533, Lockheed Missiles and Space co., Huntsville,Ala. , Sept., 1971.

19. Bannister, T. C, Grodzka, P. G. , Spradley, L. W. , Bourgeois, S. V. , Hedden, R. O. , and Facemire, B. R. "Apollo 17 Heat Flow and Convection Experiments:Final Results of Data Analysis." NASA TM X-64772, July, 1973.

20. Spradley, L. W., Bourgeois, S. V., Fan, C., and, Grodzka, P. G. "A Numerical Solution For Thermoacoustic Convection of Fluids in Low Gravity." Lockheed Missiles and Space Co., Huntsville Engineering and Research Centers. HREC-7015-2,LMSC-HREC TR D 306140, Jan. , 1973.

21. Krane, R. J. , Parang, M. "a Scaling Analysis of Thermoacoustic Convection in a Zero-Gravity Environment." J. of Spacecraft and Rockets, Vol 20, no. 3, May-June 1983.

22. Kreith, F. principles of Heat Transfer. Harper and Row Publishers, New York, 1973.

23. Wilkes, G. B. Total Normal Emissivities and Solar Absorptivities of Material. Wright Air Development Center., 1954

24. Brandenberg, W. M. "The Radiative Properties of Titanium and Stainless Steel With Different Surface conditions." General Dynamics Corporation, San Diego, Ca., AE 62-0289, 1962.

25. Siegel, R. , Howel, J. R. Thermal Radiation Heat Transfer. McGraw-Hill Book Company, New York, 1981.

26. Holman, J. P. Experimental Methods For Engineers . McGraw-Hill Book Company, New York,1978.

APPENDIX A

THE DESIGN AND DESCRIPTION OF THE CONTROL CIRCUIT

The control circuit consists of several DC relays, switches, and safety fuses connected as shown in Figure A-1. The circuit was designed to automatically operate the camera and the lights and to initiate and terminate the heating of the stainless steel foil. A 28-volt battery was used to activate various parts of the circuit and to supply electric power to the camera and the lights. Several preparatory steps involving the control circuit were performed before each dropping of the experimental apparatus. The following is a listing of these steps and their resulting actions:

1. Switches (S1), (S2), and (S3) were connected to the control circuit using clips (Figure A-1). These switches, located outside the shield, were used to activate the relays that control the operation of the heater, the camera, and the lights.

2. The master switch (MS) was opened, thus isolating the control circuit from the batteries.

3. Since the master switch must be closed before the shield is balanced, the camera switch (S1), the heater switch (S2), and the time delay relay (TDR) switch (S3) were closed thus activating relays R1, R2, and R3. By closing these switches the camera, the heater, and the lights remain disconnected from the batteries after closing the master switch.

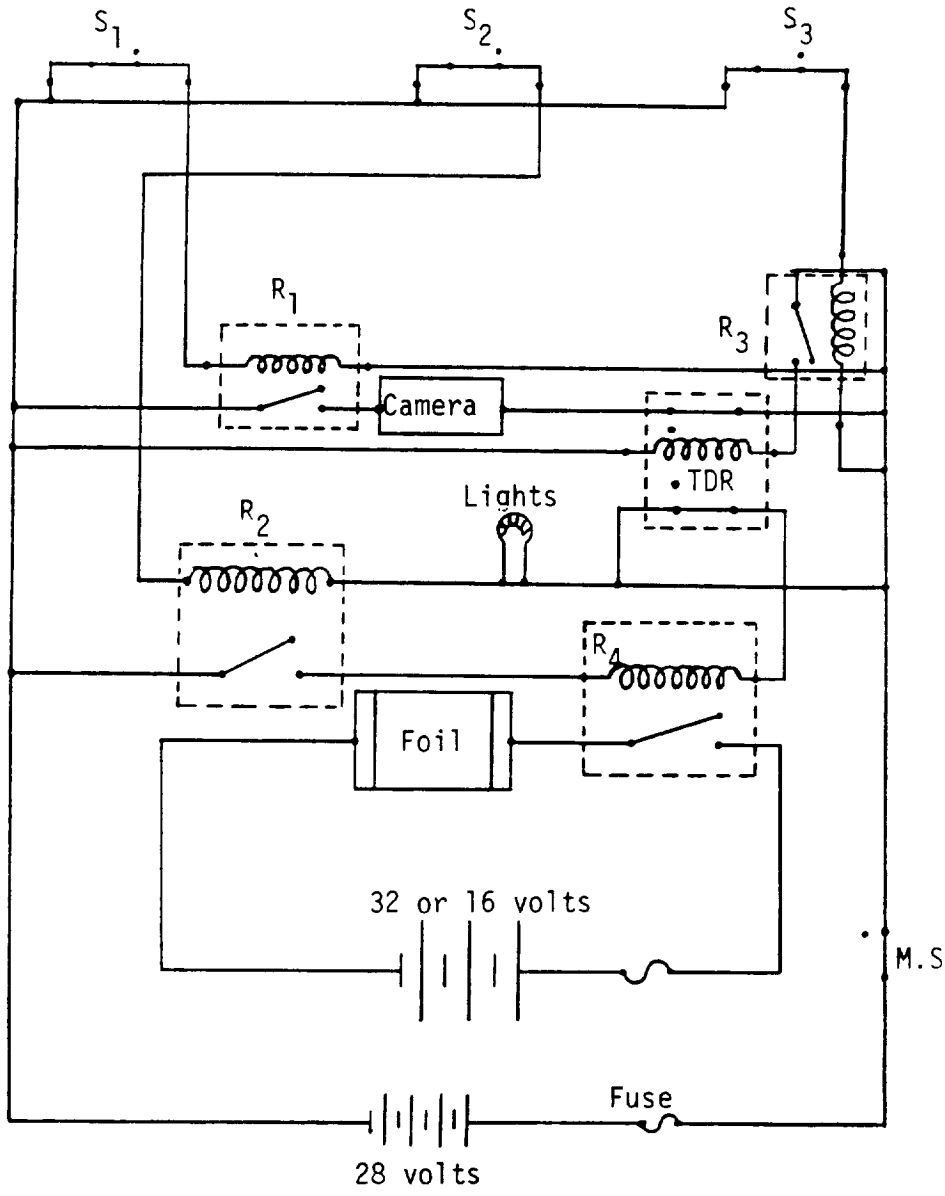

Figure A-1. Schematic Diagram of the Control Circuit.

4. The master switch was then closed and the apparatus was balanced.

5. To preheat the steel foil prior to the dropping of the apparatus, the heater switch is opened. This will also cause the lights to turn on marking the start of the heating on the film. The camera switch was always opened few seconds prior to the start of the heating to allow the camera motor to reach a uniform speed.

6. When the drop is initiated switch (S1), (S2), and (S3) become open. This activates the time delay relay which shuts off the power supply to the heater, the camera, and the lights after a preset time. The TDR was set at 3 seconds throughout the experiments to allow for temperature measurements during the 2-seconds free fall.

APPENDIX B

COMPUTER PROGRAM USED FOR TEMPERATURE MEASUREMENTS

```
**********************************************
*                                            *
*  AIR TEMPERATURE MEASUREMENTS USING THE    *
*           HP  9826  COMPUTER               *
*                                            *
**********************************************
**********************************************
*                                            *
*  THIS PROGRAM WAS  USED TO MEASURE THE     *
*  HEATING SURFACE  TEMPERATURE AND THE AIR  *
*  TEMPERATURE AT TWO  LOCATIONS INSIDE THE  *
*  CYLINDER.                                 *
*                                            *
**********************************************

DIM V(47,2),TS(47,2),TEF(47,2)
GINIT
GRAPHICS ON
FRAME
WINDOW -1,7,-100,1800
AXES 1.0,200
LORG 6
FOR I=-1 TO 6
MOVE I,0
LABEL I
NEXT I

LORG 8
FOR I=0 TO 1700 STEP 200
MOVE 0,I
LABEL I
NEXT I

LORG 5
MOVE 0,0
MOVE 3,1650
LABEL "PLOT OF TEMP. VS. TIME CH. 0"
MOVE 0,0
PRINTER IS 701
PRINT
PRINT "THERMOCOUPLE LOCATION";TAB(19);"TEMP(C)"
;TAB(32);"TEMP(F)";TAB(53);"TIME(SEC)"
PRINT
CLEAR 709
OUTPUT 709;"VR1VA0SO1"

!CURVE FIT COEFFICIENTS FOR VOLTAGE TO TEMP.
!CONVERSION.
```

```
R0=1.23773E-7
R1=5.866E-5
R2=4.5E-8
P0=2.1E-1
P1=1.61299E+4
P2=-2.05411E+5
P3=3.049432E+7
P4=-2.9690242E+9
P5=1.4284958E+11
P6=-3.7221944E+12
P7=5.3981272E+13
P8=-4.1055295E+14
P9=1.2777466E+15

OUTPUT 709; "AC3"
ENTER 709; R
V1=R
TIN=TIMEDATE
FOR I=1 TO 47
FOR N= 0 TO 2
TIF=TIMEDATE
TS(I,N)=TIF-TIN
OUTPUT 709; "AC";N

ENTER 709;V2
V(I,N)=-V1+V2
NEXT N
NEXT I

TF=TIMEDATE
TRI=TF-TIN
FOR I=1 TO 47
FOR N=0 TO 2
Y1=V(I,N)*(P6+V(I,N)*(P7+V(I,N)*(P8+V(I,N)*P9)))
Y2=V(I,N)*(P3+V(I,N)*(P4+V(I,N)*(P5+Y1)))
T1=P0+V(I,N)*(P1+V(I,N)*(P2+Y2))
T2=32+1.8*T1
TEC=INT(T1*100+0.5)/100
TEF(I,N)=INT(T2*100+0.5)/100
PRINT N;TAB(18);TEC;TAB(31);TEF(I,N);TAB(51);TS(I,N)
NEXT N
PRINT
NEXT I

!PLOTTING THE RESULTS
FOR I=1 TO 47
DRAW TS(I,0),TEF(I,0)
NEXT I
WAIT 60
DUMP DEVICE IS 701,EXPANDED
```

```
DUMP GRAPHICS
WAIT 60
MOVE 0,0
GINIT
FRAME
WINDOW -1,7,-50,300
AXES 1.0,25
LORG 6
FOR I=0 TO 6
MOVE I,0
LABEL I
NEXT I
LORG 8
FOR I=0 TO 275 STEP 25
MOVE 0, I
LABEL I
NEXT I
MOVE 0,0
LORG 5
MOVE 3,275
LABEL"PLOT OF TEMP(F) VS. TIME (SEC)"
MOVE 3,250
LABEL "FOR X=2 IN. AND X=3 IN."
MOVE 0,0
FOR I=1 TO 47
DRAW TS(I,1),TEF(I,1)
NEXT I
MOVE 0,0
FOR I=1 TO 47
DRAW TS(I,2),TEF(I,2)
NEXT I
WAIT 60
DUMP DEVICE IS 701,EXPANDED
DUMP GRAPHICS
END
```

Table B-1. The Results Of the Temperature Measurements Using the HP 9826 Computer With Input Voltage = 24 volts and Cylinder Height = 0.5 ft.

Thermocouple No.	Time (sec)	Temperature (°F)
0	0.0	67.11
1	0.06	66.57
2	0.11	66.57
0	0.16	86.16
1	0.21	66.69
2	0.26	66.63
0	0.31	112.97
1	0.36	66.91
2	0.41	66.80
0	0.46	155.28
1	0.51	67.45
2	0.56	67.22
0	0.61	208.15
1	0.66	68.58
2	0.71	68.05
0	0.76	269.04
1	0.81	70.51
2	0.86	69.41
0	0.90	333.78
1	0.95	73.48
2	1.00	71.50
0	1.05	401.29
1	1.10	77.54
2	1.15	74.33

Table B-1 (continued)

Thermocouple No.	Time (sec)	Temperature (°F)
0	1.20	469.14
1	1.25	82.50
2	1.30	77.74
0	1.35	536.31
1	1.40	88.09
2	1.45	81.60
0	1.50	601.98
1	1.55	94.04
2	1.60	85.76
0	1.65	666.09
1	1.70	100.05
2	1.75	89.97
0	1.80	729.59
1	1.85	105.89
2	1.90	94.07
0	1.94	791.00
1	1.99	111.39
2	2.04	97.99

Thermocouples No. 0, 1, and 2 represent thermocouple location at $x' = 0$, $x' = 1$, and $x' = 2$ in., respectively.

Table B-2. The Results of the Temperature Measurements Using the Omega Digital Thermometers with Input Voltage = 24 volts and Cylinder Height = 0.5 ft.

Time (sec)	T'_w(°F)	T'_1(°F)	T'_2(°F)
0.0000	68	67	67
0.1342	86		
0.2683		68	
0.4024	126		
0.5366			68
0.6037	199		
0.6707		69	
0.8049	294		
0.8720		72	
1.0732	407	78	74
1.3415		86	80
1.4085	541		
1.5427		94	86
1.7439		103	92
1.8110	688		
2.0122	764	111	98

T'_w, T'_1, and T'_2 represent the measured temperature at x' = 0 in., x' = 1 in., and x' = 2 in.

APPENDIX C

CONDUCTION HEAT TRANSFER COMPUTER PROGRAM

```
C       ***********************************************
C       *                                             *
C       *   CONDUCTION SOLUTION ASSUMING VARIABLE     *
C       *                PROPERTEIS                   *
C       *                                             *
C       ***********************************************
C
C       ***********************************************
C       *                                             *
C       *  THIS PROGRAM SOLVES THE ONE-DIMENSIONAL    *
C       *  TRANSIENT HEAT CONDUCTION EQUATION TO      *
C       *  CALCULATE THE TEMPERATURE DISTRIBUTION     *
C       *  IN AN ENCLOSED AIR MEDIUM ASSUMING VAR-    *
C       *  IABLE THERMAL CONDUCTIVITY AND DENSITY.    *
C       *  THE AIR IS HEATED AT ONE SURFACE WHILE     *
C       *  THE OTHER BOUNDARY IS KEPT AT CONSTANT     *
C       *  TEMPERATURE.THE TRANSIENT TEMPERATURE OF   *
C       *  THE HEATER SURFACE IS APPROXIMATED BY A    *
C       *  POLYNOMIAL CURVE FIT EQUATION.             *
C       *                                             *
C       ***********************************************
C
C       ***********************************************
C       *                                             *
C       *  THE VARIABLES USED ARE:                    *
C       *    TER----GAS INITIAL TEMPERATURE (R)       *
C       *    TEO----GAS INITIAL TEMPERATURE (F)       *
C       *    TAV----AVERAGE HEATER SURFACE TEMP.(F)   *
C       *    DX-----SPACE INCREMENT (IN)              *
C       *    DTS----TIME INCREMENT (SEC.)             *
C       *    CP-----GAS SPECIFIC HEAT                 *
C       *    CH-----CYLINDER HEIGHT (FT.)             *
C       *    TK-----GAS THERMAL CONDUCTIVITY          *
C       *    DE-----GAS DENSITY                       *
C       *                                             *
C       ***********************************************
C
        DIMENSION TE(49),DE(49),TK(49),AL(48),BE(48)
       1  ,A(48),B(48),C(48),D(48),E(48),TOLD(49)
C
C-------COEFFICIENTS OF THE SURFACE TEMP. EQ.
C
        AA=137.2328
        BB=-451.9775
        CC=90.60042
        DD=836.3806
        EE=-962.0433
        FF=1688.746
C
```

```
          WRITE(22,31)
  31      FORMAT(//,23X,'CONDUCTION SOLUTION FOR D41'//)
          TEO=76.0
          CH=0.5
          TAV=1083
C
C-------LO IS THE NO. OF NODE PTS.
C
          LO=49
          LOM=LO-1
C
C-------MESH SIZE
C
          DX=CH/LOM
          D2X=DX*DX
C-------TIME STEP
          DTS=0.01
          NO=(2.0/DTS)+1
          T=0.0
          TER=TEO+460.0
          TAVR=TAV+460.0
          TS=TEO
          DTH=DTS/3600
          CP=0.240
          NN=1
C
C-------INITIAL CONDITIONS
C
          DO 1 I=1,LO
          TE(I)=TER
  1       CONTINUE
C
C-------SOLVING THE CONDUCTION EQUATION
C
          DO 2 N=1,NO
          IF(NN .NE. N)  GO TO 95
          NN=NN+10
          Q=(1.889E-5*((TS+TE(2)-460)/2.0)+0.0133)
          1  *0.4583*(TS-TE(2)+460)/DX
C
C-------PRINT OUT LOOP
C
          WRITE(22,3),T,TS,Q
   3      FORMAT(//,23X,'TIME=',F4.2,1X,'SEC',5X,'T-WALL='
          1  ,F7.2,1X,'(F)',2X,'HEAT TRAN.='F7.2,1X,'BTU/HR'
          1  ,//)
          WRITE(22,4)
  4       FORMAT(21X,'I',8X,'X/L',13X,'TE(I)',13X,'T-NON',/)
          DO 5 I=1,LO
          X=(I-1)*DX/CH
```

```
          TNON=(TE(I)-TER)/(TAVR -TER)
          TEF=TE(I)-460
          WRITE(22,16),I,X,TEF,TNON
 16       FORMAT(20X,I2,6X,F5.3,11X,F8.3,10X,F8.4)
  5       CONTINUE
C
C-------EVALUATING THE THERMAL PROPERTIES
C
  95      DO 6 I=1,LO
          TOLD(I)=TE(I)
          TT=TE(I)-460.0
          TK(I)=1.8889E-5*TT+0.0133
          DE(I)=-0.8247572E-24*(TT**6)+0.6407921E-19*
          1  (TT**5)+0.4295403E-14*(TT**4)-0.3562589E-10*
          1  (TT**3)+0.1019464E-6 *TT*TT-0.1310382E-3*TT
          1  +0.086
  6       CONTINUE
C
C-------CALCULATING THE NEW TEMPERATURE
C
          T=N*DTS
          TESF=AA*(T**6)+BB*(T**5)+CC*(T**4)+DD*(T**3)
          1  +EE*T*T+FF*T+TEO
          TS=TESF
          TE(1)=(TESF+460+TOLD(1))/2.0
          DO 7 I=2,LOM
          B(I)=(TK(I)+TK(I-1))/(2.0*D2X)
          C(I)=(TK(I)+TK(I+1))/(2.0*D2X)
          D(I)=(DE(I)*CP)/DTH
          A(I)=2.0*D(I)+B(I)+C(I)
          E(I)=2.0*D(I)-B(I)-C(I)
  7       CONTINUE
C
C-------CALCULATING ALPHA(2) AND BETA(2)
C
          AL(2)=(E(2)*TOLD(2)+C(2)*TOLD(3)+B(2)*(TOLD(1)
          1  +TE(1)))/A(2)
          BE(2)=C(2)/A(2)
C
C-------CALCULATING ALPHA(I) AND BETA(I)
C
          DO 8 I=3,LOM
          F=A(I)-B(I)*BE(I-1)
          AL(I)=(E(I)*TOLD(I)+B(I)*TOLD(I-1)+C(I)*
          1  TOLD(I+1)+AL(I-1)*B(I))/F
          BE(I)=C(I)/F
  8       CONTINUE
C
          DO 9 I=2,LOM
          II=LOM+2-I
```

```
      TE(II)=AL(II)+BE(II)*TE(II+1)
9     CONTINUE
2     CONTINUE
      STOP
      END
```

APPENDIX D

RADIATION HEAT TRANSFER COMPUTER PROGRAM

```
C       ********************************************
C       *                                          *
C       *   ESTIMATION OF THE RADIATION EFFECTS ON *
C       *            THERMOCOUPLE OUTPUT           *
C       *                                          *
C       ********************************************
C
C       ********************************************
C       *                                          *
C       *  THIS PROGRAM CALCULATES THE RISE IN THE *
C       *  THERMOCOUPLE TEMPERATURE  AT TWO LOCA-  *
C       *  TIONS IN THE AIR  CAUSED BY RADIATION   *
C       *  HEAT TRANSFER.                          *
C       *                                          *
C       ********************************************
C
C       ********************************************
C       *                                          *
C       *  THE VARIABLES USED ARE:                 *
C       *    BD1-----DIAMETER OF THE FIRST THERMO- *
C       *            COUPLE AT THE JUNCTION (IN).  *
C       *    H1------DISTANCE BETWEEN THE FIRST    *
C       *            THERMOCOUPLE AND THE HEATER   *
C       *            (IN).                         *
C       *    CH------CYLINDER HEIGHT (IN)          *
C       *    TFF-----GAS INITIAL TEMPERATURE (F)   *
C       *    TBF1----INITIAL TEMPERATURE OF THE    *
C       *            FIRST THERMOCOUPLE (F).       *
C       *    TBF2----INITIAL TEMPERATURE OF THE    *
C       *            SECOND THERMOCOUPLE (F).      *
C       *    BD2-----DIAMETER OF THE SECOND THERMO-*
C       *            COUPLE AT THE JUNCTION (IN).  *
C       *    H2------DISTANCE BETWEEN THE SECOND   *
C       *            THERMOCOUPLE AND THE HEATER   *
C       *            (IN).                         *
C       *    TAV-----AVERAGE HEATER SURFACE TEMP-  *
C       *            ERATURE (F)                   *
C       *    BDE-----DENSITY OF THE THERMOCOUPLE   *
C       *            AT THE JUNCTION.              *
C       *    BCP-----SPECIFIC HEAT OF THE THERMO-  *
C       *            COUPLE AT THE JUNCTION.       *
C       *    RS------INSULATION REFLECTIVITY       *
C       *    ES------EMISSIVITY OF THE STAINLESS   *
C       *            FOIL.                         *
C       *    DR------DISK RADIUS (IN).             *
C       *    AD------DISK AREA  (IN**2)            *
C       *    AF------AREA OF THE HEATER SURFACE (IN)*
C       *                                          *
C       ********************************************
C
```

```
          WRITE(24,31)
   31     FORMAT(//,23X,'RADIATION SOLUTION FOR D41',//)
C
C-------INPUT DATA
C
          BD1=0.01
          H1=2.0
          CH=12.0
          TFF=76.0
          TBF1=TFF
          TBF2=TFF
          BD2=0.01
          H2=3.0
          TAV=1083.0
          TE01=TFF
          TE02=TFF
C
C-------ENTERING THE COEFFICIENTS OF THE SURFACE
C-------TEMPERATURE CURVE FIT POLYNOMIAL
C
          A=137.2328
          B=-451.9775
          C=90.60042
          D=836.3806
          E=-962.0433
          F=1688.746
          G=76
C
C-------THERMOCOUPLE MATERIAL PROPERTIES
C
          BDE=551.0
          BCP=0.100
          RS=0.80
         SI=1.714E-9
          DR=6.00
          AD=0.7854
          AF=0.4583
C
C-------CALCULATING THE SURFACE AREA AND VOLUME
C-------OF THE THERMOCOUPLES.
C
          ASG1=4.0*3.1416*((BD1/24.0)**2)
          VG1=(3.1416*4.0/3.0)*((BD1/24.0)**3)
          ASG2=4.0*3.1416*((BD2/24.0)**2)
          VG2=(3.1416*4.0/3.0)*((BD2/24.0)**3)
          AW=2.0*3.1416*DR*CH/144.0
C
C-------CALCULATING THE CONFIGURATION FACTORS
C
          FB11 =(1.0-1.0/((1+(DR/H1)**2)**0.5))/2.0
```

```
          FB21 =(1.0-1.0/((1+(DR/H2)**2)**0.5))/2.0
          F1B1 =(ASG1/AD)*FB11
          F1B2 =(ASG2/AD)*FB21
          X1=CH-H1
          X2=CH-H2
          FB14=(1.0-1.0/((1+(DR/X1)**2)**0.5))/2.0
         FB24 =(1.0-1.0/((1+(DR/X2)**2)**0.5))/2.0
          FB12 =1.0-FB11-FB14
          FB22=1.0-FB21-FB24
          F2B1=(ASG1/AW)*FB12
          F2B2=(ASG2/AW)*FB22
C
          R1=DR/CH
          P1=R1**2
          X=1+(1+P1)/P1
          F14=(X-((X**2-4)**0.5))/2.0
          F12=1.0-F14
C
C-------MAIN BODY OF THE PROGRAM
C
          WRITE(24,5)
    5     FORMAT(5X,'TIME(SEC)',5X,'TC#',5X,'DIRECT INC.
          1  RAD,',5X,'REF. INC. RAD.',5X,'EMMITTED RAD.'
          1  ,5X,'ENERGY GAIN' ,5X,'*','TB(F)',5X,'(TB-T0)/
          1  /(TAV-T0)')
C
          WRITE(24,9)
   9      FORMAT (31X,'(BTU/HR)',11X,'(BTU/HR)',11X,'(BTU/HR)'
          1  ,11X,'(BTU)')
C
          WRITE(24,10)
    10    FORMAT( /)
          DT=0.05
          T=0.0
C
C-------TEMPERATURE CALCULATIONS
C
          DO 15 I=1,41
          T11=TFF
          TFF=A*T**6+B*T**5+C*T**4+D*T**3+E*T**2+F*T+G
          TEF=(T11+TFF)/2.0
C
C--------EMISSIVITY CURVE FIT COEFFICIENTS
C
          A1=0.129247E-25
          A2=0.1057093E-15
          A3=-0.1811926E-12
          A4=-0.1640302E-9
          A5=0.4788375E-6
          A6=-0.1528234E-3
```

```
          A7=0.21
          ES=A1*(TEF**6)+A2*(TEF**5)+A3*(TEF**4)+A4*
          1  (TEF**3)+A5*(TEF**2)+A6*TEF+A7
          IF(ES .GT. 0.6)   ES=0.6
          TER=TEF+460
          P=ES*SI*AF*(TER**4)
          DIR1=F1B1*P*0.47
          DIR2=F1B2*P*0.47
C
          Q=RS*F12*P
C
          RIR1=F2B1*Q*0.47
          RIR2=F2B2*Q*0.47
C
          TBR1=TBF1+460
          TBR2=TBF2+460
C
          ER1=SI*ASG1*(TBR1**4)*0.47
          ER2=SI*ASG2*(TBR2**4)*0.47
C
          N=1
          L=2
          DE1=DIR1+RIR1-ER1
          DE2=DIR2+RIR2-ER2
          EG1=DE1*DT/3600
          EG2=DE2*DT/3600
          IF(EG1 .LT.0.0 .OR. EG2 .LT. 0.0) GO TO 26
C
C-------CALCULATING THE NEW THERMOCOUPLE TEMPERATURE
C
          TBF1=(EG1/(BDE*BCP*VG1))+TBF1
          TBF2=(EG2/(BDE*BCP*VG2))+TBF2
C
          RIO1=(TBF1-TE01)/(TAV-TE01)
          RIO2=(TBF2-TE02)/(TAV-TE02)
C
C-------PRINTING THE RESULTS
C
  26     WRITE(24,20),T,N,DIR1,RIR1,ER1,EG1,TBF1,RIO1
  20      FORMAT(6X,F4.2,10X,I1,E18.4,3 X,E18.4,E18.4,3X,
          1  E16.4,4X,'*',F6.2,8X,F7.5)
          WRITE(24,30),L,DIR2,RIR2,ER2,EG2,TBF2,RIO2
   30     FORMAT(20X,I1,E18.4,3X,E18.4,E18.4,3X ,E16.4
          1  ,4X,,'*',F6.2,8 X,F7.5)
C
          WRITE(24,11)
  11      FORMAT(/)
          T=T+DT
   15     CONTINUE
          END
```

APPENDIX E

THERMOACOUSTIC CONVECTION HEAT TRANSFER COMPUTER PROGRAM

```
C        ********************************************
C        *                                          *
C        *    THERMOACOUSTIC CONVECTION COMPUTER    *
C        *                PROGRAM                   *
C        *                                          *
C        ********************************************
C        ********************************************
C        *                                          *
C        * THIS PROGRAM CALCULATES THE TRANSIENT    *
C        * VELOCITY, DENSITY, PRESSURE, AND TEMPER- *
C        * ATURE DISTRIBUTION INSIDE AN AIR MEDIUM  *
C        * AT SEVERAL TIME LEVELS. THE AIR IS HEAT- *
C        * ED AT ONE BOUNDARY WHILE THE OTHER IS    *
C        * KEPT AT CONSTANT TEMPERATURE.            *
C        *                                          *
C        ********************************************
C        ********************************************
C        *                                          *
C        *  THE VARIABLES USED ARE:                 *
C        *    DT-----NON-DIMENSIONAL TIME INCREMENT *
C        *    DX-----NON-DIMENSIONAL GRID SPACING   *
C        *    L------CYLINDER HEIGHT (CM)           *
C        *    TEO----INITIAL TEMPERATURE (R)        *
C        *    TBF----INITIAL TEMPERATURE (F)        *
C        *    TAV----AVERAGE HEATER SURFACE TEMP-   *
C        *           ERATURE (F)                    *
C        *    DEO----INITIAL AIR DENSITY            *
C        *    V------AIR VISCOUSITY                 *
C        *    CV-----AIR SPECIFIC HEAT              *
C        *    C------AIR THERMAL CONDUCTIVITY        *
C        *    PEO----INITIAL PRESSURE IN THE AIR    *
C        *    G------RATIO OF SPECIFIC HEATS        *
C        *    R------IDEAL GAS CONSTANT OF AIR      *
C        *    RN-----REYNOLD'S NUMBER               *
C        *    PR-----PRANDTL NUMBER                 *
C        *    U------NON-DIMENSIONAL VELOCITY       *
C        *    P------NON-DIMENSIONAL PRESSURE       *
C        *    DE-----NON-DIMENSIONAL DENSITY        *
C        *    TE-----NON-DIMENSIONAL TEMPERATURE    *
C        *    TW-----HEATER SURFACE TEMPERATURE     *
C        *                                          *
C        ********************************************
C
        DOUBLE PRECISION U(22,2),DE(22,2),TE(22,2)
      $,DXUU(22,2),D2XU(22,2),DEU(22,2),DXP(22,2)
      $,DXDEU(22,2),DXTE(22,2),DXU(22,2),D2XTE(22,2)
      $,DEU2(22,2),VI(22,2),DPR(22,2)
C
C-------GEOMETRICAL DATA AND INITIAL CONDITIONS
C
```

```
          DT=0.015
          L=30.48
          COF=3.5157E-5
          TEO=533.0
          TBF=73
          TAV=1322.0
C
C-------COEFFICIENT OF THE HEATER SURFACE TEMP.
C-------CURVE FIT EQUATION
C
          AA=126.50
          BB=-779.69
          CC=1581.43
          DD=-880.48
          EE=-930.85
          FF=1914.03
C
C-------AIR INITIAL PROPERTIES
C
          DEO=1.2124E-3
          V=1.8279E-4
          CV=0.1715
          C=60.7689E-6
          PEO=1.013E6
          G=1.4
C
C-------CALCULATING RE NO. AND PR NO.
C
          R=53.34
          SRTO=((R*32.2*TEO)**0.5)*(12*2.54)
          DTP=(DT*L)/SRTO
          PP=0.15/DTP
          M=(2.0/DTP)+2
          MO=M-51
          RN=(DEO*L*SRTO)/V
          PR=(V*G*CV)/C
          TEB=(TBF+460)/TEO
C
C-------NUMBER OF NODE POINTS AND GRID SPACING
C
          LO=22
          DX=1.0/22.0
          LOPM=LO-1
          NO=1
          NI=1
          N=1
C
C-------INITIAL CONDITIONS
C
          DO 1 I=1,LO
```

```
          U(I,1)=0.0
          TE(I,1)=(TBF+460)/TEO
          P(I,1)=1.0
          DE(I,1)=1.0
  1       CONTINUE
C
          PRINT 6
  6       FORMAT('1',///)
  340     TI=(NI-1)*DT
          TRI=(TI*L)/SRTO
          T=TRI
C
C-------CALCULATING THE HEATER SURFACE TEMPERATURE
C-------USING THE POLYNOMIAL CURVE FIT EQUATION
C
          TW=AA*(T**6)+BB*(T**5)+CC*(T**4)+DD*(T**3)
        $+EE*(T**2)+FF*T+TBF
          TTEF=TW+460
          TEW=TEF/TEO
          IF(NI .GT. MO) GO TO 2
          IF(NI .LT. NO) GO TO 3
          NO=NO+PP
C
C-------PRINT STATEMENT
C
  2       PRINT 4 ,NI,TI,TRI,TW
  4      FORMAT(//23X,'TIME STEP=',I6,5X,'TI=',F8.3,
        $5X,'TRI=',F7.5,1X,'SEC',3X,'T-WALL',3X,F8.2,//)
          PRINR 21
  21      FORMAT(22X,'I',4X,'DIS',10X,'U(I,N)',14X,
        $'P(I,N)',13X,'DE(I,N)',13X,'TE(I,N)',13X,
        $'TNON',/)
C
          DO 60 I=1,LO
          TO=TE(I,N)*TEO
          TNON=(TO-TEO)/(TAV-TEO)
          DIS=DX/2.0+(I-1)*DX
          PRINT 61,I,DIS,U(I,N),P(I,N),DE(I,N),TE(I,N)
        $TNON
  61      FORMAT(21X,I2,3X,F5.3,7X,F9.6,12X,F8.6,12X,
        $F8.6,12X,F8.6,11X,F8.6)
  60      CONTINUE
C
C-------SOLVING THE MOMENTUM EQUATION
C
          DXUU(1,N)=(DE(1,N)*(U(1,N)**2)+DE(2,N)*(U(2,N)
        $**2))/(2.0*DX)
          D2XU(1,N)=(U(2,N)-3.0*U(1,N))/(DX*DX)
          DXP(1,N)=(P(2,N)-P(1,N))/DX
C
```

```
          DO 7 I=2,LOM
          IF(U(I-1,N) .LT. 1E-30 .AND. U(I-1,N) .GT.
        $-1E-30)   U(I-1,N)=0.0
          IF(U(I,N) .LT. 1E-30 .AND. U(I,N) .GT. -1E-30)
        $   U(I,N)=0.0
          IF(U(I+1,N) .LT. 1E-30 .AND. U(I+1,N) .GT.
        $-1E-30)    U(I+1,N)=0.0
          DEU2(I+1,N)=DE(I+1,N)*U(I+1,N)*U(I+1,N)
          DEU2(I,N)=DE(I,N)*U(I,N)*U(I,N)
          DEU2(I-1,N)=DE(I-1,N)*U(I-1,N)*U(I-1,N)
C
          DXUU(I,N)=(DEU2(I,N)-DEU2(I-1,N))/DX
          IF(U(I,N) .LT. 0.0)  DXUU(I,N)=(DEU2(I+1,N)
        $-DEU2(I,N))/DX
          DXP(I,N)=(P(I+1,N)-P(I-1,N))/(2.0*DX)
          D2XU(I,N)=(U(I+1,N)-2.0*U(I,N)+U(I-1,N))/
        $(DX*DX)
  7       CONTINUE
C
          DXUU(LO,N)=(-1.0*(DE(LO,N)*(U(LO,N)**2)+DE(LOM,
        $N)*(U(LOM,N)**2)))/(2.0*DX)
          DXP(LO,N)=(P(LO,N)-P(LOM,N))/DX
          D2XU(LO,N)=(U(LOM,N)-3.0*(U(LO,N)))/(DX*DX)
C
C-------CALCULATING DX*U AT A NEW TIME LEVEL
C
          DO 8 I=1,LO
          TF=(TE(I,1)*TEO)-460.0
          V1=(0.98/1000)*TF+1.49
          IF(TF .LT. 500)  V1=(1.5491/1000)*TF+1.1154
          IF(TF .GT. 500 .AND. TF .LT. 1000)  V1=
        $1.16/1000)*TF+1.31
          VI(I)=14.8798E-5*V1
          DEU(I,N+1)=DE(I,N)*U(I,N)-DT*(DXUU(I,N)+DXP
        $(I,N)-COF*DE(I,N)-4.0*(VI(I)/V)*D2XU(I,N)/3.0
        $*RN)
  8       CONTINUE
C
C-------SOLVING THE CONTINUITY EQUATION
C
          DXDEU(1,N+1)=(DEU(2,N+1)+DEU(1,N+1))/(2.0*DX)
          DXDEU(LO,N+1)=-1.0*(DEU(LO,N+1)+DEU(LOM,N+1))
        $/(2.0*DX)
C
          DO 9 I=2,LOM
          DXDEU(I,N+1)=(DEU(I+1,N+1)-DEU(I-1,N+1))/2.0
        $*DX)
  9       CONTINUE
C
C-------CALCULATING THE NEW DENSITY AND VELOCITY
C-------PROFILES
C
```

```
          DO 10 I=1,LO
          DE(I,N+1)=DE(I,N)-DT*(DXDEU(I,N+1))
          U(I,N+1)=DEU(I,N+1)/DE(I,N+1)
  10      CONTINUE
C
C-------SOLVING THE ENERGY EQUATION
C
          DXTE(1,N)=(TE(1,N)-TEW)/(0.5*DX)
          IF(U(1,N) .LT  0.0)  DXTE(1,N)=(TE(2,N)-TE(1,N)
        $)/DX
          DXU(1,N+1)=(U(1,N+1)+U(2,N+1))/(2.0*DX)
          D2XTE(1,N)=TE(2,N)-3.0*TE(1,N)+2.0*TEW)/(DX*DX)
          D2XTE(1,N)=(4.0/3.0)*D2XTE(1,N)
C
          DXTE(LO,N)=(TE(LO,N)-TE(LOM,N))/DX
          IF(U(LO,N) .LT. 0.0) DXTE(LO,N)=(TEB-TE(LO,N))
        $/(0.5*DX)
          DXU(LO,N+1)=-1.0*(U(LO,N+1)+U(LOM,N+1))/(2.0*DX)
          D2XTE(LO,N)=(TE(LOM,N)-3.0*TE(LO,N)+2.0*TEB)/(DX*DX)
          D2XTE(LO,N)=(4.0/3.0)*D2XTE(LO,N)
C
          DO 11 I=2,LOM
          DXTE(I,N)=(TE(I,N)-TE(I-1,N))/DX
          IF((U(I,N) .LT. 0.0)   DXTE(I,N)=(TE(I+1,N)-
        $TE(I,N))/DX
          DXU(I,N+1)=(U(I+1,N+1)-U(I-1,N+1))/(2.0*DX)
          D2XTE(I,N)=(TE(I+1,N)-2.0*TE(I,N)+TE(I-1,N))/
        $(DX*DX)
  11      CONTINUE
C
C-------CALCULATING THE NEW TEMPERATURE
C
          DO 12 I=1,LO
          BI=(G/(RN&PR))*(VI(I)/V)*D2XTE(I,N)/DE(I,N+1)
          TE(I,N+1)=TE(I,N)-DT*(U(I,N+1)*DXTE(I,N)+(((G-
        $1)*P(I,N)*DXU(I,N+1))/DE(I,N+1))-BI
  12      CONTINUE
C
C-------CALCULATING THE NEW PRESSURE
C
          DO 13 I=1,LO
          P(I,N+1)=DE(I,N+1)*TE(I,N+1)
  13      CONTINUE
C
          DO 16 I=1,LO
          U(I,1)=U(I,2)
          P(I,1)=P(I,2)
          DE(I,1)=DE(I,2)
          TE(I,1)=TE(I,2)
  16      CONTINUE
C
```

```
NI=NI+1
IF(NI .LT. M) GO TO 340
STOP
END
```

APPENDIX F

UNCERTAINTY ANALYSIS FOR THE EXPERIMENTAL RESULTS

The uncertainty in the experimental results was determined based on the uncertainty in the time measurements and the uncertainty in the temperature readings. Also, the uncertainty in the results of the radiation heat transfer model was estimated based on the uncertainty in the emissivity-temperature data of stainless steel. The uncertainty in time is assumed to be due to the uncertainty in the uniformity of the speed of the camera used to record the temperature display of the thermometers. This uncertainty was evaluated using the camera speed data obtained from the experimental results. The following presents the analysis performed to determine the uncertainties in experimental and numerical results.

Uncertainty in the Time Measurements

The time corresponding to a specific temperature measured and recorded was calculated using the number of film frames exposed prior to the display of that temperature. The uncertainty in the number of film frames exposed during any specific time interval results in the uncertainty in the time measurement. The method of evaluation of the uncertainty in time is presented below.

The total number of film frames exposed during the entire 3-second heating period is determined to be

$N' = 116 \pm 1$ frames

Therefore, the uncertainty in the camera speed (S') is calculated to be

$S' = 38.67 \pm 0.33$ frames/sec

The time prior to a temperature measurement is given by

$t' = N'/S'$

where N' is the number of exposed frames

The maximum uncertainty in the time calculations ($w'_{t_{max}}$) which occur at the end of the 2-second heating time ($N' = 77$ frames) is then used for the time measurement.

$w'_{t_{max}} = \pm 0.026$ seconds

The uncertainty in the temperature measured by the digital thermometers is provided by the manufacturer (Omega inc.) as

$w'_T = 0.8 \pm 0.1$ % of the temperature reading in ^{o}C

Finally, the uncertainty in the location of the thermocouples is estimated to be

$$w' = \pm 0.02 \text{ in}$$

It is important to mention that the uncertainty in the temperature measurements due to the time response of the digital thermometers was greatly reduced by the data correction procedure discussed in chapter III. The Data Acquisition System which was used to reduce the error due to the thermometer response time is estimated to have a time response less than 0.02 seconds. Therefore, as shown above, the greatest uncertainty in the temperature-time measurements is seen to be due to the uncertainties in the thermometer and the camera speed.

Uncertainty In The Calculated Thermocouple Temperature Rise Caused By Radiation Heat Transfer

As mentioned in chapter IV, the accuracy in the calculated temperature rise of the thermocouple due to heat transfer by radiation strongly depends on the accuracy of the steel foil emissivity-temperature data used in the calculations. Although the stainless steel emissivity values given in References [23] and [24] are in good agreement, an estimation of the error in the temperature results of the radiation heat transfer model was performed using the highest and lowest

emissivity-temperature data given in the above references. The results show that, after two seconds of heating, the maximum uncertainty in the calculated temperature rise of the thermocouple caused solely by radiaticn heat transfer is approximately ± 6 ^{o}F and ±12 ^{o}F for the low voltage setting (16 volts) and the high voltage setting (32 volts), respectively.

APPENDIX G

EXPERIMENTAL DATA

In the following tables subscripts 1, 2, 3, and 4 denote thermocouple locations at $\dot{x}$= 1 in., 2 in., 3 in., and 4 in. for a cylinder height of 1 ft. and at $\dot{x}$= 0.5 in., 1.0 in., 1.5 in., and 2.0 in. for a cylinder height of 0.5 ft., respectively.

Zero-Gravity Test
Cylinder Height 1 ft.
Input Voltage 18 Volts

Time (sec)	$T_w^{\cdot}$ (°F)	$T_2^{\cdot}$ (°F)	$T_3^{\cdot}$ (°F)
0.0000	73	73	73
0.1293	439		
0.3103		74	
0.3879			74
0.4397	707		
0.7500		75	
0.8534	1016		
0.9052			75
0.9828		76	
1.1379			77
1.1897		78	
1.3448			79
1.3707	1329		
1.3966		81	
1.5517			82
1.5776		85	
1.7328			85
1.7586		89	
1.9138			88
1.9397	1573		
2.0172		94	
2.1207	impact		

Zero-Gravity Test
Cylinder Height 1 ft.
Input Voltage 18 Volts

Time (sec)	T'_w (°F)	T'_2 (°F)	T'_3 (°F)
0.0000	74	75	75
0.1293	286		
0.3879			76
0.4397	498	76	
0.7759	756		
0.9828		77	77
1.1638	1044		
1.1897		78	
1.2931			78
1.3966		80	
1.5000			80
1.6034		83	
1.6552	1320		
1.6810			82
1.8103		86	
1.8362	1417		84
2.0172		91	
2.0690			86
2.2241	1530		
2.1207	impact		

Zero-Gravity Test
Cylinder Height 1 ft.
Input Voltage 18 Volts

Time (sec)	T'_w (°F)	T'_2 (°F)	T'_3 (°F)
0.0000	76	75	75
0.1810	344		
0.3879		76	
0.4397			76
0.5172	563		
0.8534	838		
0.9828		78	77
1.1897			78
1.2931	1142	80	
1.3966			80
1.5000		82	
1.6034			82
1.7069		86	
1.8103			84
1.8362	1417		
1.9138		90	
2.0172			87
2.1207	impact	94	

Gravity Test
Cylinder Height 1 ft.
Input Voltage 18 Volts

Time (sec)	T_w' (°F)	T_2' (°F)	T_3' (°F)
0.0000	73	71	71
0.1304	160		
0.3652		72	
0.3913	351		72
0.7043	559		
0.9130		73	
0.9652			73
1.0696	800		
1.2261		75	
1.2522			74
1.4348		77	
1.4609			76
1.4870	1043		
1.6174		80	
1.6696			78
1.8261		82	
1.8783			80
1.9826	1261		
2.0348		86	
2.0870			82
2.5043	1420		

Gravity Test
Cylinder Height 1 ft.
Input Voltage 18 Volts

Time (sec)	T_w' (°F)	T_2' (°F)	T_3' (°F)
0.0000	73	71	71
0.1304	138		
0.1826		72	
0.3130			72
0.3913	330		
0.6783	534	73	
0.9391			73
1.0174	777		
1.0957		74	
1.2783		76	
1.3304			75
1.4348	1024		
1.4870		78	
1.5130			76
1.6957		80	
1.7217			78
1.8783		83	
1.9043	1246		
1.9304			80
2.0870		87	
2.1391			83
2.2957		90	
2.4783	1412		

Zero-Gravity Test
Cylinder Height 0.5 ft.
Input Voltage 18 Volts

Time (sec)	T_w' (°F)	T_1' (°F)	T_4' (°F)
0.0000	75	75	75
0.1034	101		
0.1293		90	
0.3362	284		
0.3879		196	76
0.6207	510		
0.6466		380	
0.9310		597	
0.9569	767		
0.9828			78
1.2931		788	80
1.3707	1032		
1.5000			82
1.7069		944	86
1.8621	1266		
1.9138			90
2.1026	impact		

Zero-Gravity Test
Cylinder Height 0.5 ft.
Input Voltage 18 Volts

Time (sec)	T_w' (°F)	T_1' (°F)	T_4' (°F)
0.0000	76	77	76
0.1538	175	109	
0.2564			77
0.4359	390	232	
0.7179		439	78
0.7436	638		
1.0256		668	79
1.1282	904		
1.2308			81
1.3846		852	
1.4359			84
1.5641	1160		
1.6410			87
1.8462			90
2.0513			95
2.1282	impact		

Gravity Test
Cylinder Height 0.5 ft.
Input Voltage 18 Volts

Time (sec)	T_w' (°F)	T_1' (°F)	T_4' (°F)
0.0000	73	73	72
0.0776	164		
0.1034		75	73
0.3103	586	175	
0.5172			74
0.5690		417	
0.6724	894		
0.9052		690	
0.9310			76
1.1379	1228		78
1.2931		954	
1.3190			82
1.5517			86
1.7069	1513		
1.7586		1152	90
1.9655			94
2.1724			98
2.2759		1286	
2.3276	1690		

Gravity Test
Cylinder Height 0.5 ft.
Input Voltage 18 Volts

Time (sec)	T'_w (°F)	T'_1 (°F)	T'_4 (°F)
0.0000	74	73	73
0.1034	228		
0.2069		151	
0.3621	618		
0.4397			75
0.5690		335	
0.7500	932		
0.8793		597	
0.9828			76
1.1897			79
1.2414	1261	838	
1.3966			82
1.6034			86
1.6810		1056	
1.7845	1534		91
2.0172			95
2.1724		1210	
2.2241			99
2.4052	1698		103

Gravity Test
Cylinder Height 0.5 ft.
Input Voltage 18 Volts

Time (sec)	T'_w (°F)	T'_1 (°F)	T'_4 (°F)
0.0000	74	74	73
0.1034		75	
0.1810	474		
0.3103		155	
0.4138			74
0.5431	756		
0.5690		366	
0.8793		606	
0.9310			76
0.9569	1080		
1.1379			78
1.2414		841	
1.3448			82
1.4741	1390		
1.5776			86
1.6810		1050	
1.7845			90
1.9914			94
2.0690	1615		
2.1466		1194	
2.1983			98

Zero-Gravity Test
Cylinder Height 1 ft.
Input Voltage 18 Volts

Time (sec)	T'_w (°F)	T'_1 (°F)	T'_4 (°F)
0.0000	69	69	68
0.1565	200		
0.3130		71	
0.4696	384		
0.6261			69
0.7304		85	
0.7826	606		
0.9391		151	
1.1478	860		
1.1739		282	
1.3565			70
1.4609		452	
1.5652			71
1.5913	1114		
1.7739		633	72
1.9826			74
2.0870	1332		
2.1130	impact		

Zero-Gravity Test
Cylinder Height 1 ft.
Input Voltage 18 Volts

Time (sec)	T'_w (°F)	T'_1 (°F)	T'_4 (°F)
0.0000	69	69	69
0.1304	148		
0.2870		70	
0.3913	329		
0.4435			70
0.6522		74	
0.6783	523		
0.8348		95	
1.0174	753		
1.0696		150	71
1.3043		246	
1.3565			72
1.4348	990		
1.5391		374	
1.6696			74
1.8522		523	
1.9304	1208		
1.9826			75
2.1130	impact		

Zero-Gravity Test
Cylinder Height 1 ft.
Input Voltage 18 Volts

Time (sec)	T_w' (°F)	T_1' (°F)	T_4' (°F)
0.0000	72	72	73
0.1035	96	75	
0.3103		153	
0.3362	286		
0.4655		74	
0.5431		323	
0.6207	519		
0.8535		545	
0.9569	778		
1.0345			76
1.2155		739	
1.2414			78
1.3707	1042		
1.4483			80
1.6034		900	
1.6552			83
1.8621	1276		87
2.1207	impact		

Gravity Test
Cylinder Height 1 ft.
Input Voltage 18 Volts

Time (sec)	T'_w (°F)	T'_1 (°F)	T'_4 (°F)
0.0000	71	71	70
0.1293	184		
0.3103			71
0.3621		79	
0.4138	373		
0.7500	591		
0.8276		115	
0.9310			72
1.0340		171	
1.1121	832		
1.2672		236	
1.4483			73
1.5259	1070	328	
1.7586			75
1.7845		437	
1.9655			76
2.0172	1286		
2.0690		547	
2.1724			78

Gravity Test
Cylinder Height 1 ft.
Input Voltage 18 Volts

Time (sec)	T'_w (°F)	T'_1 (°F)	T'_4 (°F)
0.0000	72	72	71
0.1043	93		
0.3130	278	73	
0.5478			72
0.5739	476		
0.7304		91	
0.9130	707		
0.9391		140	
1.1478		197	
1.2783			73
1.3304	955		
1.3826		270	
1.5652			74
1.6435		378	
1.7739			75
1.8000	1188		
1.9304		486	
1.9826			76

Zero-Gravity Test
Cylinder Height 0.5 ft.
Input Voltage 18 Volts

Time (sec)	T'_w (°F)	T'_2 (°F)	T'_3 (°F)
0.0000	69	69	69
0.1293	155		
0.2069			70
0.3879	361	70	
0.5948			71
0.6983	598		
0.8793		71	72
1.0603		74	73
1.0862	856		
1.2672		80	75
1.4741			80
1.5000		92	
1.5259	1109		
1.6552			86
1.7069		110	
1.8621			99
1.9138		135	
2.1207	impact		

Zero-Gravity Test
Cylinder Height 0.5 ft.
Input Voltage 18 Volts

Time (sec)	T'_w (°F)	T'_2 (°F)	T'_3 (°F)
0.0000	74	74	75
0.1795	214		
0.3077		75	
0.3590			76
0.4872	429		
0.7949	678	77	
0.8974			77
1.1026		80	79
1.2051	939		
1.3333		88	82
1.5385		101	86
1.6667	1184		
1.7436		122	93
1.875			
1.9487	1334	151	104
2.1026	impact		

Gravity Test
Cylinder Height 0.5 ft.
Input Voltage 18 Volts

Time (sec)	T_w' (°F)	T_2' (°F)	T_3' (°F)
0.0000	77	77	77
0.1271	158		78
0.3305		78	
0.3814	341		
0.5593			79
0.6610	546		
0.7627		82	
0.9661		97	80
1.0169	761		
1.1695		101	83
1.3729		110	86
1.4237	967		
1.5763		124	89
1.7797			93
1.8051		142	
1.8814	1147		
2.0085			98
2.0339		162	
2.2119			103
2.2373		185	

Gravity Test
Cylinder Height 0.5 ft.
Input Voltage 18 Volts

Time (sec)	T'_w (°F)	T'_2 (°F)	T'_3 (°F)
0.0000	76	76	76
0.1293	156		
0.3879	350	77	77
0.6724	570		
0.8793		91	79
1.0086	796		
1.0862		99	81
1.2931		105	84
1.4483	1016		
1.5000		118	88
1.7069		137	92
1.9138			97
1.9397		158	
1.9655	1204		
2.1207			102
2.1724		183	

Zero-Gravity Test
Cylinder Height 0.5 ft.
Input Voltage 36 Volts

Time (sec)	T'_w (°F)	T'_1 (°F)	T'_4 (°F)
0.0000	68	66	66
0.1034	182		
0.1552		78	
0.2069			68
0.3879	667		
0.4397		228	
0.4914			70
0.7241		546	77
0.8276	1276		
0.9052			90
1.0862		922	106
1.3190			124
1.4224	1814		
1.5517		1228	140
1.7586			154
1.9655			166
2.1207	impact		

Zero-Gravity Test
Cylinder Height 0.5 ft.
Input Voltage 32 Volts

Time (sec)	T'_w (°F)	T'_2 (°F)	T'_3 (°F)
0.0000	70	70	71
0.1293	241		
0.1810		71	
0.2328			72
0.4397	630	72	
0.5690			75
0.6207		76	
0.7759			82
0.8534	1106	85	
0.9569			94
1.0603		101	
1.1379			110
1.2414		128	
1.3448			129
1.3707	1581		
1.4483		166	
1.5517			152
1.6810		215	
1.7845			182
1.9138		274	
2.1207	impact		

Zero-Gravity Test
Cylinder Height 0.5 ft.
Input Voltage 36.5 Volts

Time (sec)	T'_w (°F)	T'_2 (°F)	T'_3 (°F)
0.0000	68	68	69
0.1810	387		70
0.2069		69	
0.4655			73
0.5172		73	
0.5948	946		
0.6724			85
0.7241		85	
0.8793			104
0.9310		110	
1.0862			130
1.1121	1576		
1.1379		152	
1.3190			158
1.3707		216	
1.5517			195
1.6293		295	
1.7845			241
1.8879		377	
2.1207	impact		

Gravity Test
Cylinder Height 0.5 ft.
Input Voltage 35 Volts

Time (sec)	T'_w (°F)	T'_2 (°F)	T'_3 (°F)
0.0000	76	76	76
0.1795	426		
0.2564		78	
0.2821			80
0.5897	1005		
0.6154		86	
0.6923			91
0.8205		107	
0.8974			109
1.0256		138	
1.0769			132
1.1282	1588		
1.2564		170	
1.3077			153
1.4872		207	
1.5385			171
1.7179		262	
1.7436			188
1.9744		341	208
2.2308			247
2.2564		426	

Gravity Test
Cylinder Height 0.5 ft.
Input Voltage 36 Volts

Time (sec)	T'_w (°F)	T'_2 (°F)	T'_3 (°F)
0.0000	75	76	76
0.1810	370		77
0.2586		78	
0.4655			79
0.5948	942		
0.6207		94	
0.6724			88
0.8276		178	
0.8793			104
1.0603		231	
1.0862			126
1.1379	1589		
1.2931			150
1.3190		330	
1.5259			172
1.5776		404	
1.7585			195
1.8621		490	
1.9914			232
2.1983		587	

Zero-Gravity Test
Cylinder Height 1 ft.
Input Voltage 36 Volts

Time (sec)	T'_w (°F)	T'_2 (°F)	T'_3 (°F)
0.0000	78	76	76
0.0783	86		
0.2348		78	77
0.2870	400		
0.5739		83	82
0.6261	940		
0.7826		96	93
0.9913		116	110
1.1478	1582		
1.2000		139	129
1.4087		160	145
1.6174			158
1.6435		179	
1.8522			168
1.8783		196	
2.0870			176
2.1130	impact	210	

Gravity Test
Cylinder Height 1 ft.
Input Voltage 36 Volts

Time (sec)	T'_w (°F)	T'_2 (°F)	T'_3 (°F)
0.0000	78	76	76
0.1293	202		
0.2586		78	78
0.4397	665		
0.6207		86	84
0.8276		100	97
0.8793	1306		
1.0345		120	114
1.2414		140	131
1.4741	1820	156	144
1.7069		170	154
1.9138		184	161
2.1207			168
2.1466		206	

Zero-Gravity Test
Cylinder Height 1 ft.
Input Voltage 35 Volts

Time (sec)	T'_w (°F)	T'_1 (°F)	T'_4 (°F)
0.0000	68	68	68
0.1034	184		
0.1810		69	
0.3103			69
0.3879	656		
0.4655		79	
0.6724		172	
0.6983			72
0.8276	1290		
0.8793			77
0.9310		439	
1.0862			84
1.2672		828	
1.2931			93
1.5000			103
1.6810		1135	
1.7069			111
1.9138			120
2.1207	impact		121
2.1983		1286	

Gravity Test
Cylinder Height 1 ft.
Input Voltage 36 Volts

Time (sec)	T'_w (°F)	T'_1 (°F)	T'_4 (°F)
0.0000	76	75	74
0.1565	274		
0.1826		76	
0.2870			75
0.4696		99	
0.5217	780		
0.6261			76
0.7043		284	
0.7565			81
0.9391			90
0.9913		553	
1.0174	1442		
1.1478			100
1.3565		874	110
1.5913			119
1.8000		1074	
1.8261			127
1.9826			
2.0348			132
2.2435			138
2.2696		1112	